

Three Dimensional Finite-Difference Time-Domain-Simulations of Photonic Crystals

Von der Fakultät für Mathematik und Physik der Universität Stuttgart
zur Erlangung der Würde eines
Doktors der Naturwissenschaften (Dr. rer. nat.)
genehmigte Abhandlung

von

Christian Hermann

aus Müllheim

Hauptberichter: Prof. Dr. O. Hess
Mitberichter: Prof. Dr. H. Herrmann
Tag der mündlichen Prüfung: 18. Juni 2004

Theoretische Quantenelektronik
Institut für Technische Physik, DLR
Pfaffenwaldring 38-40
D-70569 Stuttgart

2004

Acknowledgements

First of all I want to thank Prof. Dr. Ortwin Hess for his support and the possibility to work in his group. Many thanks also for providing me with excellent facilities and infrastructure.

I also would like to thank Prof. Dr. Hans Herrmann and Prof. Dr. Tilman Pfau for agreeing to be an examiner.

Many thanks go to the research groups in Stuttgart and Guildford:

- Dr. Stefan Scholz for introducing me into the field and laying the foundation of the FDTD-codes.
- Achim Hamm, Andreas Klaedtke and Christian Simmendinger for their patience while solving my computer problems, in particular Andreas Klaedtke for implementing the PML-boundaries.
- Dr. Edeltraud Gehrig, Dr. Dietmar Preisser and Klaus Böhringer for many helpful discussions.
- Heiko Pittner, Hui Bian, Kosmas Tsakmakidis and Durga Aryal for bearing my supervisions.

... and all of them for the excellent working atmosphere.

Special thanks I would like to express to Cécile Jamois from Max-Planck-Institute Halle for an excellent cooperation and many inspiring suggestions and discussions.

Thanks to my parents for making it possible for me to achieve my aims.

And, last but not least, many thanks to my family, Joschua and Monika, for all your love and support.

Contents

1	Summary	7
2	Introduction and Overview	11
3	Principles of Photonic Crystals	15
3.1	Electromagnetism of Periodic Dielectrics	15
3.1.1	Maxwell's Equations	15
3.1.2	Bloch's Theorem	17
3.1.3	The Concept of Brillouin-Zone and Bandstructure	19
3.1.4	The Bandgap	21
3.1.5	Symmetries	22
3.1.6	Density of States	24
3.2	One-Dimensional Photonic Crystals: The Bragg Mirror	25
3.3	Two-Dimensional Photonic Crystals	28
3.3.1	Basic Structures and Properties	29
3.4	Defects	39
3.4.1	Point Defects in 1D	40
3.4.2	Point- and Line-Defects in 2D	44
3.5	Transmission	49
3.6	Conclusion	50
4	Photonic Crystal Slab Structures	53
4.1	Introduction	53
4.2	Principles of Slab Waveguides	54
4.2.1	Slab Modes and Lightcone	54
4.2.2	Backfolding of Slab Modes	57
4.3	Interaction of In-Plane Periodicity and Vertical Structure.	59
4.3.1	Air-Bridge Structure	59
4.3.2	Infinite Low-Index Cladding	70
4.3.3	Finite Low-Index Cladding	73
4.3.4	Influence of Substrate	87
4.4	Conclusion	91

5	Spontaneous Emission in Inverted Opals	93
5.1	Introduction	93
5.2	Weak and Strong Coupling Regime	93
5.3	Classical and Quantum Description Within the Weak Coupling Regime	94
5.3.1	Quantum Approach	95
5.3.2	Classical Approach	96
5.4	Single Dielectric Sphere	99
5.5	Inverted Opals	100
5.5.1	Geometrical Setup	100
5.5.2	Bandstructure	102
5.6	Spontaneous Emission Rate	104
5.6.1	Space and Polarisation Dependence	104
5.6.2	Influence of Finite Size	108
5.7	Conclusion	111
6	The FDTD-Method and its Application in Photonic Crystal Analysis	113
6.1	Introduction	113
6.2	Basic Components and Methods	113
6.2.1	The Time-Stepping Algorithm and the Yee-Cell	114
6.2.2	Boundary Conditions	118
6.2.3	Sources	122
6.2.4	Data Extraction	127
6.3	Application to Photonic Crystals	132
6.3.1	Bandstructure and Eigenmode Calculations	132
6.3.2	Transmission and Reflection of Partially Periodic Systems	144
6.4	Conclusion	150
7	Conclusions and Outlook	151
	Bibliography	155

1 Summary

In this work the optical properties of three dimensional photonic crystal structures are studied theoretically by means of a full vectorial three dimensional finite-difference time-domain (FDTD) numerical simulation. First, the principles of lower dimensional photonic crystal structures are comprehensively discussed to assess the underlying physical principles of eigenmode and bandgap formation. For consistency, results are obtained on the basis of the FDTD-method. Then these principles are generalised to two different classes of three dimensional photonic crystal systems. First, we address the technologically important case of photonic crystal slab structures, i.e. two dimensional crystal patterns in vertically finite layer structures, where the localisation of the electromagnetic fields perpendicular to the crystal plane is achieved by total internal reflection. Starting with simple air-bridge structures the systems studied are extended to more complex vertical structures, like patterned insulator-on-silicon-on-insulator (IOSOI) cladding structures mounted on a substrate. The main focus thereby is laid on the quantitative description of effects that are related to the coupling of the index-guided localised photonic crystal modes to the environment. Next to the technologically extremely important calculation of radiation losses, it is, in particular, the discovery of cladding modes (i.e. modes that have no exponential decaying behaviour in the claddings) for frequencies in the bandgap region that is important and pioneering for the understanding of these systems and their potential application in integrated optics. Second, we focus on the fundamental physical properties of three dimensional inverted opal structures. Within the weak coupling regime, we analyse the strong frequency, polarisation and space dependence of the spontaneous emission rate (which is equivalent to the local density of states) of a dipole source embedded within our inverted opal in a crystallite of finite size. Thereby, strong enhancement effects are demonstrated close to dielectric interfaces for certain frequencies due to the continuity conditions of the electric field modes. These results are essential for the interpretation of luminescence experiments, because in real systems there is always an inhomogenous distribution of emitters and an approximation based on a total density of states becomes invalid. Finally, the basic building blocks of the FDTD-code like core algorithm, boundary conditions and data extraction are discussed in detail. Moreover, special adaptations of these components with respect to photonic crystal analysis are discussed and exemplary results for the dependence on internal simulation parameters on the results are shown.

Zusammenfassung

In der vorliegenden Arbeit werden die optischen Eigenschaften von dreidimensionalen photonischen Kristallen theoretisch mit Hilfe von voll-vektoriellen finite-difference time-domain (FDTD)-Simulationen untersucht. Zunächst werden die Prinzipien von niederdimensionalen photonischen Kristall-Systemen diskutiert, insbesondere um die zugrundeliegenden physikalischen Mechanismen zu klären, die für das Zustandekommen von Eigenmoden und Bandlücken verantwortlich sind. Die zugehörigen exemplarischen Ergebnisse werden mit Hilfe der FDTD-Methode berechnet. Anschliessend werden diese Prinzipien auf zwei verschiedene Klassen dreidimensionaler Systeme verallgemeinert. Als erstes betrachten wir den technologisch wichtigen Fall eines zweidimensionalen photonischen Kristalls in einer vertikal endlichen Schichtstruktur, wobei die Wellenführung senkrecht zur Kristallebene durch Totalreflektion erfolgt. Beginnend mit einfachen Membranstrukturen werden die untersuchten Systeme bis hin zu komplex strukturierten IOSOI-Schichtsystem mit Claddings auf einem Substrat erweitert. Das Hauptaugenmerk liegt dabei auf der quantitativen Beschreibung von Effekten im Zusammenhang mit der Kopplung der index-geführten photonischen Kristallmoden mit ihrer Umgebung. Neben der technologisch äusserst wichtigen Berechnung von Streuverlusten ist insbesondere die Entdeckung von Cladding-Moden, d.h. Moden die keinen exponentiellen Abfall in den Claddings zeigen, für Frequenzen innerhalb der Bandlücke wichtig und neu für das Verständnis dieser Systeme im Hinblick auf deren Anwendung in der integrierten Optik. Als zweites betrachten wir grundlegende physikalische Eigenschaften in dreidimensionalen invertierten Opalen. Im Grenzfall der schwachen Wechselwirkung analysieren wir die starke Orts-, Polarisations- und Frequenzabhängigkeit der spontanen Emissionsrate, hier äquivalent zur lokalen Zustandsdichte, eines Punktdipols in einem Kristalliten endlicher Grösse. Es wird dabei signifikante Verstärkung an dielektrischen Grenzflächen für bestimmte Frequenzen gezeigt, die durch die Stetigkeitsbedingungen der elektrischen Feldmoden verursacht wird. Diese Ergebnisse sind essentiell für die Interpretation von Lumineszenz-Experimenten, da es in realen Systemen stets eine inhomogene Verteilung der Emitter gibt und somit eine Näherung unter Verwendung der totalen Zustandsdichte nicht mehr gilt. Am Schluss werden fundamentale Komponenten eines FDTD-Programms wie Kernalgorithmus, Randbedingungen und Datenauswertung detailliert beschrieben. Darüberhinaus werden spezielle Anpassungen dieser Komponenten im Hinblick auf die Analyse photonischer Kristalle diskutiert und exemplarische Ergebnisse zur Abhängigkeit von internen Simulationsparametern vorgestellt.

2 Introduction and Overview

The control of light propagation and emission is today one of the most exciting and progressing fields with respect to potential applications in information technology. Indeed, the traditional way of transporting and processing large amount of data with electronic circuits reaches physical limits that make it hard to satisfy the demands of the upcoming global information society. Many of these limitations are hoped to be overcome by systems that are based on photons instead of electrons. While in some aspects photonic devices already play a leading role as in long range transmission through optical fibres, an on-chip realisation of photonic circuits is still not achieved on a level mature enough for the market. Moreover, electronic circuits are still orders of magnitudes ahead with respect to miniaturisation.

For fundamental physical research this means there is a large need for the design and the understanding of systems that can control and manipulate light on small lengthscales, significantly smaller than the wavelength of the light itself.

In 1987, Yablonovitch [1] and John [2] independently suggested the use of periodically nano-structured (which means structures of a size similar or smaller than one wavelength) dielectrics to engineer the mode structure and the density of states in a meta-material that is now well known as photonic crystals. Their motivation was an interdisciplinary use of principles long known in electrodynamics and solid-state-physics. Similar to the electrons in a crystalline semiconductor, a crystal of periodically arranged dielectric scatterers with carefully chosen geometry, should exhibit a photonic band-gap, i.e. a region with vanishing density of states and prohibited propagation. In this type of material, an excited emitter with a transition frequency within the band-gap is stabilised and not able to emit a photon. It quickly turned out that this is really possible and a new field of research was born.

In the last nearly two decades intensive research has been performed and showed that the original idea of suppressing spontaneous emission is only one of many exciting possibilities photonic crystals are able to offer.

The strongly modified interaction between radiation and matter has also been applied e.g. for the enhancement of nonlinear effects. This mainly relies on the fact that within photonic crystals there can be light propagation with very low group velocities. Also, besides suppression of spontaneous emission [3], strong enhancement has been predicted

[4]. The tailoring of the local density of states has furthermore led to the proposal of various non-Markovian quantumoptical effects like an anomolous Lamb-shift [5] or splitting of optical levels at band edges [6]. It is obvious that these effects may be utilised for the optimisation of light sources like semiconductor lasers.

However, the largest variety of ideas has surprisingly not arised from the originally intended manipulation of matter-light interaction but from the purely classical propagation properties of photonic crystals. It has been recognised quite early that the controlled inclusion of defects in a perfect lattice generates strongly localised states within the bandgap. In the case of a pointlike defect this results in a cavity that can have amazingly high quality factors simultaneously with very small mode volumes [7]. A property that is very desired in optical electronics. For a linear defect however light is confined in two space directions and can propagate along the line which creates a waveguide with extensions on the lengthscale of the wavelength. Obviously, this is also strongly desired by technologists. Two dimensional calculations and simulations presented very early by Joannopoulos et al [8] moreover suggested very interesting properties of these waveguides like extremely low losses at sharp bends [9]. This is possible because the guiding mechanism in a photonic crystal is multiple Bragg interference and not total internal reflection as in conventional optical devices. This means that it is not necessary that the guiding happens in a material with high index or in a material at all. This perception made a very new and interesting technical application possible, the photonic bandgap fibre (PBF). In a PBF light is guided along a fibre with a periodically structured cross-section, with the main intensity confined in an air-channel. These fibres apparently have very low absorbtion losses and suffer only weakly from material dispersion. Moreover, very high intensities can be sent through a PBF without unwanted nonlinear interaction. PBF's are now very likely to become the first large scale technological application based on photonic crystals. Credits hereby must be given to the pioneering work of Phillip St. John Russell [10].

It would be beyond the scope of this introduction to list all possible applications and devices proposed in the last years, like beam splitters, polarisation sensitive devices, wavelength monitors or dispersion compensators. However, it is important to mention that the focus of the research concerning applications has recently been concentrated to two-dimensionally structured layer-by-layer systems where the confinement perpendicular to the crystal plane is achieved by total internal reflection. Although one loses some of the benefits of full three dimensional crystals, the ease of fabrication seems to pay off. Nevertheless there has been a lot of progress in the last few years to overcome the most fundamental disadvantage of three dimensional crystals, the difficult controlled inclusion of defects [11].

From the beginning of the research in this field, numerical analysis and simulation has played a very important role. The reason for this is that the solutions of the full vec-

torial Maxwell's equations are required to correctly describe the optical properties and that due to the structure of the equations no reasonable analytical approximation is possible. It has e.g. been demonstrated in the early 1990's that a scalar approximation cannot explain the existence of a band-gap. Another reason is that the experimental fabrication of photonic crystals is difficult and time consuming. A pure heuristic try-and-error approach without supporting design suggestions from theory would be unpractical.

The state of the art in numerical analysis of these systems consists of a complementary use of frequency- and time-domain methods. The most prominent and widespread frequency-domain-technique is the plane-wave-method for the computation of photonic band-structures and eigenmodes, that is based on a time-harmonic plane wave decomposition of eigenmodes and dielectric structure. Its advantages are the relative efficient computation and high accuracy in frequency due to its iterative nature, while suffering from the inability to handle systems suffering from scattering losses. On the other hand, for time-domain methods (most prominently the finite-difference time-domain (FDTD) method), there are nearly no restrictions in the geometrical or physical setup, but only in required computing resources. Unfortunately, the latter are immense and provide a significant disadvantage of FDTD. Nevertheless, due to the rapid progress in computing power, FDTD has become the standard technique for analysing technologically relevant problems. However, because it is still necessary to work with clusters or supercomputers to provide the required power, recently more sophisticated and promising new developments has appeared like finite-volume, multigrid or hybrid-basis approaches that aim to make photonic crystal analysis possible on standard personal computers.

This work addresses several aspects of photonic crystal research. Chapter 3 tries to give a comprehensive overview over the fundamental physics and mechanisms leading to bandstructures, eigenmodes and especially bandgaps. This is discussed for one and two dimensional systems, and fundamental principles are generalised to more complicated systems. To ensure consistency, all exemplary results presented in this chapter are calculated by self-developed computer codes.

Chapter 4 deals very detailed with one of the central aspects for the technical application of two dimensional photonic crystals in finite layer structures. The interaction of the crystal pattern with the vertical structure and the resulting deviations from ideal two dimensional systems, especially concerning out-of-plane losses due to coupling to the mode bath of the environment. By gradually progressing from simple idealised structures up to complex systems with claddings and substrate the important physical mechanisms as well as quantitative results for technologically relevant material systems are shown. The discovery of cladding modes in insulator-on-silicon-on-insulator (IOSOI) structures is thereby pioneering for the comprehensive understanding of these systems.

In Chapter 5 the attention is drawn to more fundamental physics in the context of

light-matter-interaction in a three dimensional opal structure. By applying a special modification of the FDTD-method the strong space and frequency dependance of the spontaneous emission rate in a finite opal crystallite within the weak coupling regime is analysed in detail. This has a strong relevance for the interpretation of luminescence experiments [12] and the experimental probing of the mode structure of a photonic crystal. In this work this has been done for the first time in a three dimensional system with finite size.

All results of the preceding chapters have been obtained by several problem adapted versions of an FDTD algorithm. As FDTD is a very general method for solving electro-dynamical problems a proper adaptation to a certain problem with respect to efficiency, reliability and accuracy is sometimes difficult and not straightforward. Therefore in chapter 6 the FDTD algorithm is described in detail including practical advise for the use in photonic crystal analysis.

3 Principles of Photonic Crystals

The basic principles and underlying theory of photonic crystals are introduced in this chapter. First, necessary prerequisites from electrodynamics, solid state physics and group theory are discussed in the context of photonic crystal analysis, most of them using the 1D case as an example. Next, basic structures and properties of crystals with various dimensionality are presented. Finally, more sophisticated concepts like the introduction of controlled defects are explained.

3.1 Electromagnetism of Periodic Dielectrics

In some way, the invention of photonic crystals in 1987 [1, 2] was not the discovery of complete new physical principles, but an outstanding interdisciplinary recombination of well-known physics. The essential part thereby was the combination of Maxwell's equations for electromagnetic fields in a dielectric structure with Bloch's theorem for periodic potentials from solid-state physics. The main aspect in understanding photonic crystals is the understanding of how these two principles interact in a periodically structured dielectric.

3.1.1 Maxwell's Equations

Under general conditions the four Maxwell's equations in Heaviside-Lorentz units read as

$$\nabla \cdot \vec{B}(\vec{r}, t) = 0 \quad (3.1)$$

$$\nabla \times \vec{E}(\vec{r}, t) + \frac{1}{c} \frac{\partial}{\partial t} \vec{B}(\vec{r}, t) = 0 \quad (3.2)$$

$$\nabla \cdot \vec{D}(\vec{r}, t) = \rho(\vec{r}, t) \quad (3.3)$$

$$\nabla \times \vec{H}(\vec{r}, t) - \frac{1}{c} \frac{\partial}{\partial t} \vec{D}(\vec{r}, t) = \vec{j}(\vec{r}, t) \quad (3.4)$$

with the material relations

$$\vec{B} = \vec{B}(\vec{H}) \quad (3.5)$$

$$\vec{D} = \vec{D}(\vec{E}) \quad (3.6)$$

For the analysis of nanostructured dielectrics we can make some reasonable simplifications. First, we assume that no free currents or charges are present in the system. This means we can set the right hand sides of the inhomogenous equations 3.3 and 3.4 to zero. Moreover, we can assume linear dielectric materials with vanishing magnetic susceptibility. This is reasonable for most dielectric materials as long as the field intensities are small enough. The general material equations 3.5 and 3.6 under this assumption are now

$$\vec{B}(\vec{r}, t) = \vec{H}(\vec{r}, t) \quad (3.7)$$

$$\vec{D}(\vec{r}, t) = \epsilon(\vec{r}) \vec{E}(\vec{r}, t) \quad (3.8)$$

where $\epsilon(\vec{r})$ is the spacially varying dielectric constant. In principal, $\epsilon(\vec{r})$ can also be time and/or frequency dependent, but this is not under consideration in our case. If we go back to Maxwell's equations with these assumptions they now can be written as two curl equations with the time derivatives only depending on \vec{E} and \vec{H} and two homogeneous equations completing the set.

$$\nabla \times \vec{E}(\vec{r}, t) = -\frac{1}{c} \frac{\partial}{\partial t} \vec{H}(\vec{r}, t) \quad (3.9)$$

$$\nabla \times \vec{H}(\vec{r}, t) = \frac{1}{c} \epsilon(\vec{r}) \frac{\partial}{\partial t} \vec{E}(\vec{r}, t) \quad (3.10)$$

$$\nabla \cdot \vec{E}(\vec{r}, t) = 0 \quad (3.11)$$

$$\nabla \cdot \vec{H}(\vec{r}, t) = 0 \quad (3.12)$$

In practical applications, e.g. solving these equations numerically, it is sufficient to solve the curl equations while assuring the homogeneous equations are fulfilled. In this case it might be convenient to rearrange the curl equations in a way that they depend only on \vec{E} or \vec{H} , respectively. This leads to two second order wave equations, which are often called master equations in literature [8]:

$$\nabla \times \left[\epsilon^{-1}(\vec{r}) \nabla \times \vec{H}(\vec{r}, t) \right] = -\frac{1}{c^2} \frac{\partial^2}{\partial t^2} \vec{H}(\vec{r}, t) \quad (3.13)$$

$$\epsilon^{-1}(\vec{r}) \nabla \times \left[\nabla \times \vec{E}(\vec{r}, t) \right] = -\frac{1}{c^2} \frac{\partial^2}{\partial t^2} \vec{E}(\vec{r}, t) \quad (3.14)$$

To analyse the structure of 3.13 (we do not choose 3.14 for reasons that will be explained later) we choose a fourier decomposition in time, which means we assume a

time-harmonic behaviour of the fields. This can be done without loss of generality. The ansatz

$$\vec{H}(\vec{r}, t) = \vec{H}(\vec{r}) e^{i\omega t} \quad (3.15)$$

leads to the fourier space master equation

$$\nabla \times \left[\epsilon^{-1}(\vec{r}) \nabla \times \vec{H}(\vec{r}) \right] = \frac{\omega^2}{c^2} \vec{H}(\vec{r}) \quad (3.16)$$

which can be understood as an eigenvalue problem for the eigenfunctions $\vec{H}(\vec{r})$ and the eigenvalues ω^2 of the general form

$$\hat{\Theta} \vec{H}(\vec{r}) = \omega^2 \vec{H}(\vec{r}) \quad (3.17)$$

where the operator $\hat{\Theta}$ contains the information about the dielectric structure. The eigenvalue problem based on 3.13 is Hermitian and therefore ensuring that the eigenvalues are real and the eigenfunctions form a complete set of basis functions. This is convenient for further theoretical analysis as well as for certain types of numerical solutions (e.g. the plane-wave-expansion method (PWM, [13])). The reason for choosing 3.13 instead of 3.14 is that the different position of $\epsilon(\vec{r})$ within $\hat{\Theta}$ destroys the hermiticity. For further analysis of 3.16 we need more information about the dielectric structure described by $\epsilon(\vec{r})$. This is discussed in the next section.

3.1.2 Bloch's Theorem

Within the eigenvalue equation 3.16 the dielectric constant $\epsilon(\vec{r})$ mathematically plays the role of a potential. In a photonic crystal, we know that this potential is by definition periodic in one or more dimensions. We will now take advantage of this discrete translational symmetry to learn more about the solutions of the master equation. Mathematically, the periodicity of $\epsilon(\vec{r})$ can be expressed as

$$\epsilon(\vec{r} + \vec{R}) \quad (3.18)$$

where \vec{R} is an integer multiple of a primitive lattice vector \vec{R} in one dimension or the superposition of integer multiples of primitive lattice vectors \vec{R}_i in d dimensions:

$$\vec{R} = \sum_{i=1}^d n_i \vec{R}_i \quad (3.19)$$

with integer n_i . For simplicity we will restrict ourselves now to the one dimensional case (in x-direction: $\vec{R} = a\hat{x}$), without loss of generality. For completeness we have to state that we assume a continuous translational symmetry in the other two space directions. The discrete translational symmetry can be expressed in terms of a translation operator \hat{T} which creates a spatial shift by a . Due to the structure of the dielectric potential $\epsilon(\vec{r})$ it can be shown, that \hat{T} commutes with $\hat{\Theta}$:

$$[\hat{T}, \hat{\Theta}] = 0 \quad (3.20)$$

This means we can construct simultaneous eigenfunctions of \hat{T} and $\hat{\Theta}$ and therefore classify the eigenfunctions of $\hat{\Theta}$ by the eigenvalues of \hat{T} . The eigenfunctions of \hat{T} are easily determined as plane waves with wavenumber k , because the translational symmetry only allows the eigenfunctions to differ by a phase shift which corresponds to the eigenvalue θ :

$$\hat{T} e^{ikx} = e^{ik(x+a)} = e^{ika} e^{ikx} = \theta e^{ikx} \quad (3.21)$$

It is obvious now, that θ is not unique for all wavevectors k , because each $k + m 2\pi/a$ (m is an integer) will produce the same θ as k . Mathematically, this means that all plane waves corresponding to $k + mG$ with $G = 2\pi/a$ form a degenerate set of eigenfunctions, and that all superpositions of plane waves with wavevector $k + mG$ are also an eigenfunction with eigenvalue θ . As θ does only depend on k as a free parameter for a given structure, we can now make the step back to the master equation and state the following:

The eigenfunctions of $\hat{\Theta}$ can be classified by a wavevector k and have the form:

$$\vec{H}_k(x) = e^{ikx} \sum_m \vec{H}_m e^{imGx} = e^{ikx} \vec{u}_k(x) \quad (3.22)$$

with the lattice periodic function $u_k(x) = u_k(x + na)$ and plane wave amplitudes \vec{H}_m . This statement is well known in solid state physics as Bloch's theorem [14].

We will now generalise Bloch's theorem for d dimensions:
A given d -dimensional structure with dielectric constant

$$\epsilon(\vec{r}) = \epsilon(\vec{r} + \vec{R}) \quad (3.23)$$

where

$$\vec{R} = \sum_{i=1}^d n_i \vec{R}_i \quad (3.24)$$

with primitive lattice vectors \vec{R}_i and integer numbers n_i has eigenfunctions which can be labeled by an wavevector \vec{k} and expressed in the form

$$\vec{H}_{\vec{k}}(\vec{r}) = e^{i\vec{k}\vec{r}} \sum_{\vec{G}} \vec{H}_{\vec{k},\vec{G}} e^{i\vec{G}\vec{r}} = e^{i\vec{k}\vec{r}} \vec{u}_{\vec{k}}(\vec{r}) \quad (3.25)$$

where \vec{G} represents reciprocal lattice vectors of the form

$$\vec{G} = \sum_{i=1}^d m_i \vec{G}_i \quad (3.26)$$

with integer numbers m_i and

$$\vec{G}_i \cdot \vec{R}_i = 2\pi \delta_{i,j} \quad (3.27)$$

and a lattice periodic function.

$$\vec{u}_{\vec{k}}(\vec{r}) = \vec{u}_{\vec{k}}(\vec{r} + \vec{R}) \quad (3.28)$$

$\delta_{i,j}$ is the Kronecker delta function and \vec{G}_i primitive reciprocal lattice vectors.

3.1.3 The Concept of Brillouin-Zone and Bandstructure

We know from Bloch's theorem that wavevectors \vec{k} and $\vec{k} + \vec{G}$ produce the same set of eigenfunctions and corresponding eigenvalues. Therefore we can restrict our analysis to the smallest region in k-space that can be expanded to the entire k-space by adding reciprocal lattice vectors. Only this region contains non-redundant information. From solid state physics we know that this smallest possible region can be constructed as the primitive Wigner-Seitz cell in reciprocal space and is called the first Brillouin-zone (BZ) [14]. This concept is easily understood in a one dimensional photonic crystal, because it is obvious that only k-values from $-\pi/a$ to π/a (which is equivalent to $-0.5G$ to $0.5G$) fulfill this condition. The complete frequency eigenvalue spectrum of the system can be obtained by calculating the eigenvalues for these k-values. One step further we can sort all eigenvalues corresponding to a certain k-value and label them by an index, we will refer from now to as the band-index n. The unique representation of an eigenfunction is therefore

$$\vec{H}_{\vec{k}}^n(\vec{r}) = e^{i\vec{k}\vec{r}} \sum_{\vec{G}} \vec{H}_{\vec{k},\vec{G}}^n e^{i\vec{G}\vec{r}} = e^{i\vec{k}\vec{r}} \vec{u}_{\vec{k}}^n(\vec{r}) \quad (3.29)$$

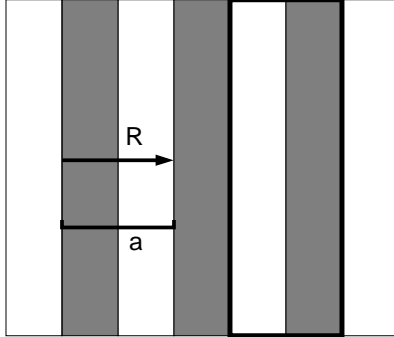


Figure 3.1: Schematic picture of a one dimensional photonic crystal. The black framed box shows a primitive unit cell, R is a lattice vector and a the lattice constant

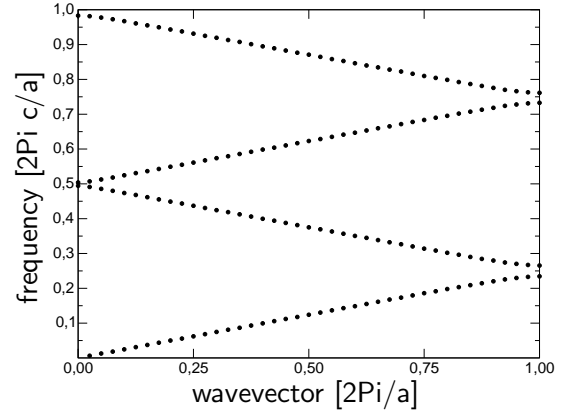


Figure 3.2: Bandstructure of a low index contrast Bragg-mirror. The k -range from $-\pi/a$ to 0 is not displayed because it is mirror symmetric with respect to $k = 0$.

or, as also often used in literature, the labelling by the frequency eigenvalue:

$$\vec{H}_{\vec{k}}^{\omega}(\vec{r}) = e^{i\vec{k}\vec{r}} \sum_{\vec{G}} \vec{H}_{\vec{k},\vec{G}}^{\omega} e^{i\vec{G}\vec{r}} = e^{i\vec{k}\vec{r}} \vec{u}_{\vec{k}}^{\omega}(\vec{r}) \quad (3.30)$$

The combination of these two concepts results in an ω over \vec{k} diagram which is called the bandstructure and has proven to be very useful when discussing the properties of periodic systems in solid state physics, and now as well in the field of photonic crystals. The frequencies are displayed in units of $2\pi c/a$, which has proven to be useful. As Maxwell's equations are linear, the geometry and eigenvalues/eigenfunctions scale also linearly. Therefore it makes sense to normalize frequencies by a fundamental length of the crystal, the lattice constant. The normalization to $2\pi c/a$ is always assumed in this work when no explicit frequency units are given. We will illustrate this concept now for a one dimensional photonic crystal. As shown in fig. 3.1 the unit cell consists of two layers with the same thickness $a/2$ and refractive indices n_1 and n_2 . If we assume now a very small index contrast n_1/n_2 the structure is expected to have a similar dispersion relation as an homogeneous material with an average index $n_{avg} = (n_1 + n_2)/2$, because the periodic modulation represents only a small perturbation. This dispersion relation is well known to be a straight line $\omega = n_{avg} \cdot k$. The modes of this slightly perturbed structure consist mainly of one component: The plane wave with wavevector \vec{k} . In this simple system we can easily see what happens for a k -value k_1 larger than π/a . The

modes are backfolded by an reciprocal lattice vector \vec{G} to a k-value $k_0 = k_1 - G$ into the first Brillouin zone, and now both eigenvalues $\omega_0 = n_{avg} \cdot k_0$ and $\omega_1 = n_{avg} \cdot k_1$ belong to the k-value k_0 , but have gained an additional band index. Moreover, due to the symmetry of the layer system we do not have to distinguish between k and $-k$ and therefore can restrict to the interval $[0, \pi/a]$. This procedure is illustrated in fig. 3.2. This picture of backfolding into the first Brillouin-zone is only valid in a strict sense when the modes have one dominant fourier-component (which means they are nearly plane waves). In a general case all modes contain contributions of plane waves $e^{i(k+G)x}$ for an infinite number of G vectors.

3.1.4 The Bandgap

In the discussion of the last section we ignored what happens at the edge of the BZ. It is already obvious from fig. 3.2 that the perturbation of the homogenous case is largest and that a small gap in the dispersion relation arises for $k = \pm\pi/a$. We now want to clarify the physical reason of this effect:

The (nearly) plane wave for $k_0 = \pi/2$ can be mapped by the reciprocal lattice vector $-G$ to $k_1 = -\pi/2$. As both plane waves have the same absolute value of k , both will contribute to the eigenmode. The result of an interaction of a propagating and counter-propagating plane wave is a standing wave. The same argumentation holds true when mapping k_1 to k_0 by $+G$. This means that the modes have a two-fold degeneracy. We can now construct basis functions of this two-dimensional subspace, with the maxima of the standing wave either in the higher or the lower dielectric material. As the electromagnetic energy

$$Energy = \int \epsilon(x) \left| \vec{E}(x) \right|^2 + \left| \vec{H}(x) \right|^2 dx \quad (3.31)$$

is different in these two cases, the modes have different frequency eigenvalues. At the edges of the BZ this results in a degeneracy splitting in the band diagram. In turn, this splitting causes a bandgap. That we define as the frequency interval, within which no modes exist for all possible \vec{k} -vectors. This has further consequences:

1. Due to the lack of modes, the density of states (see 3.1.6) in the band-gap is zero. This has a strong influence e.g. on spontaneous emission. We will discuss this topic in more detail in chapter 5.
2. No propagation is allowed inside the photonic crystal for frequencies within the gap. This certainly only holds when propagation within the same dimensionality as the Brillouin-zone is taken into account. This means for the 1D-case that a bandgap only exists for propagation perpendicular to the layers, and for the 2D-case that there is generally no bandgap for propagation out of the crystal plane.

We want to stress here, that point 2 is not a commensurate condition for the existence of a bandgap as often mistaken in literature. It will be discussed later that other mechanism can also cause zero transmission through a photonic crystal, without the existence of a bandgap.

In practical applications normally one aims to make the bandgap as large as possible. To obtain a comparable measure for the size, we now introduce the relative gap width of a bandgap with lower edge ω_1 and upper edge ω_2

$$\frac{\Delta\omega}{\omega_c} = \frac{\omega_2 - \omega_1}{\frac{1}{2}(\omega_2 + \omega_1)} \quad (3.32)$$

where $\Delta\omega$ is the absolute gap width and ω_c the center frequency of the gap. Eq. 3.31 implies that the size of the bandgap is dependent on the refractive index contrast of the two layers. However, geometrical parameters are also important for size and position of the gap. The dependance of these parameters varies strongly in structures of different dimensionalities and is discussed in the sections later on.

3.1.5 Symmetries

An important tool for analysing photonic crystals and their optical properties is information on the behaviour of eigenmodes under certain symmetry operations. In many cases this allows qualitative predictions e.g. about transmission behaviour, but is generally useful when there is a coupling of a photonic crystal to the environment (e.g. incoupling of external sources). In the following we will therefore discuss fundamental symmetries of electromagnetic systems.

Mirror symmetry

The symmetry that will be used mainly in this work is the mirror symmetry. Generally, if the dielectric constant $\epsilon(\vec{r})$ has an invariance under a mirror operation \hat{M} , then \hat{M} commutes with the operator $\hat{\Theta}$ of the master equation, and Eigenmodes can thus be classified by the eigenvalues of \hat{M} . We therefore define a mirror operator that mirrors a vector field $\vec{F}(\vec{r})$ at the plane $x = 0$

$$\hat{M}\vec{F}(\vec{r}) : x \rightarrow -x, F_x \rightarrow -F_x \quad (3.33)$$

This can be easily generalised to an arbitrary mirror plane, but for simplicissity we will discuss only this simple example. It is obvious that applying \hat{M} two times to the vector field will recreate the original function. Therefore, the single application can only cause a multiplication by a constant

$$\hat{M}\vec{F}(\vec{r}) = \alpha\vec{F}(\vec{r}) \quad (3.34)$$

$$\hat{M}^2\vec{F}(\vec{r}) = \alpha^2\vec{F}(\vec{r}) = \vec{F}(\vec{r}) \quad (3.35)$$

From these two equations it follows, that α (the eigenvalue of \hat{M}) can only have the values $+1$ and -1 . The eigenmodes of $\vec{F}(\vec{r})$ will therefore be classified for there ‘odd’ and ‘even’ symmetry ($\alpha = -1$ and $\alpha = +1$, respectively).

When we adopt this principle to the electromagnetic eigenmodes of a photonic crystal we have to be careful. While the argumentation above is applicable straight forward to the electric field $\vec{E}(\vec{r})$, the magnetic field $\vec{H}(\vec{r})$ gains an additional sign due to its pseudovectorial character. We will summarize the conditions that are valid for odd and even electromagnetic eigenmodes due to a mirror operation at an $x=0$ -plane in the following table:

even mode:

$$\begin{aligned} E_x(x, y, z) &= -E_x(-x, y, z) \\ E_y(x, y, z) &= +E_y(-x, y, z) \\ E_z(x, y, z) &= +E_z(-x, y, z) \\ H_x(x, y, z) &= +H_x(-x, y, z) \\ H_y(x, y, z) &= -H_y(-x, y, z) \\ H_z(x, y, z) &= -H_z(-x, y, z) \end{aligned}$$

odd mode:

$$\begin{aligned} E_x(x, y, z) &= +E_x(-x, y, z) \\ E_y(x, y, z) &= -E_y(-x, y, z) \\ E_z(x, y, z) &= -E_z(-x, y, z) \\ H_x(x, y, z) &= -H_x(-x, y, z) \\ H_y(x, y, z) &= +H_y(-x, y, z) \\ H_z(x, y, z) &= +H_z(-x, y, z) \end{aligned}$$

or, more generally speaking:

- An even mode has even parallel components of the electric field and an even normal component of the magnetic field. The other components are odd.
- An odd mode has odd parallel components of the electric field and an odd normal component of the magnetic field. The other components are even.

where normal and parallel are meant with respect to the mirror plane. We want to note here, that e.g. a plane wave propagating in x-direction with an electric field polarized in y-direction and magnetic field in z-direction is odd with respect to a ($y = \text{constant}$)-mirror plane.

Polarisation

A special type of mirror symmetry occurs in 2D systems. Due to the continuous translational invariance perpendicular to the two dimensional basis (referred to as z-direction),

an intrinsic mirror symmetry exists. Moreover, the fields can only vary by a phase factor $e^{ik_z z}$ in z-direction. If we restrict ourselves to in-plane propagation ($k_z = 0$), and consider the symmetry conditions described in the previous section we easily obtain that even modes can only consist of E_x , E_y and H_z field components and odd modes of E_z , H_x and H_y , respectively. If we use this information in the master equations 3.13 and 3.14 we see that they decouple into two scalar equations for E_z and H_z .

$$\left(\frac{\partial}{\partial x} \epsilon^{-1}(x, y) \frac{\partial}{\partial x} + \frac{\partial}{\partial y} \epsilon^{-1}(x, y) \frac{\partial}{\partial y} \right) H_z(x, y, t) = -\frac{1}{c^2} \frac{\partial^2}{\partial t^2} H_z(x, y, t) \quad (3.36)$$

$$\left(\epsilon^{-1}(x, y) \frac{\partial^2}{\partial x^2} + \epsilon^{-1}(x, y) \frac{\partial^2}{\partial y^2} \right) E_z(x, y, t) = -\frac{1}{c^2} \frac{\partial^2}{\partial t^2} E_z(x, y, t) \quad (3.37)$$

As even modes only have transverse (in-plane) electric field components, they are called transverse electric (TE), while odd modes, that consist only of transverse magnetic field components, are denoted transverse magnetic (TM). This separation into two scalar master equations can drastically reduce the numerical effort in calculating band structures and eigenmodes for purely two dimensional systems.

If the continuous translational symmetry of a two dimensional photonic crystal is broken, but a mirror symmetry still exists (e.g. in a photonic crystal slab), it is common to call the odd modes TM-like and the even modes TE-like. Directly in the mirror plane, the strict separation of components is still valid.

3.1.6 Density of States

The photonic density of states (DOS) plays an important role in understanding the optical properties of a photonic crystal because it describes the integral availability of allowed states in a certain frequency range regardless of band-index or k-value. The DOS is defined as

$$N(\omega) = \sum_n \int_{BZ} d^3k \delta(\omega - \omega_n(\vec{k})) \quad (3.38)$$

where the k-space integration covers the hole Brillouin zone (BZ) and $\omega_n(\vec{k})$ is the eigenvalue for band-index n and k-vector \vec{k} . δ is the Dirac delta function. In free space $N(\omega)$ is proportional to ω^2 . A vanishing DOS is the commensurate condition for a complete photonic bandgap and not, as often argued in literature, a perfect reflection or vanishing transmission behaviour. We will discuss later that a vanishing transmission can also be caused by coupling effects due to symmetry mismatch.

$N(\omega)$ represents a quantity that is averaged over the unit cell. It must not be confused with the coupling strength of an emitter at a certain position to the electromagnetic

environment which can strongly vary in space. This quantity is called local density of states (LDOS) and weights the contributions of each $\omega_n(\vec{k})$ by the intensity of the electric field at the position of the emitter, averaged over all dipole polarisations:

$$N(\omega, \vec{r}) = \sum_n \int_{BZ} d^3k \left| \vec{E}_{\vec{k}}^n(\vec{r}) \right|^2 \delta(\omega - \omega_n(\vec{k})) \quad (3.39)$$

The LDOS plays an essential role in quantum-electrodynamical phenomena in photonic crystals [15]).

3.2 One-Dimensional Photonic Crystals: The Bragg Mirror

In this section we will discuss the simplest case of a photonic crystal, the one dimensional Bragg-mirror consisting of alternating layers of two different materials. This structure is well known and has been used in optics for decades. Here we will discuss it using the terminology of photonic crystals to gain insight into fundamental processes that will help us later in the understanding of more complex higher dimensional photonic crystal structures.

Basically, we have two types of variable parameters in a Bragg mirror. First, the refractive indices n_1 and n_2 of the two materials and second, the thicknesses d_1 and d_2 of the two layers within the unit cell. More generally, we can speak of material and geometry parameters that are responsible for the optical properties.

First, we want to keep the geometry fixed, using a lattice constant a and two layers with thickness $a/2$ forming the unit cell, and study the influence of the refractive indices on the bandgap which is characterised by its relative width $\Delta\omega/\omega_c$. Before we calculate bandstructures for different sets of refractive indices, we can obtain some more information out of the structure of the master equation. If we multiply the dielectric distribution $\epsilon(\vec{r})$ by a constant factor α or, equivalently the refractive index by $\sqrt{\alpha}$, we see that the only consequence would be a scaling of the eigenfrequencies ω by $\sqrt{\alpha}$. However, this constant factor will be absorbed in the fractional expression in $\Delta\omega/\omega_c$. This means that every dielectric structure with the same refractive index contrast n_2/n_1 will produce the same relative gap width, and we can resort to discussing n_2/n_1 instead of n_1 and n_2 independently.

Now we want to see the quantitative influence of the refractive index contrast n_2/n_1 (we always assume $n_2 > n_1$ and, respectively, $n_2/n_1 > 1$).

Fig. 3.3 shows the relative gap width $\Delta\omega/\omega_c$ in dependance on n_2/n_1 , as well as frequencies of the upper and lower edges for $n_1 = 1.0$. We can see that the relative gap width increases strongly with the index contrast for $n_2/n_1 \approx 3.5$, and then starts to

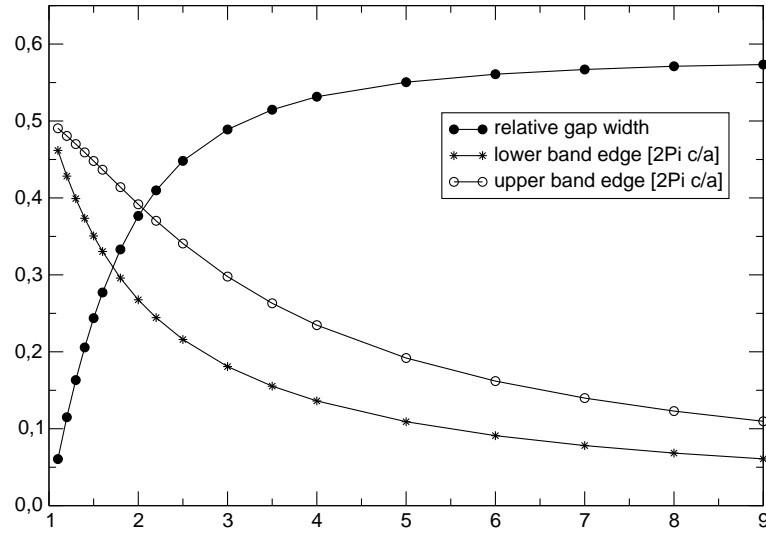


Figure 3.3: $\Delta\omega/\omega_c$, upper and lower bandedge for layers with equal thickness dependent on n_2/n_1

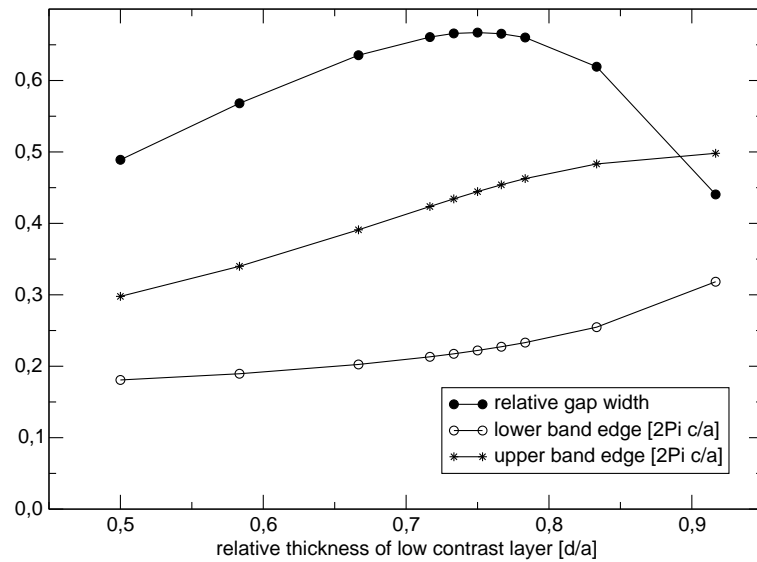


Figure 3.4: $\Delta\omega/\omega_c$, upper and lower bandedge dependent on d_1/a for $n_2/n_1 = 3.0$.

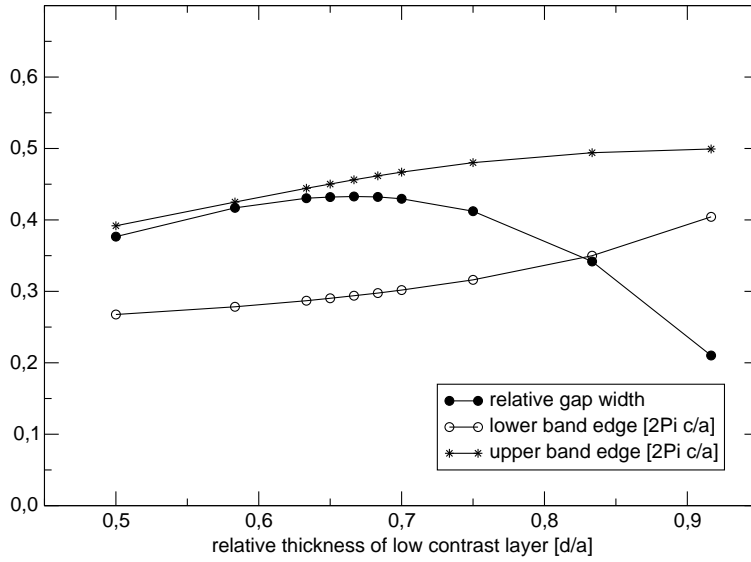


Figure 3.5: $\Delta\omega/\omega_c$, upper and lower bandedge dependent on d_1/a for $n_2/n_1 = 2.0$.

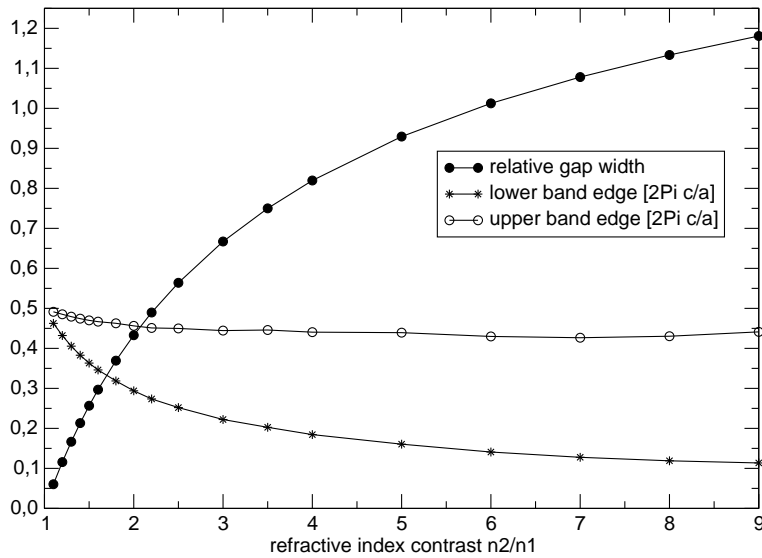


Figure 3.6: $\Delta\omega/\omega_c$, upper and lower bandedge dependent on n_2/n_1 for $n_1d_1 = n_2d_2$.

saturate. This can be explained qualitatively like that: In 3.1.4 we have identified the origin of the bandgap as a degeneracy splitting of modes that are predominately localised in high or low dielectric material. For increasing index contrast this is still the case, but both modes now tend to localise more and more in the high index material. Above a certain level of index contrast a further increase does not have a large effect because the modes are already nearly completely localised in the the high index material. The route to solve this problem is obvious: We should give the modes more room to localize in the low index material. This can be done by modifying the thickness of the layers, making the high index layer thinner in favour of the low index layer. As we normalize frequencies to $2\pi c/a$, we keep the lattice constant $a = d_1 + d_2$ constant. To verify this we calculate $\Delta\omega/\omega_c$ for different values of the relative thickness of the low index layer d_1/a with fixed $n_2/n_1 = 3.0$ (fig. 3.4) and $n_2/n_1 = 2.0$ (fig. 3.5). The maximum gap widths correspond to $d_1/a = 0.75$ ($n_2/n_1 = 3.0$) and $d_1/a = 0.666$ ($n_2/n_1 = 2.0$). These values fulfill the condition $n_1 d_1 = n_2 d_2$ that is well known in classical optics as the matching of the optical path lengths in both layers. When we now use this condition for calculating the gap width in dependence of n_2/n_1 we end up with the optimum result in fig. 3.6. This result is not new and was known long before photonic crystals became an active scientific topic. However, it shows the importance of the synergy between material and geometrical properties when designing structures with a bandgap. The understanding of the mechanisms that lead to a maximum bandgap are much more difficult in higher dimensions because of the higher number of degrees of freedom (especially in geometry and polarisation), but the principles are the same.

3.3 Two-Dimensional Photonic Crystals

In this section we will discuss basic properties of two dimensional photonic crystals (2D-PC). Therefore we will present typical 2D-PC structures and corresponding numerical results for bandstructures and eigenmodes. Furthermore we will analyze in more detail the bandstructure and the parameter dependencies of the hexagonal hole array, which is essential for later parts of this work.

The precise definition of a two dimensional photonic crystal we use here consists of two parts: First, a dielectric constant that is periodic in 2D and translationally invariant perpendicular to the in-plane periodicity.

$$\epsilon(\vec{r}_{xy}, z) = \epsilon(\vec{r}_{xy} + \vec{R}_{xy}, z) \quad (3.40)$$

$$\epsilon(\vec{r}_{xy}, z) = \epsilon(\vec{r}_{xy}, z + \delta z) \quad (3.41)$$

We will associate the x-y-plane with the crystal plane and the z-direction as translationally invariant. Second, we will restrict our analysis to in-plane propagation.

$$k_z = 0 \tag{3.42}$$

For out-of-plane propagation the in-plane bandgap closes for a certain value of k_z . Details can be found in [16].

3.3.1 Basic Structures and Properties

Even if we restrict ourselves to using two different materials only, the possibilities of designing a two dimensional photonic crystal are immense. There has been large effort of testing various lattices and unit-cells in search of an optimum bandgap or other optical properties of interest. Without achieving a comprehensive quantitative understanding yet, some general rules have been established that determine the bandgap:

Brillouin Zone and Index Contrast

Within the x-y-plane a directional gap exists in each direction because there is always some kind of one dimensional periodic modulation and a one-dimensional photonic crystal always has a gap (see 3.2). To obtain an omni-directional gap there must be an overlap of all directional gaps. This is clearly very difficult to realize if the directional gaps are too small. This implies that there is a minimum index contrast $n_2/n_1 > 1$ that is required to obtain a gap. The overlap of the directional gaps may be achieved more easily if the k-values along the edge of the Brillouin-zone do not differ too much. This calls for a Brillouin zone that is as circular as possible.

Polarization Dependence

In 3.2 we learned that the origin of a bandgap is the degeneracy splitting of modes whose energies are localized stronger or weaker in the high dielectric medium. We will now see that this has consequences for the topology for gaps of different polarization. Let's assume a dielectric interface at $x = x_0$ with

$$\epsilon(x < x_0) > \epsilon(x > x_0) \tag{3.43}$$

To understand the behaviour of the electric energy $\epsilon(\vec{r}) \left| \vec{E}_k^\omega(\vec{r}) \right|^2 = \vec{E}_k^\omega(\vec{r}) \vec{D}_k^{*\omega}(\vec{r})$ (the * denotes the complex conjugate) of a mode at this interface we have to distinguish between the electric fields polarized perpendicular or parallel to the interface. As $E_{||}$ is continuous at x_0

$$\epsilon(x_0 - \delta x) \left| \vec{E}_{k,\parallel}^\omega(x_0 - \delta x) \right|^2 > \epsilon(x_0 + \delta x) \left| \vec{E}_{k,\parallel}^\omega(x_0 + \delta x) \right|^2 \quad (3.44)$$

which means the energy discontinuously decreases at the interface to the low index material. For E_\perp we recall that now the dielectric displacement $\vec{D} = \epsilon \vec{E}$ is the continuous variable and therefore

$$\epsilon(x_0 - \delta x) \left| \vec{E}_{k,\perp}^\omega(x_0 - \delta x) \right|^2 < \epsilon(x_0 + \delta x) \left| \vec{E}_{k,\perp}^\omega(x_0 + \delta x) \right|^2 \quad (3.45)$$

which means the energy discontinuously increases. The first case is obviously more suitable for a strong confinement in the high index material. In terms of two dimensional photonic crystals we can use this for finding optimal topologies for gaps of different polarizations. We have to avoid interfaces with respect to the perpendicular E-field component. This is the case for isolated high dielectric scatterers and TM-polarization, and for interconnected high index dielectrics with low index scatterers (inverse structures) and TE-polarization. We will demonstrate this now for typical structures.

Square Lattice of High Index Cylinders Surrounded by Air

As an example we consider a square arrangement of cylinders with refractive index $n = 3.0$ and radius $r = 0.2a$ in air. Fig. 3.7 (top) shows a schematic picture of the crystal with a primitive unit cell, the lattice vectors \vec{R}_1 and \vec{R}_2 , lattice constant a and cylinder radius r . The corresponding reciprocal lattice is depicted in fig. 3.7 (bottom). The inset shows the Brillouin zone constructed from the reciprocal lattice vectors G_1 and G_2 as Wigner-Seitz cell of the reciprocal lattice. The Brillouin zone is quadratic and therefore has additional symmetries that will reduce the part of k -space that has to be considered. The light grey triangle is the smallest area that can be mapped to the whole Brillouin zone by mirror- or rotation-operations and contains all non-redundant information. This smallest possible part is called the irreducible Brillouin zone. It is limited by the high symmetry points Γ , X and M . We already know from one dimensional examples that bandgaps will appear at the border of the Brillouin zone. Therefore it is sufficient to calculate the bandstructure for a closed path along the lines connecting the high symmetry points. Fig. 3.8 shows a calculation for TE- and TM-bands done by a finite-difference time-domain (FDTD) method. As expected from the general arguments in 3.3.1 a TM-gap appears for frequencies from 0.321 to 0.441, while there is no TE-gap. The TM-gap has a relative width $\Delta\omega/\omega_c$ of 31.5% and is limited by the first band at the M -point and by the second band at the X -point. There is also a small directional gap in Γ - X -direction for TE-modes. To explain the appearance of the gaps according to 3.3.1 we will now analyze the distribution of the electric energy $\epsilon(\vec{r}) \left| \vec{E}_k^\omega(\vec{r}) \right|^2$ of the first two TE- and TM-bands at the X -point. Fig. 3.9 shows the energy for the first TM-band

within one primitive unit cell (Here and in all upcoming intensity plots, bright shading indicates high intensity values and dark shading low intensity values). As \vec{E} points along the cylinder axis and therefore always parallel to the dielectric interface, the energy can be confined very strongly in the region of high-index dielectric material. Consequently, this leads to the lowest frequency in the eigenvalue spectrum. A mode of higher order will now require an additional node in the crystal plane, because there is no additional degree of freedom due to the quasi-scalar character of the z-polarized electric field. This nodal line, as can be seen in fig. 3.10 has to go through the center of the cylinder because the mode has to be orthogonal to the first one. This pushes a significant part of the energy out of the high dielectric into the air region and causes an energy shift that leads to the large gap observed in fig. 3.8.

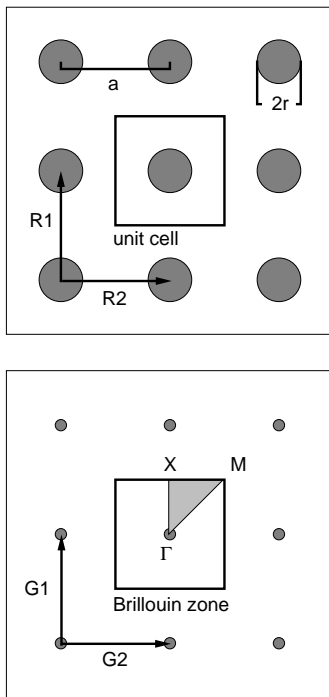


Figure 3.7: Top: Real space lattice. Bottom: Reciprocal space lattice.

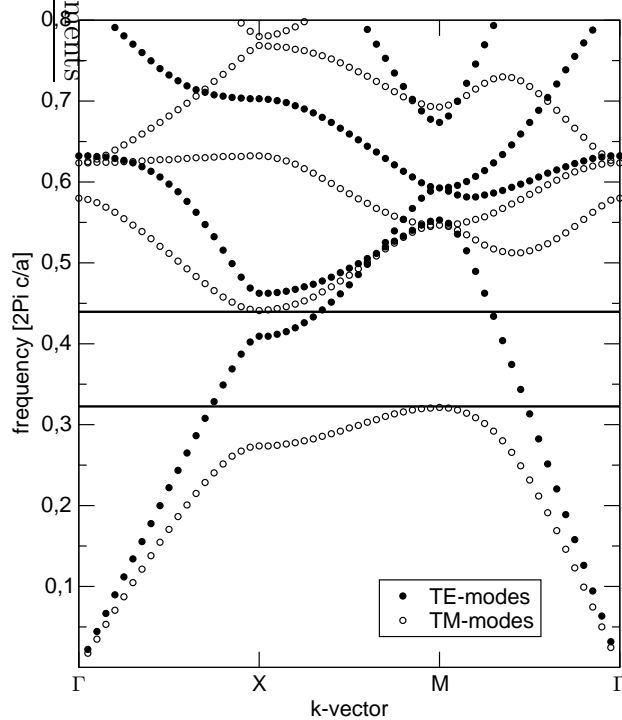


Figure 3.8: Bandstructure for a square lattice of $n = 3.0$ cylinders with radius $r = 0.2a$ in air.

The situation, however, is different for TE-modes. As the electric field vector lies in the crystal plane there are additional possibilities for the energy to localise. The electric field vector can be orientated perpendicular or parallel to the interface. For the lowest

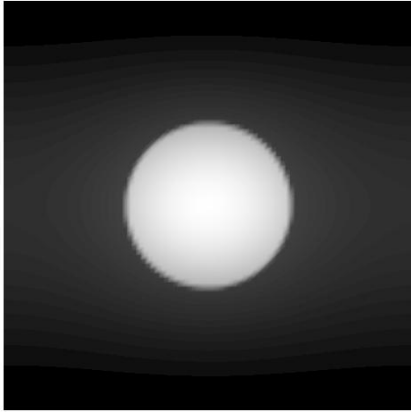


Figure 3.9: Electric energy at the X -point for the first TM-band.

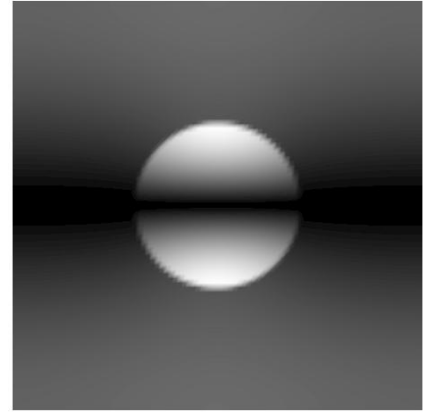


Figure 3.10: Electric energy at the X -point for the second TM-band.

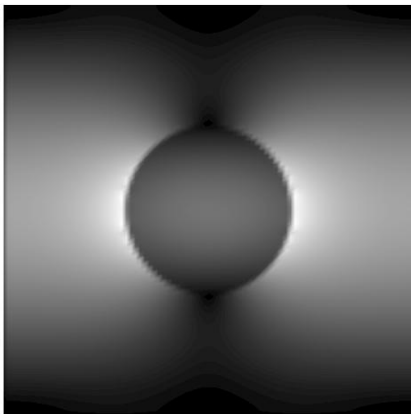


Figure 3.11: Electric energy at the X -point for the first TE-band.

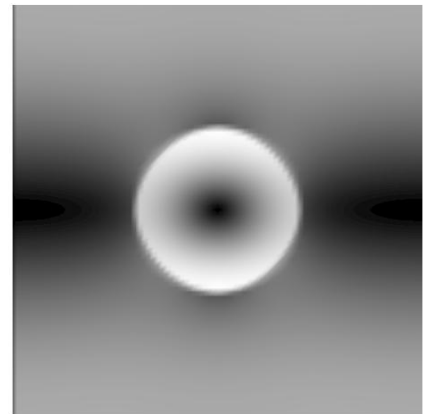


Figure 3.12: Electric energy at the X -point for the second TE-band.

order mode in fig. 3.11 the field lines tend to be parallel (high contribution of the first order plane wave). This indicates a perpendicular crossing at two sides of the cylinder. The corresponding discontinuous increase of the energy is clearly observed in fig. 3.11. This causes a high localization in the low-index dielectric. The second order band in fig. 3.12 has a more complex structure in the field distribution and an even higher low index localization. However, the difference to the first order band is obviously much smaller than in the TM-case.

Hexagonal Lattice of Air Holes in a High Dielectric Background

Following our argumentation that interconnected structures provide TE-gaps and isolated structures TM-gaps, we now try to find a compromise to achieve a polarisation independant gap. This can be done by using an inverse structure with large airholes that nearly touch each other.

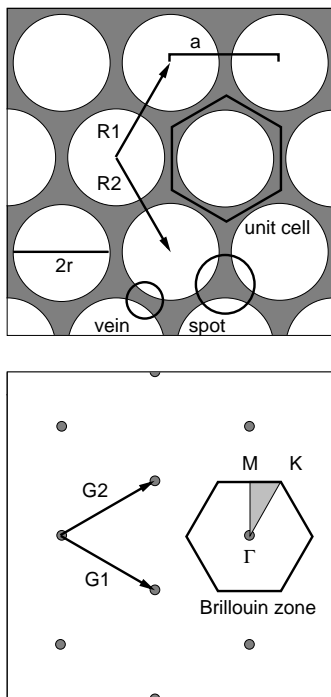


Figure 3.13: Top: Real space lattice. Bottom: Reciprocal space lattice.

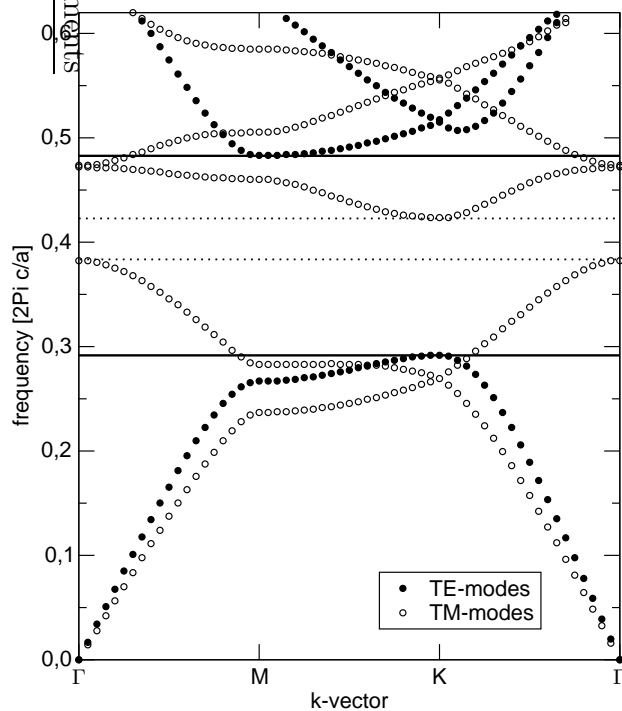


Figure 3.14: Bandstructure for a hexagonal lattice of air holes with radius $r = 0.45a$ in a $n = 3.6$ backbone.

Moreover, we now use an hexagonal lattice, that renders the Brillouin zone more circular

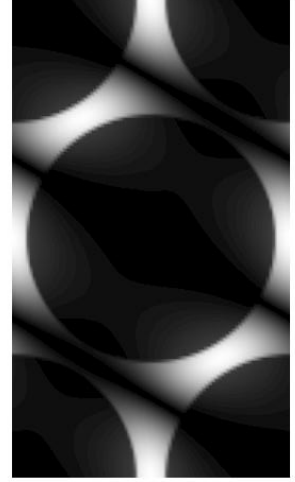
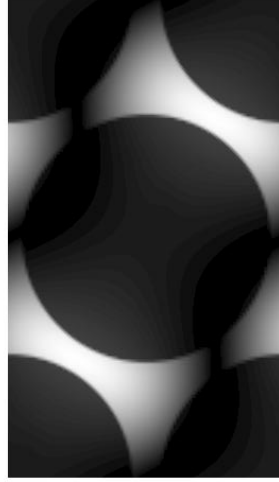
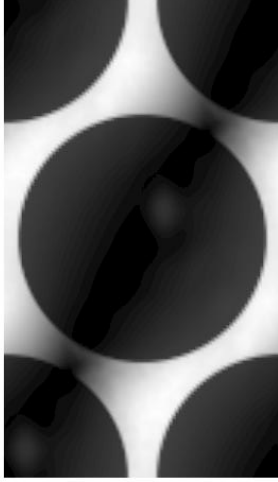


Figure 3.15: 1st TM at M

Figure 3.16: 2nd TM at M

Figure 3.17: 3rd TM at M

than in the square lattice. These considerations lead to the structure shown in fig. 3.13 (top). The high dielectric material consists of spots that are interconnected by thin veins in a way such that each hole is surrounded by six veins and spots. The insets also show the primitive unit cell, the lattice vectors R_1 and R_2 and the parameters r and a . In fig. 3.13 (bottom) the reciprocal lattice is displayed with insets of the Brillouin zone, the irreducible Brillouin zone with high symmetry points Γ , M and K , and the reciprocal lattice vectors G_1 and G_2 . As an example we choose a high dielectric background $n = 3.6$ and holes with $r = 0.45a$. The corresponding bandstructure is shown in fig. 3.14. We can see a large TE-bandgap from 0.292 to 0.483 with $\Delta\omega/\omega_c = 49.3\%$ and a smaller TM-bandgap from 0.382 to 0.424 with $\Delta\omega/\omega_c = 10.4\%$. The TE-gap is limited by the first band at the M -point and the second band at the K -point, the TM-gap by the second band at Γ and the third band at K . To analyse the origin of these gaps we now study the energy distribution at selected points, starting with the TM-modes.

Similar to the square lattice the only way to create higher modes for TM-polarization is by adding node planes. Fig. 3.15 shows the first TM-mode at the M -point that strongly localizes its energy in the dielectric veins and spots, beside one node plane that crosses two veins. The second band (fig. 3.16) adds one more node plane that also crosses veins. The third band contains three nodal planes (fig. 3.17) that cross the dielectric spots (and also run through two veins). As significantly more energy can be stored in a spot than in a vein, the change in energy is much larger between the second and the third band compared to the first and second. This is reflected in the bandstructure by the frequencies at the M -point but also in the fact that the TM-gap rises between band two and three and not between 1 and 2 as for the TE-modes.

Now we discuss how strong the size of the air-holes influences the width of the bandgap. We therefore focus on the modes that limit the bandgap.

In fig. 3.18 and 3.19 we see modes that have a high six fold symmetry in the distribution of the electric energy. At the Γ -point the energy is strongly localised in the dielectric spots while at the K -point the energy is concentrated in the veins with nodes in the spots. The localisation in the thin veins pushes some energy into the air regions and causes an increase in frequency which results in a gap. Following these qualitative arguments, the upper bandedge should consequently be more sensitive to changes in the radius of the airholes because this causes a larger relative change in the areas where the energy is concentrated as illustrated by comparison of fig. 3.19 and fig. 3.20 where the upper edge mode is shown for different radii. If the veins have a similiar thickness than the spots, the gap should vanish.

Now we want to discuss the TE-modes of the hexagonal structure. This is done in more detail because later we will focus on this particular system. Fig. 3.14 shows that the TE-gap is much larger than the TM-gap. For the parameters used in fig. 3.14 we obtain a TE-gap of 49.4%. The gap is limited at the lower edge by the first band at the M -point and at the upper edge by the second band at the K -point. Therefore we will now look closer at these two modes and for illustration also at the first band at M .

Fig. 3.21 shows the electric energy for the first band at M and radius $0.45a$. The energy is well localised in the dielectric regions and the continuity behaviour shows that the electric field is parallel to the dielectric interfaces. Therefore only little energy is stored in the air regions. The second band at the same point displays a completely different picture (fig. 3.22): At two positions the field lines cross the interface perpendicular, leading to significant energy in the holes. Moreover, there are node planes in some of the dielectric veins and nodes. The additional degree of freedom due the polarization leads to a large difference in energy localisation and therefore in the frequency eigenvalues. The mode that represents the upper band edge (fig. 3.23) has similiar properties as fig. 3.21 beside a different symmetry due to the different k-vector. What happens if we change the radius of the air hole? For both bands frequencies will decrease due to the higher effective refractive index. The effect on the second band is larger because the relative volume of air decreases and therefore also the possibility of storing energy there. In the modes of the first band nearly the whole energy is already stored in the high index material and adding more material will not strongly improve this. As the frequency of the upper edge decreases stronger than the frequency of the lower edge the relative width of the bandgap also becomes smaller. This is illustrated in fig. 3.24 to 3.26 (energy distribution) and fig. 3.30 (bandstructure) for radius $0.33a$. In comparison to the case with $r = 0.45a$ the relative decrease is 37.8% for the upper edge frequency and 28.6% for the lower edge frequency while the relative bandwidth decreases to 36.3%. Compared to the structures and polarisations discussed so far, the TE-gap in the inverse hexagonal structure is very robust and exists for a large range of frequencies. If we further decrease the radius we have to go until $r = 0.13a$ to destroy the gap. This

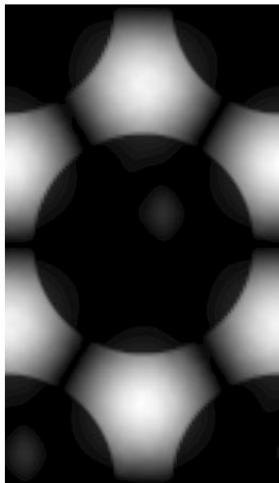


Figure 3.18: 2nd TM at Γ ,
 $r = 0.4a$

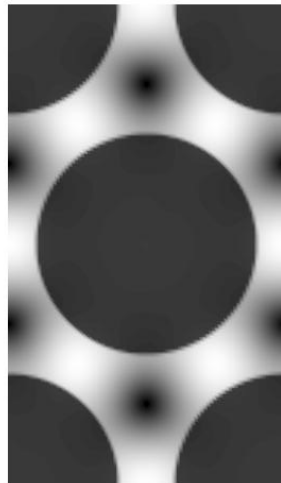


Figure 3.19: 3rd TM at K,
 $r = 0.4a$

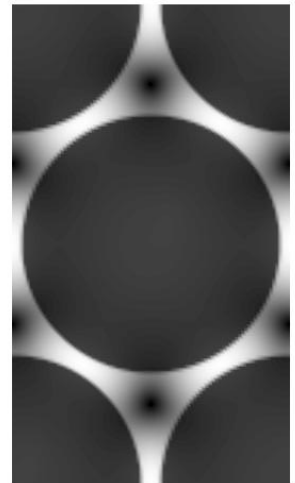


Figure 3.20: 3rd TM at K,
 $r = 0.47a$

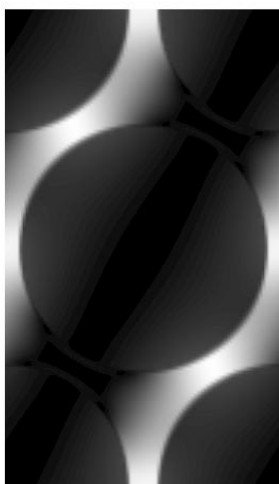


Figure 3.21: 1st TE at M,
 $r = 0.45a$

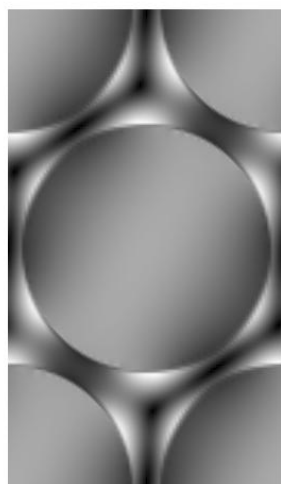


Figure 3.22: 2nd TE at M,
 $r = 0.45a$

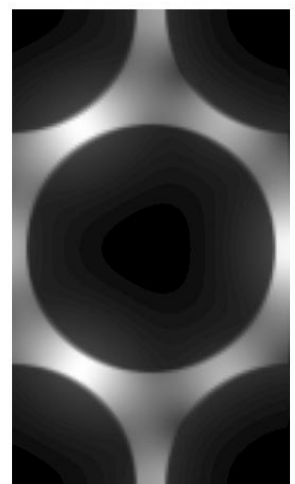


Figure 3.23: 1st TE at K,
 $r = 0.45a$

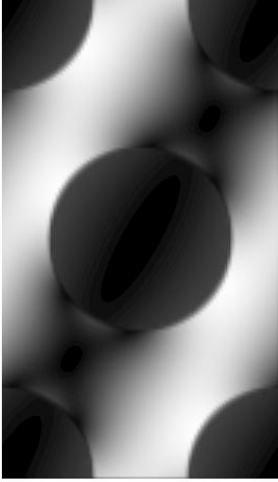


Figure 3.24: 1st TE at M,
 $r = 0.33a$

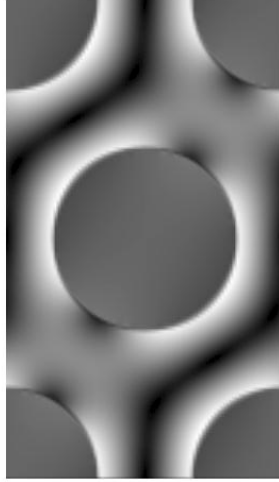


Figure 3.25: 2nd TE at M,
 $r = 0.33a$

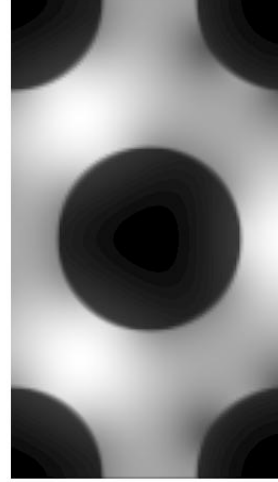


Figure 3.26: 1st TE at K,
 $r = 0.33a$

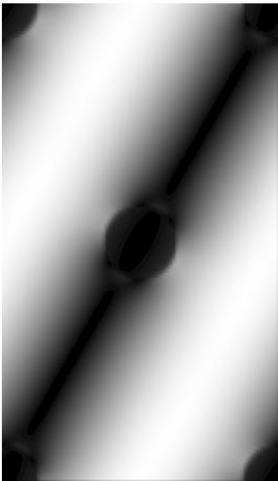


Figure 3.27: 1st TE at M,
 $r = 0.13a$

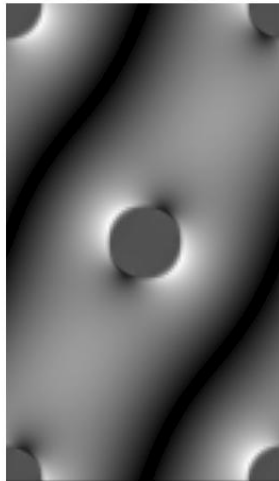


Figure 3.28: 2nd TE at M,
 $r = 0.13a$

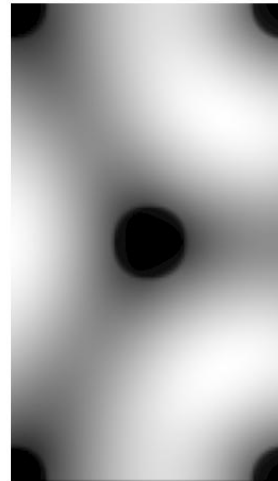


Figure 3.29: 1st TE at K,
 $r = 0.13a$

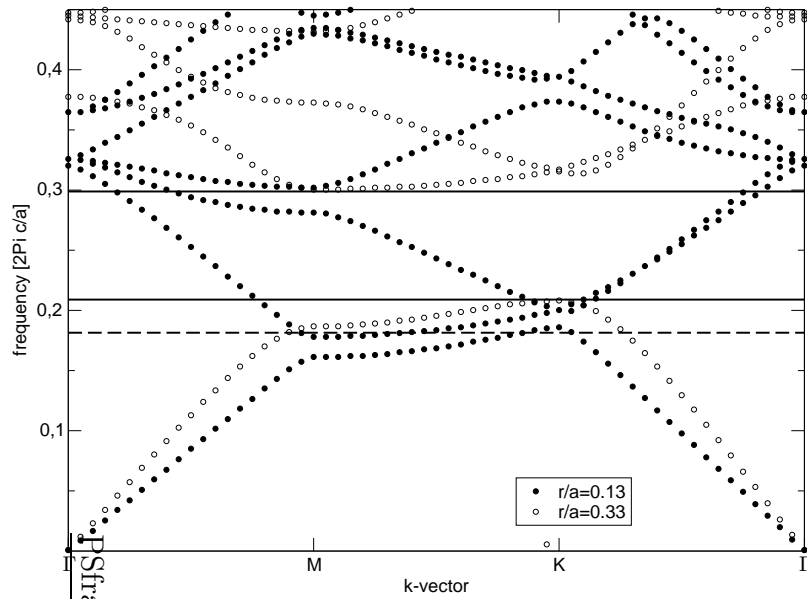


Figure 3.30: Bandstructure for TE-modes for structures with varying radius

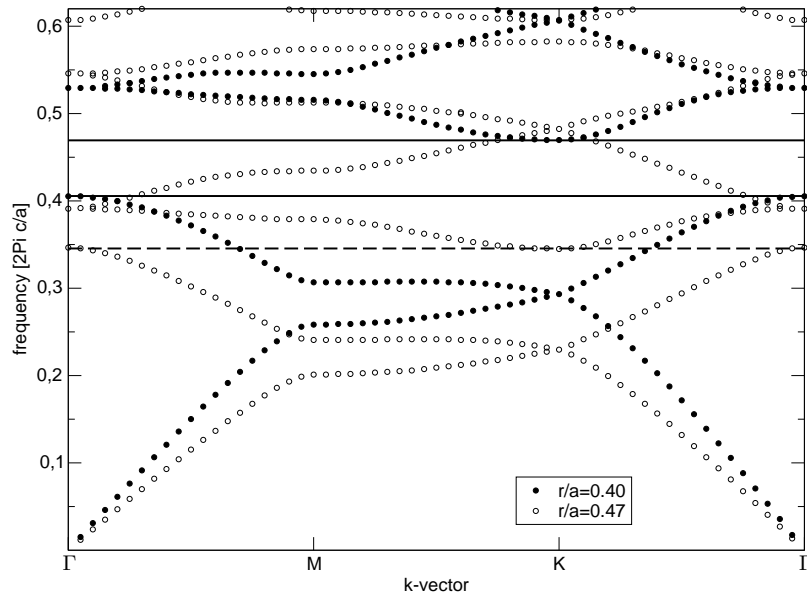


Figure 3.31: Bandstructure for TM-modes for structures with varying radius

is presented in fig. 3.30 and fig. 3.27 to 3.29. In the energy distribution we see that the perturbation of the dielectric by the hole becomes so small that the character of the light is nearly that of a plane wave.

In contrast, the TM-gap is much less robust, as can be seen in fig. 3.31 where we compare the TM-bands for radii $0.40a$ and $0.47a$. The relative change in the lower edge frequency is 14.5% while the upper edge frequency changes by 26.6%. For $r = 0.47a$ this results in a gap width of 14.7% while for $r = 0.40a$ the gap just closes.

In the last two sections the application of the general principles of 3.3.1 has been demonstrated. However, even for basic structures and the lowest order bands, it is already difficult to analyse the complicated mode structures. It has become clear that the general principles may only work as qualitative guidelines but cannot replace numerical analysis whenever quantitative information is required.

3.4 Defects

The availability of structures where no propagation is allowed has led to many interesting suggestions for applications and devices (e.g. as mirrors for lasers [17]) as well as the novel propagation properties of the photonic crystal bands (e.g. superprisma [18]). However, the largest field of applications opens up by the controlled introduction of defects into the perfect periodic structure that creates well defined and strongly localised states within the bandgap. The qualitative understanding why local deviations from the perfect crystal can trap light is easy, because one can just imagine semi-infinite crystals that act as perfect mirrors and are brought together in a way such that they surround a small region. If defects with well defined properties (e.g. a certain frequency or mode profile) are required a deeper understanding of the mechanisms that lead to a defect mode is necessary, especially because the possibilities of locally disturbing the lattice are large. It can be done by modifying the material, the geometry or the lattice itself. Generally, the introduction of a defect destroys the periodicity of the crystal. In systems of higher dimensionality this not necessarily needs to be done in all dimensions. Indeed, we can classify the type of defect by the number of dimensions in which the periodicity is broken. In an i -dimensional system a point-defect will destroy the discrete translational symmetry in i directions, a line-defect in $i - 1$ directions and a planar defect in $i - 2$ dimensions. Therefore point defects can appear in 1-, 2- and 3-D systems, line defects in 2- and 3-D and planar defects only in 3-D. In the following sections we will discuss the creation of defects of various types in some example systems. We will not address defects in three dimensional systems because they have not yet reached technological relevance because of experimental difficulties, but there has been important recent progress by applying direct laser writing in polymers [11].

3.4.1 Point Defects in 1D

The super-cell concept

Before we start analysing defects we will introduce a concept that helps understanding the physical mechanisms leading to defect creation as well as being useful for numerical calculations. When defining the lattice vectors \vec{R}_i and the concept of bandstructure in 3.1.2 and 3.1.3 we have assumed that \vec{R}_i are primitive lattice vectors referring to a primitive unit cell, leading to the largest possible Brillouin zone. For the concept of bandstructure this is convenient because an unnecessary backfolding can cause confusion. Mathematically, however, it is not necessary. We can also choose a non-primitive unit cell, from now on called super-cell, (in 1D e.g. $l \cdot a$ long) and calculate the corresponding vectors of real ($\vec{R} \cdot l$) and reciprocal space (\vec{G}/l) as well as the now (l -times) artificially backfolded bandstructure. Fig. 3.32 shows an example of this procedure for a simple Bragg-mirror with $n_1 = 1.0$, $n_2 = 2.0$, $d_1 = 2a/3$, $d_2 = a/3$ and $l = 11$. In the ideal system this formal change is trivial and not beneficial. However, if we now change for example the thickness of one layer and thereby create a point defect, we destroy the \vec{R} -periodicity but still have the $\vec{R} \cdot l$ -periodicity. The system now consists effectively of a periodic arrangement of defects within a background one dimensional crystal. The solutions of this system are not the same as of the perfect defect structure that would be a single defect in an infinitely extended crystal. However, we can argue that the defect mode is strongly localised to the spatial perturbation and if the distance between two defects (which is essentially the size of the supercell) is large enough that the eigenfunctions of the single defects do not overlap, the eigensolutions are the same as in the ideal case. We therefore can calculate the defect modes and frequencies without losing the benefits of working with a periodic system.

High and Low Index Defects

Using the supercell method we will now investigate the physical origin of pointlike defects in the one dimensional example mentioned in the last section. The energy distribution at the lower and the upper edge of the bandgap are shown in fig. 3.32 as well as the dielectric structure.

We now perturb the crystal by making the central high dielectric layer $dx = 0.1a$ thicker. As adding high dielectric material decreases the frequencies and we look for modes in the bandgap we examine the influence on the upper bandedge mode. Fig. 3.33 (left) shows the supercell bandstructure of the defect system and we can observe two effects. First, at the edges of the supercell Brillouin zone small bandgaps appear. This is due to the small modulation with period $l \cdot a$ that is caused by the periodic defects. These gaps are artificial ones due to the supercell method and have no further relevance for our discussion. Second, the lowest branch of the second band of the unperturbed crystal is moving downwards into the gap and flattens, but still has a small non zero group

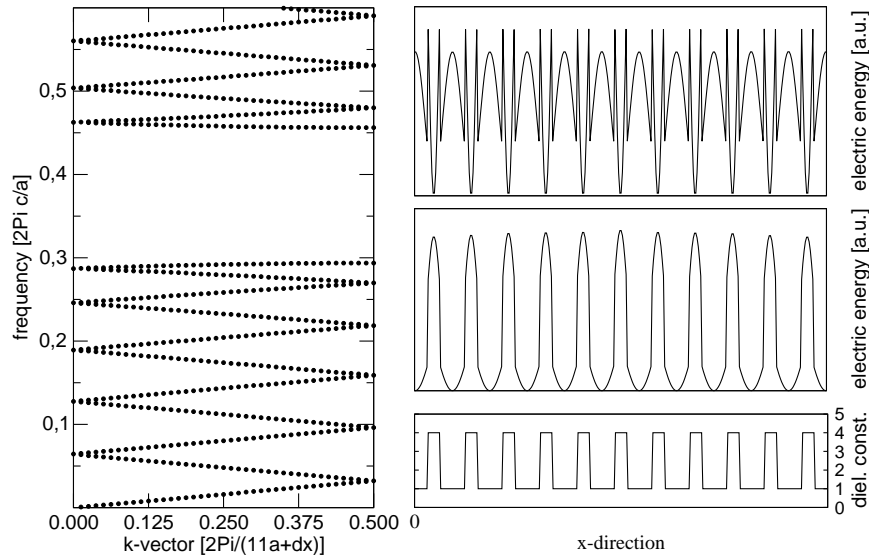


Figure 3.32: Bandstructure (left), upper edge mode (right,top), lower edge mode (right, center) and dielectric distribution (right, bottom) for a $11a$, $dx = 0$ supercell.

velocity. The distribution of the electric energy of this mode in fig. 3.33 (right, top) shows already a localisation to the defect, but the additional high index material is not yet sufficient to make the exponential decrease away from the defect fast enough to inhibit interaction with the periodic continuation of the supercell. This is achieved in the next example (fig. 3.34) for $dx = 0.333a$ where we can associate the defect mode with a constant frequency 0.3734 which results in a vanishing group velocity and therefore pointlike localisation. A stronger localisation to the defect can also be achieved by increasing the refractive index contrast of the background photonic crystal. This is illustrated in fig. 3.35 for an example with the same geometrical setup as in fig. 3.33 with a high index material with $n = 3.0$. Besides the stronger localisation the defect frequency is also pushed away stronger from the bandedge.

We can also create a defect by decreasing the refractive index in one layer or, which is effectively the same, make the high dielectric layer in the center of the supercell thinner. In this case, the origin of the localised defect mode is the lower edge of the bandgap. This is illustrated in fig. 3.36.

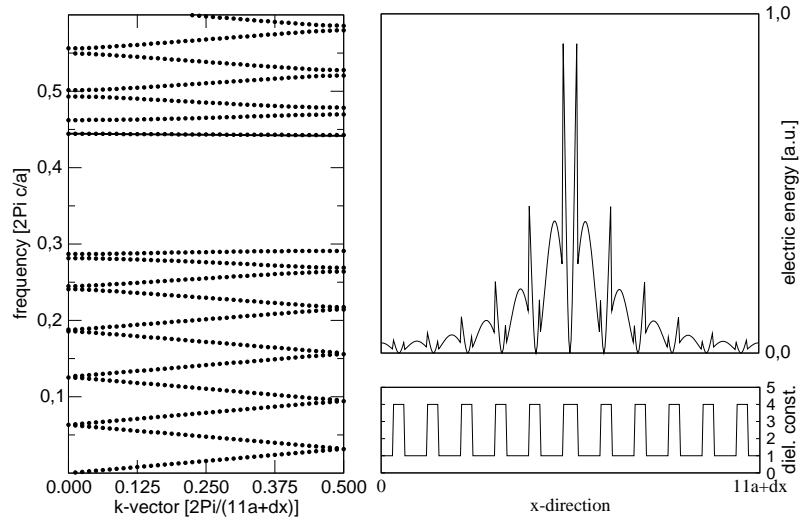


Figure 3.33: Bandstructure (left): defect mode marked by line, defect mode (right,top) and dielectric distribution (right, bottom) for a $11a, dx = 0.1a$ supercell

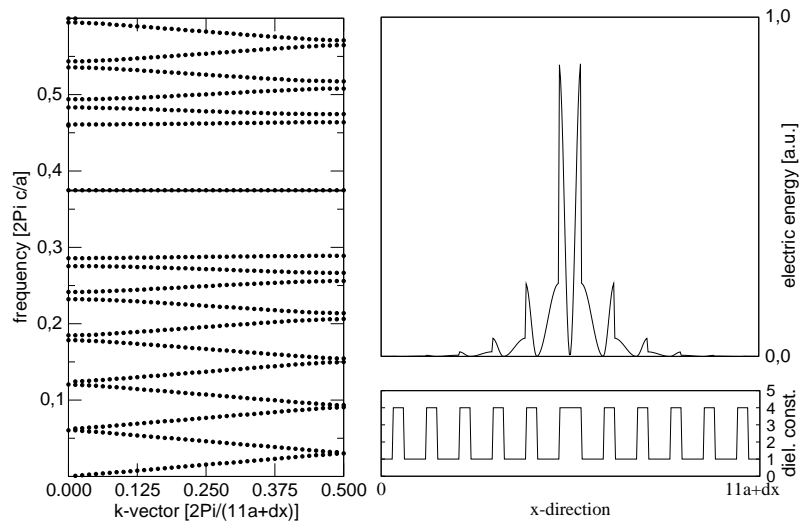


Figure 3.34: Bandstructure (left): defect mode marked by line, defect mode (right,top) and dielectric distribution (right, bottom) for a $11a, dx = 0.333a$ supercell

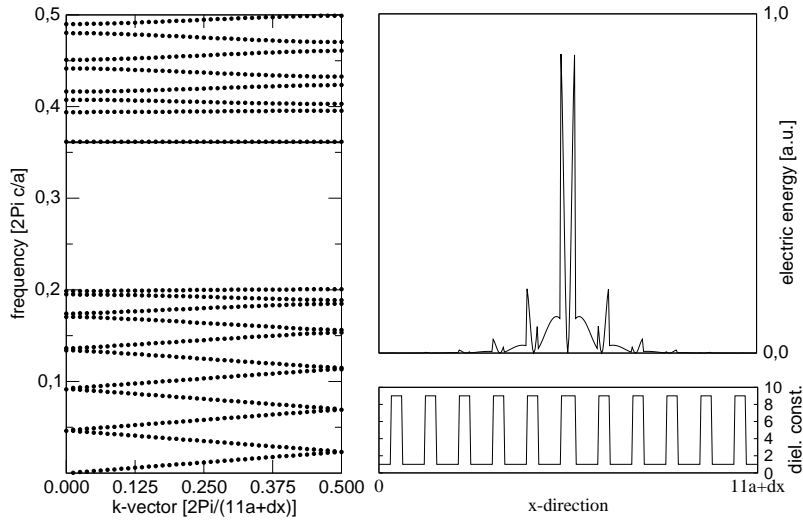


Figure 3.35: Bandstructure (left): defect mode marked by line, defect mode (right,top) and dielectric distribution (right, bottom) for a $11a$, $dx = 0.1a$ supercell

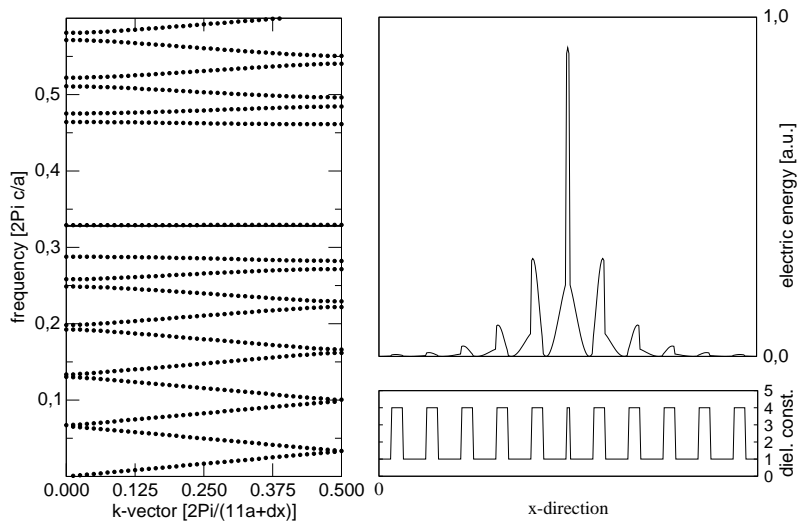


Figure 3.36: Bandstructure (left): defect mode marked by line, defect mode (right,top) and dielectric distribution (right, bottom) for a $11a$, $dx = -0.233a$ supercell

In summary:

- Locally decreasing the refractive index results in a defect mode that is deducted by the lower band edge while increasing the refractive index results in a defect mode deducted from the upper band edge.
- Small perturbations with defect frequencies close to the band edge have spatially weakly confined modes. This should be noticed when supercell methods are used.
- A higher index contrast of the background crystal enhances the spatial localisation.

3.4.2 Point- and Line-Defects in 2D

For the creation of defects in a two dimensional system there exists a wide range of parameters that can in principal be modified to destroy the periodicity. For example we can locally change the refractive index, the size, shape or symmetry of a scatterer, the lattice constant, the lattice symmetry or various combinations of these parameters. Moreover, we can modify more than one unit cell in the described ways. This list is not comprehensive at all and a systematic analysis of the possibilities would go beyond the scope of this work. In the following we will restrict ourselves to typical examples and show aspects of principal importance.

Point Defects

The simplest way of creating a point defect in a two dimensional crystal is to modify one single scatterer without otherwise changing the symmetry of the lattice. In the fundamental structures already discussed this is usually done by changing the radius of a dielectric cylinder or an air hole, or by entirely removing it. If we take, for example, an inverse hexagonal lattice and remove one hole we have a high dielectric defect that will pull down states from the upper band edge in a qualitatively analogous way as in the one dimensional case. However, the situation is much more complicated now. As the defect structure still has a six-fold rotational symmetry (or C_{6v} in terms of group theory) that allows several types of defect modes, starting with a highly symmetric fundamental mode and several higher order defect modes. However, it is not certain that all modes allowed for symmetry reasons do exist in the bandgap. Detailed analysis shows that it depends strongly on the crystal parameters which modes really appear in the gap. Moreover, the irreducible representations of C_{6v} also allow two fold degenerated modes. We demonstrate this now for a set of typical parameters used in experimental investigations based on *GaAs*-structures (described e.g. in [19]).

We use a supercell with $7 \cdot a$ in x-direction ($\Gamma - K$) and $5 \cdot \sqrt{3}a$ in y-direction ($\Gamma - M$). The high dielectric material has a refractive index of 3.6 and the air holes a radius of 0.266. The hole in the center ($x=0, y=0$) is missing. For these parameters bandstructure

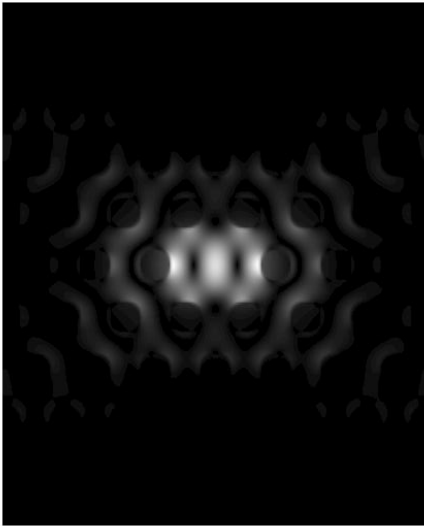


Figure 3.37: Mode 1: Energy.

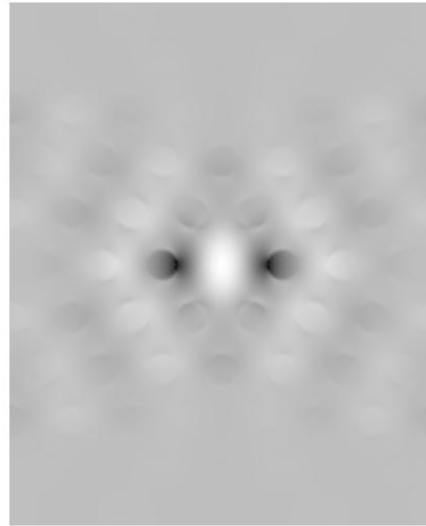


Figure 3.38: Mode 1: E_y .

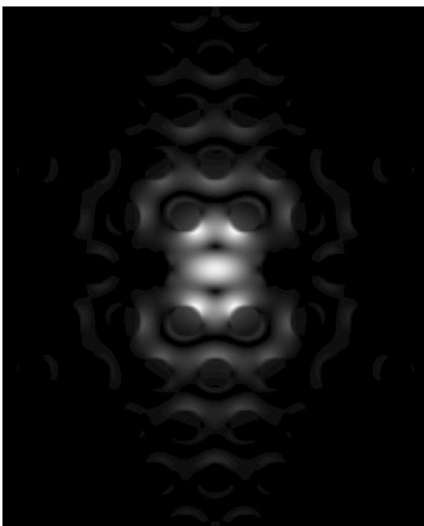


Figure 3.39: Mode 2: Energy

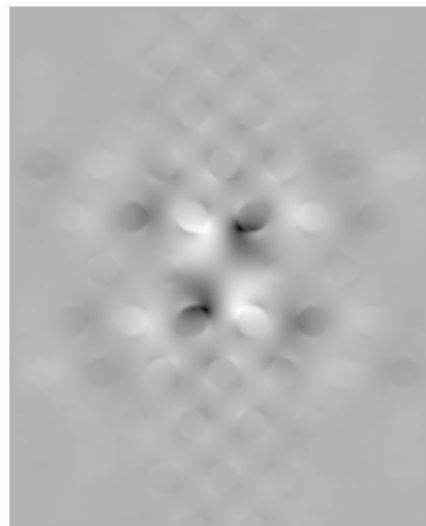


Figure 3.40: Mode 2: E_y .

calculations show only one defect mode lying in the bandgap. Due to the size of the supercell and the being folded back many times bands the band diagram becomes very confusing and yields no additional insights. We therefore do not display it. Practically, if we excite the defect mode by a random initial condition, we do not know if the mode is degenerated or not. A test could be to use a different initial condition which is not linearly dependant on the first. If we get a different result we found a degeneracy and are able to construct a basis for the two-dimensional subspace. We can also get orthogonal basis functions directly if we modify the initial conditions in a way that only modes of certain symmetries are excited. In the hexagonal lattice we have mirror symmetries for $x = 0$ and $y = 0$. We now make use of these symmetries by choosing initial conditions that are odd with respect to either x- or y-mirror-symmetry. The energy distributions for the defect modes are shown in fig. 3.37 and fig. 3.39. In fig. 3.38 and fig. 3.40 the distribution of the E_y component are shown (white represents positive, grey zero and black negative values of E_y , respectively). Mode 1 has even symmetry for both mirror planes while mode 2 has odd symmetry (and vice versa for E_x which is not displayed). This proves that the modes are orthogonal basis functions. The knowledge about this degeneracies led to improvements of certain desired mode characteristics by intensionally lifting this degeneracy by stretching the lattice constant along x- or y-direction [7].

Line Defects

Besides the complete spatial localisation in both dimensions there is also the possibility of breaking the crystal symmetry only in one direction by adding a one dimensional line-shaped defect. This can be done for example by leaving out a row of holes in the inverse hexagonal structure either in Γ - K - or in Γ - M -direction. This can create modes in the bandgap that are localised perpendicular to the line defect but are able to propagate along the defect. These structures are often called photonic crystal waveguides and represent one of the most interesting research fields with respect to practical applications. We will now discuss the principles of a line defect analysis by looking at a Γ - K defect in a hexagonal inverse structure with background index $n = 3.6$ and air holes with radius $r = 0.4a$. Fig. 3.41 shows a line defect structure with the supercell used for the calculations as an inset. Since we are only interested in the defect modes localised perpendicular to the defect we need a sufficient number of primitive unit cells around the defect to separate the infinite number of parallel line defects that effectively exist due to the supercell. Due to the high index contrast background structure a separation of $4 \cdot \sqrt{3}a$ in Γ - M -direction is enough. In Γ - K -direction there is a real physical periodicity but we have to be careful because the K -point is not the same as in the unperturbed structure. In the defect-free structure the distance from Γ to K is $2/3 \cdot 2\pi/a$. By adding a line defect we distinguish one K -direction from the others and therefore all high symmetry-points that limit the BZ have to be projected onto the line-defect-axis to determine the BZ of the defect system. The new BZ is then limited by the projection of a M -point of the unperturbed lattice and the resulting K' has a distance to Γ

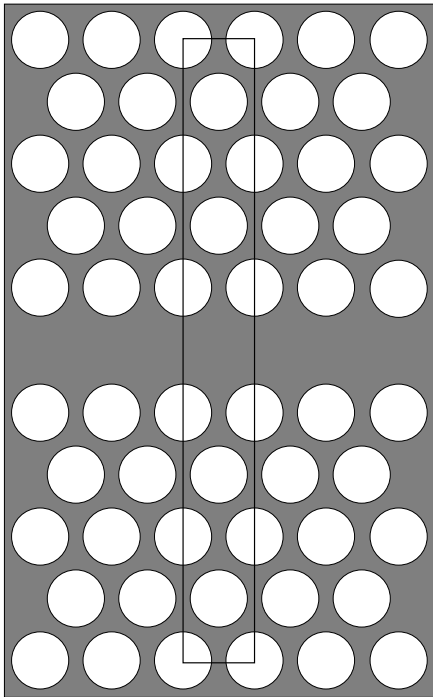


Figure 3.41: Schematic view of the real space defect structure with supercell.

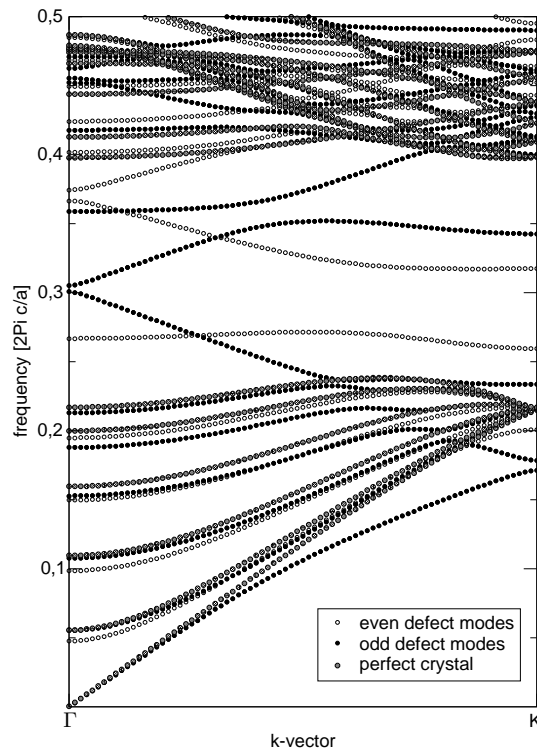


Figure 3.42: Projected bandstructure of a line defect (odd and even modes) with projected bandstructure of the perfect structure

of $1/2 \cdot 2\pi/a$. The same result can be obtained by directly calculating the BZ of the supercell. To calculate the dispersion of the line-defect (waveguide) modes we therefore can restrict ourselves in k -space to the Γ - K' -direction.

Although the translational symmetry in Γ - M -direction is broken there is still a mirror symmetry with respect to the plane spanned by the Γ - K' - and z -direction crossing the defect at the center. We will also classify the defect modes by their odd and even symmetry with respect to this mirror plane. This is important for incoupling problems [20]. Fig. 3.42 shows the bandstructure under the described conditions. For clear distinction of bulk and defect modes the projected bands of the defect-free crystal are also contained. There are six defect modes (three even and three odd) that exist in the gap. Not all have frequencies in the gap for all k -values but enter the bulk modes for some parameters and are therefore not confined anymore by the crystal. It can be clearly seen that odd and even modes do not interact when they cross while modes of equal symmetry show avoided crossing behaviour. Fig. 3.43 shows the spatial distribution of

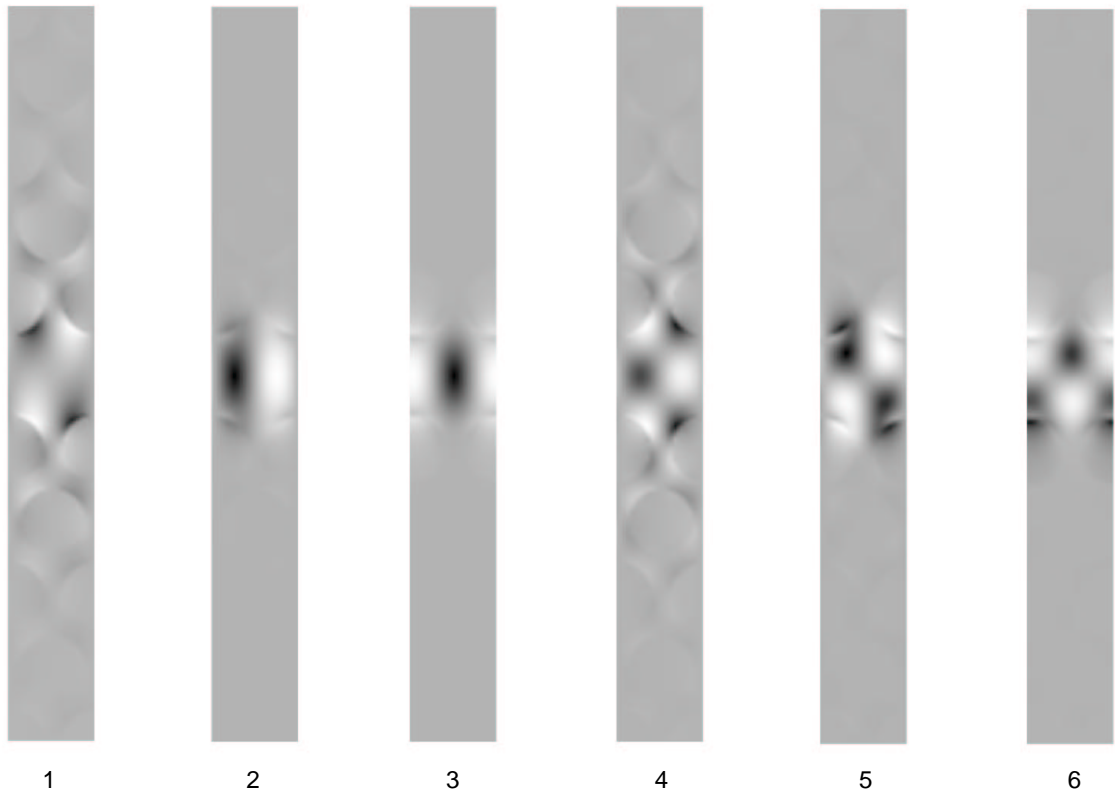


Figure 3.43: E_y -distribution for the six defect modes at Γ in order of increasing frequency.

the E_y (polarised in Γ - M -direction) field component to illustrate mode symmetry and localisation of the defect modes. The modes are numbered by increasing frequency at the Γ -point.

The guiding by the photonic crystal bandgap is not the only mechanism that is responsible for the localisation. As the defect region has a higher effective refractive index than the surrounding hole structure total internal reflection will also contribute. Mode 1 and 4 of fig. 3.43 extend more into the photonic crystal than the others that are strongly localised to the dielectric strip in the center. The explanation is that 1 and 4 are dominantly guided by the crystal while 2, 3, 5 and 6 mainly by total internal reflection. In the literature this is sometimes referred as gap guided and index guided, respectively. This distinction, however, is only qualitatively and reflects only a rough estimate of the dominant mechanism.

3.5 Transmission

The bandstructure and eigenmode calculations presented so far have assumed an infinitely extended crystal (mathematically represented by Bloch's theorem). Obviously, this can never be realised in real applications. An important question is therefore how a finite photonic crystal responds to an external excitation. This aspect is one of the research topics to be addressed in the next chapters in context with realistic three-dimensional systems. Therefore, we will now introduce some basic concepts for a 2D example which will be important for the understanding of more complex systems.

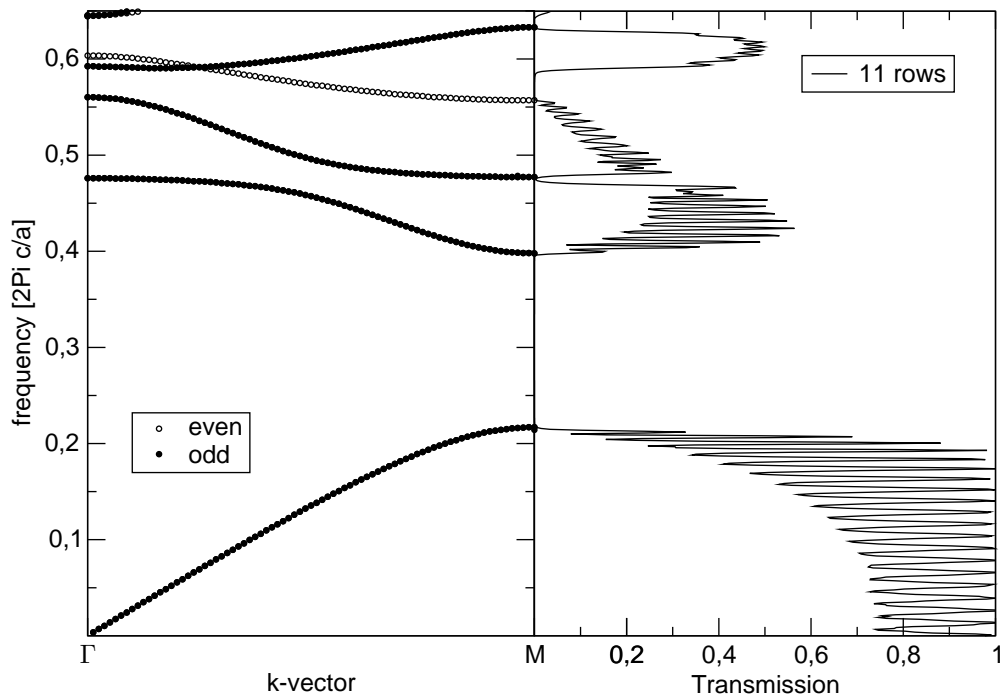


Figure 3.44: Bandstructure (left) and transmission (right) through 11 crystal layers in Γ - M -direction.

Fig. 3.44 compares the bandstructure of the infinitely extended crystal with the transmission through a finite system for a plane wave excitation with normal incidence. The first band directly corresponds to high transmission, only modulated by Fabry-Perot-oscillations that are a result of the finite length of the sample. This can be explained by the large spatial overlap of the plane wave and the first order band because the latter has a large contribution of the lowest order Fourier component. When reaching the

bandgap at frequency 0.22 the transmission becomes smaller. The reason for this is the flattening of the band near the bandedge and therefore a bad coupling due to impedance mismatch of the plane wave and the photonic crystal mode. Similiar arguments hold for the small gap caused by the anticrossing of the second and third band. Above frequency 0.56 there is one more gap in transmission however this is unexspected from the bandstructure because the fifth band (counted at Γ) covers this frequency range. To explain this we compare the field distributions of the E_y -component of the 3rd, 4th and 5th band (fig. 3.45 to 3.47). We can see that band 3 and 4 are odd with respect to the mirror plane spanned by Γ - M and z -direction while band 5 is even. An incoming plane wave has an odd symmetry in this respect. The overlap and therefore the coupling of modes with different spatial symmetry is always zero and consequently band 5 does not contribute to transmission. This result has enormous importance for the interpretation of experimental results. As mentioned earlier it proves that a vanishing transmission (or complementary a reflection equal to 1) is not a commensurate condition for the existence of a bandgap. Moreover, for practical applications there is always an interface between conventional optical components and the photonic crystal. In nearly all systems considered so far only the odd modes can be used due to the symmetry matching problem.

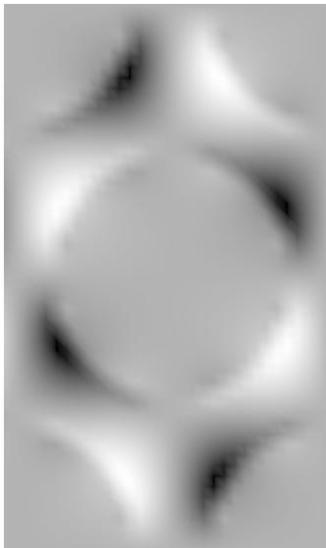


Fig. 3.45: 3rd TE at M, E_y



Fig. 3.46: 4th TE at M, E_y

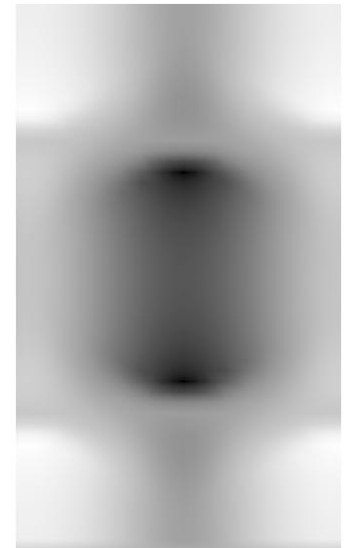


Fig. 3.47: 5th TE at M, E_y

3.6 Conclusion

In this chapter we have derived the master equation of a photonic crystal describing the fundamental properties (bandstructure and eigenmodes) by introducing Bloch's theo-

rem from solid state physics into Maxwell's equations. We have discussed fundamental properties of this equation, especially the energy localisation mechanisms leading to a bandgap, which is a frequency region with vanishing density of states, for several one- and two-dimensional examples by solving the master equation numerically in the framework of a FDTD-algorithm. As the number of degrees of freedom is very large especially in 2D we restricted the discussion of parameter dependencies to a few easy accessible examples like refractive index or layer thickness. Moreover, we utilised some other helpful concepts like the Brillouin-zone, energy localisation, density of states or certain symmetries for a better understanding of the optical properties. The inclusion of point- and linedefects with the result of localised defect modes within the bandgap has been presented in the context of a supercell approach. Finally, we have touched finite systems that may additionally be described by transmission. The concepts presented in this chapter will be extended to more complex systems that resemble reality more closely and are therefore of high practical interest in the next two chapters.

4 Photonic Crystal Slab Structures

4.1 Introduction

The optical properties of two-dimensional photonic crystals presented in the preceding chapter have led to many suggestions of technological applications and devices. Especially in integrated optics there is a large need of basic functionalities like cavities [7] or waveguides [20, 21] that can by the help of photonic crystals be realised by the controlled inclusion of defects on the scale of the wavelength, while other applications like superprisms base on novel refractive properties of the bulk crystal. Moreover, the properties are controlled by the layout of the nano-structuring and not only by microscopic properties of the materials used. This opens up a much larger operating window. Further, the two-dimensional layout assures compatibility with existing on-chip technology and the handling of high index materials like silicon or III-V-semiconductors is well established in the field of semiconductor physics and technology [22, 23, 24]. However, although there is a large library of well-known methods that can be applied there are still many problems to be solved before photonic crystal devices can find their way to the marketplace. Many of them are of experimental nature concerning the accuracy of the patterning, wall roughness, etc. [25, 26]. Others like the efficient in- and outcoupling from conventional optical fibres have to be carefully addressed theoretically. This is not because the physics is unknown, but the complexity of photonic crystal modes exceeds the limits of established approximations like effective index methods. In this section, which represents the central aspect of this work, we want to address a problem which is likely the most essential for the comprehensive understanding and future applicability of two-dimensional photonic crystals, namely the finite size of the crystal structures perpendicular to the crystal plane of real systems and the interaction of the periodic structure with its environment. Fig. 4.1 illustrates a typical structure, a dielectric slab of thickness d , patterned with a hexagonal lattice of holes with radius r . It is obvious that the conditions shown in 3.3 for an ideal two-dimensional system can not be achieved in real life, because the translational invariance in out-of-plane direction does not exist anymore. In fact, we have to deal now with regions "inside" and "outside" of the crystal as well as the interaction of both regions at the interface. This has important consequences: Due to the interaction with the environment the modes of the vertically finite photonic crystal slab may be lossy which means energy is radiated into the environment. In most cases for technological applications this is not desired, so we need mechanisms to keep the light in the crystal. This is mainly done by total internal reflection.

Mathematically this means in one direction we cannot assume periodic boundaries and therefore Bloch's theorem is not applicable in this direction. Moreover, the frequency eigenvalues are not real anymore but complex, with the imaginary part describing the losses that can be seen as an exponential damping in time. The bandstructure introduced in 3.1.3 therefore is not anymore a complete solution of the eigenvalue problem. It still gives important information but now has to be complemented by the lifetime of the modes.

In the following we will analyse selected systems with a full three-dimensional finite-difference time-domain (FDTD) approach. We will focus on the interaction of crystal modes and the modes associated with the surrounding material in systems with a high refractive index contrast between crystal and surrounding layers. We start with systems that have a simple vertical structure and will step by step advance to structures typically used in experiment.

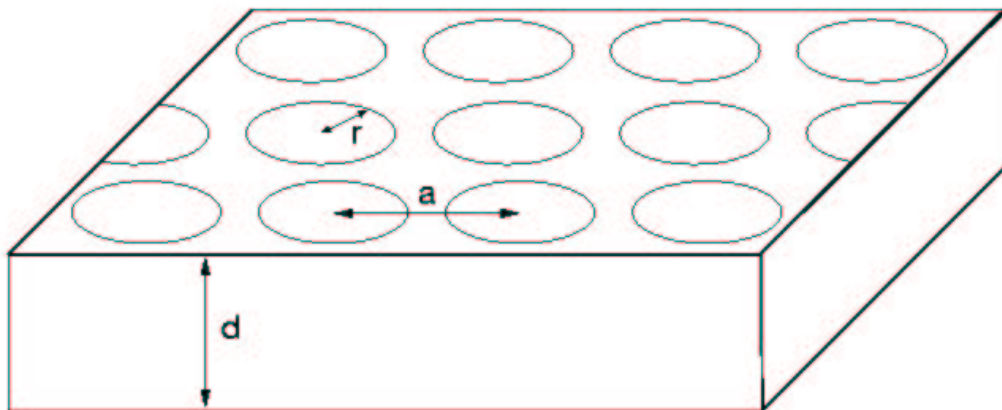


Figure 4.1: Schematic illustration of an air-bridge structure with slab thickness d , lattice constant a and hole radius r .

4.2 Principles of Slab Waveguides

4.2.1 Slab Modes and Lightcone

Before we start to analyse photonic crystal slabs we recall some well known facts about planar waveguides that are based on total internal reflection. We therefore assume a

dielectric layer with refractive index n_2 and thickness d in z -direction that is surrounded by a lower index material n_1 . The system is assumed as infinitely extended in the x - y -plane, leading to a characteristic in-plane propagation vector \vec{k}_0 due to translational symmetry.

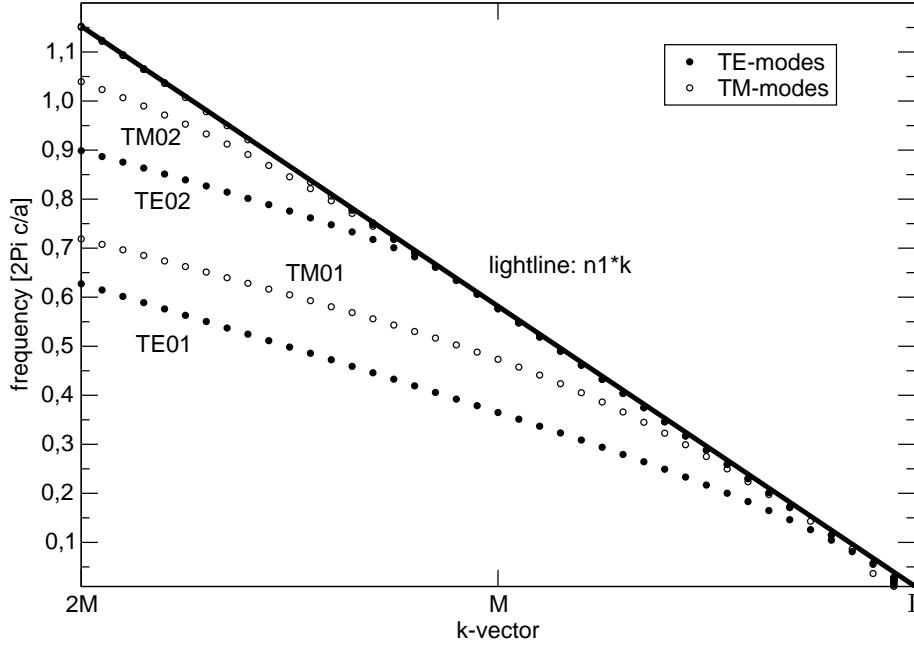


Figure 4.2: Waveguide dispersion for a slab with refractive index $n_2 = 2.17$ and thickness $d = 0.4a$ surrounded by air. The k -axis corresponds to Γ - M -direction of a hexagonal crystal with lattice constant a .

Without loss of generality we can choose \vec{k}_0 to point in y -direction. The eigenmodes of this system can now be calculated by choosing a complex exponential function in the three regions of different dielectric constant and satisfying the continuity conditions of the fields at the interfaces. This results in modes that have a cosinoidal or sinosoidal behaviour in the high dielectric region (depending on symmetry) and oscillatory or exponentially decaying behaviour in the low dielectric regions. In the latter case the energy is confined in the high dielectric core region. This can be understood as following: The mode is characterised by a wavevector \vec{k} , consisting of in-plane component \vec{k}_0 and an out-of-plane component k_z , and a frequency ω . Propagation in the low index material is only allowed if

$$\omega \leq c_0 n_1 |\vec{k}| = c_0 n_1 \sqrt{|\vec{k}_0|^2 + |\vec{k}_z|^2} \quad (4.1)$$

due to causality constraints. c_0 represents the vacuum speed of light. This implies that for $\omega > c_0 n_1 |\vec{k}_0|$, $|\vec{k}_z|$ must be real and for $\omega < c_0 n_1 |\vec{k}_0|$, $|\vec{k}_z|$ must be imaginary. In the first case the behaviour away from the core is oscillatory, in the second exponentially decaying. In an ω vs. $|\vec{k}_0|$ diagram we can therefore distinguish two regions separated by the so-called lightline (or, equivalently, lightcone) $\omega = c_0 n_1 |\vec{k}_0|$. Guided modes lie below that line while modes above the line can radiate to the surrounding layers. It should be stressed that this general statement does not tell us anything about the strength of the losses. Consequently, a mode above the lightline can have a long lifetime as well, due to e.g. symmetry considerations.

Fig. 4.2 shows the dispersion relation for the two lowest guided modes of a slab with

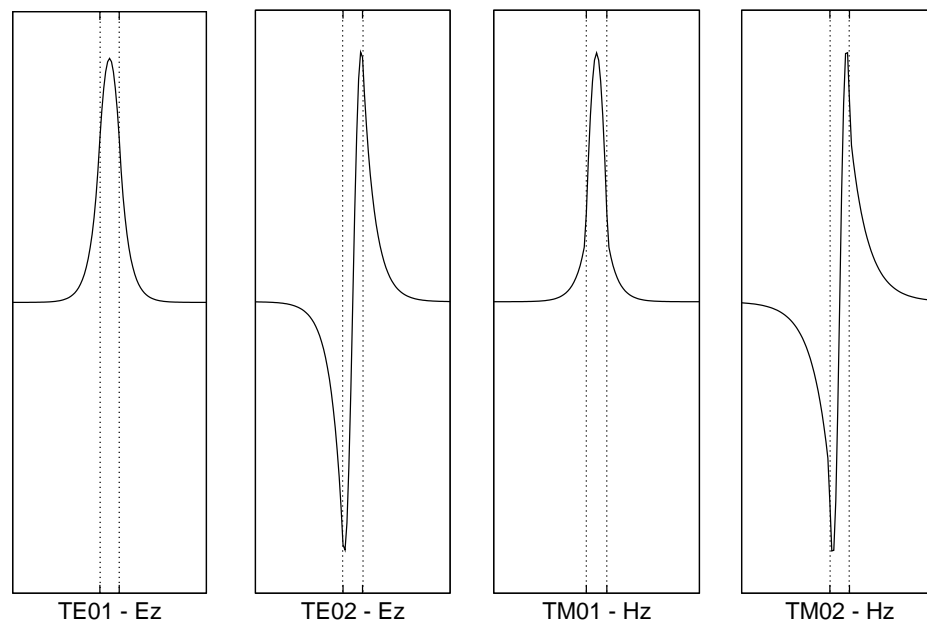


Figure 4.3: Mode profiles corresponding to fig. 4.2 at k -value $2M$. Dashed lines represent the material/air-interface.

$n = 2.17$ and $d = 0.4a$ surrounded by air for TE- and TM-polarisation, respectively. The

air-lightline $n_1 = 1.0$ is also displayed. Higher order modes are created by additional node planes in the high dielectric core as can be seen in the mode profiles in fig. 4.3. They have a certain cutoff-frequency that decreases strongly with increasing d or n_2 . If we want to avoid higher order effects, these parameters have to be chosen accordingly. The symmetry behaviour of the slab modes with respect to the mirror symmetry in x-y-plane in the center of the core region is even for the fundamental TE-mode (TE01) and odd for the fundamental TM-mode (TM01). For the higher order modes (TE02 and TM02) it is vice versa. This statement seems to be contradictory to the mode profiles in fig. 4.3 but is consistent with the definitions given in 3.1.5. The TM02 mode e.g. is even, but its only non-zero magnetic field component H_z has odd symmetry. In literature odd and even modes are often called TM-like and TE-like, respectively. It should be stressed here that this labeling is only valid for zeroth order modes.

4.2.2 Backfolding of Slab Modes

From chapter 4.2.1 we know what kind of modes a planar waveguide supports. In the following chapters we want to study step by step the way a periodic perturbation of a slab leads to a photonic crystal structure. For simplissity and easier understanding of the processes we make the following assumptions:

- Modes are TE-polarised.
- Modes are even with respect to the x-y-mirror-plane.
- We work in frequency ranges below the cutoff of higher order modes.
- The objective is a hexagonal crystal and restriction to Γ - M -direction.
- We consider only modes with odd symmetry with respect to a $(\Gamma$ - M)-z-plane.

Note that the last item may be confusing at this stage because all slab modes of the unpatterned layer have odd symmetry. However, as we will see later, in a photonic crystal structure the even symmetry is also possible but not considered because it cannot couple to an external waveguide excitation.

In the next step we artificially assume a hexagonal periodicity with lattice constant a of the translational invariant x-y-plane, to fold back the waveguide dispersion into the first BZ (Mathematically more precise we should speak of an infitesimally small periodic perturbation). For Γ - M -direction these backfolded bands are shown in fig. 4.4.

We will now have a closer look which of these bands are caused by which reciprocal lattice vector. Therefore, in fig. 4.5 we see the first BZ of the hexagonal lattice with the reciprocal lattice vectors G_i ($i = 1..6$) and the Γ - M -direction under consideration. G_i are the six lattice vectors with the smallest absolute value, so they should be responsible for the lowest bands. The k -vector at M is called k_0 . At the Γ -point for $k=0$ the first band

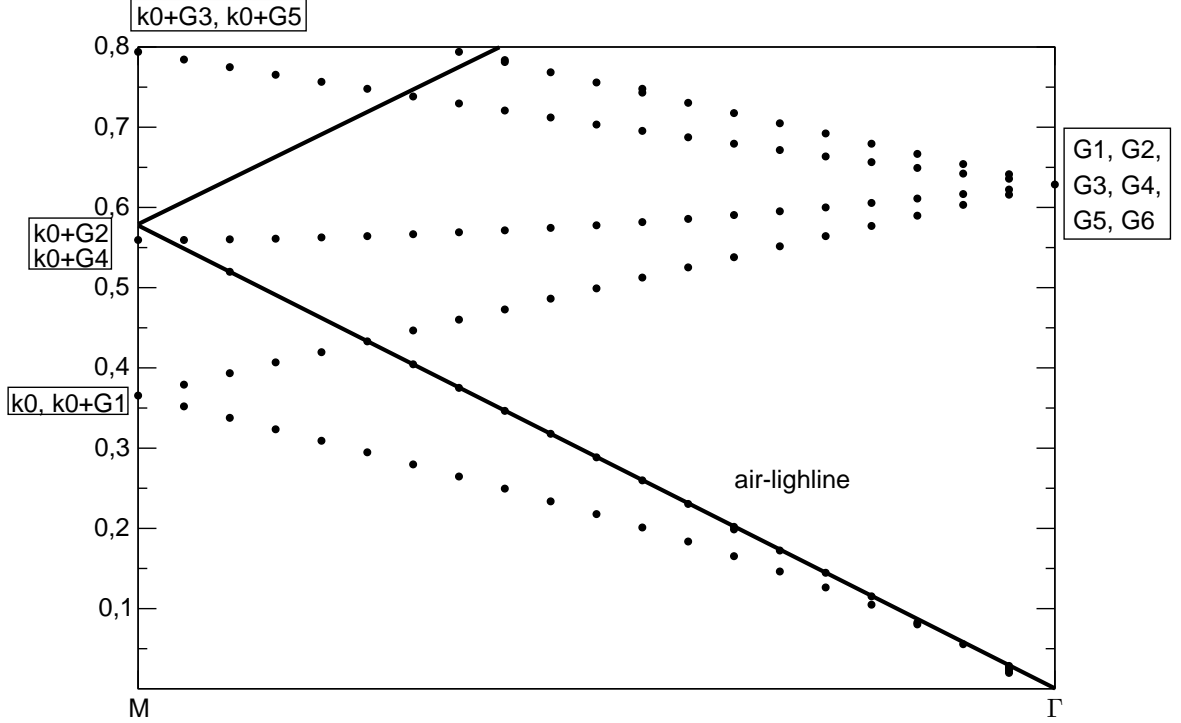


Figure 4.4: Fundamental TE-mode of an air-bridge slab; artificially backfolded into the first BZ of a hexagonal lattice in $\Gamma - M$ -direction.

has obviously zero frequency. The next higher frequency at Γ corresponds to one of all six G_i vectors that are degenerate for $k = 0$. If we increase the k -value towards M this degeneracy is partially lifted. We see a splitting into four branches. The lowest branch meets the k_0 branch of the origin at M . It must therefore be caused by adding G_1 which is directed oppositely to k_0 , leading to a two fold degeneracy at M (The lifting of this degeneracy will later cause the formation of the bandgap) because k_0 and $k_0 + G_1$ have the same absolute value.

The second and the third branch are caused by G_2 and G_3 which are equivalent to G_6 and G_5 , respectively, due to the mirror symmetry along the Γ - M - z -plane and therefore two-fold degenerate. The fourth branch represents the path from G_4 to $k_0 + G_4$ and is not degenerate.

Due to the backfolding the bands have crossings with each other or with the lightline. As the periodicity is artificial up to now there is no interaction at this crossing, although it would be allowed by mode symmetry. The introduction of real periodic variations will cause this mode interaction. From the picture described in this chapter it is obvious

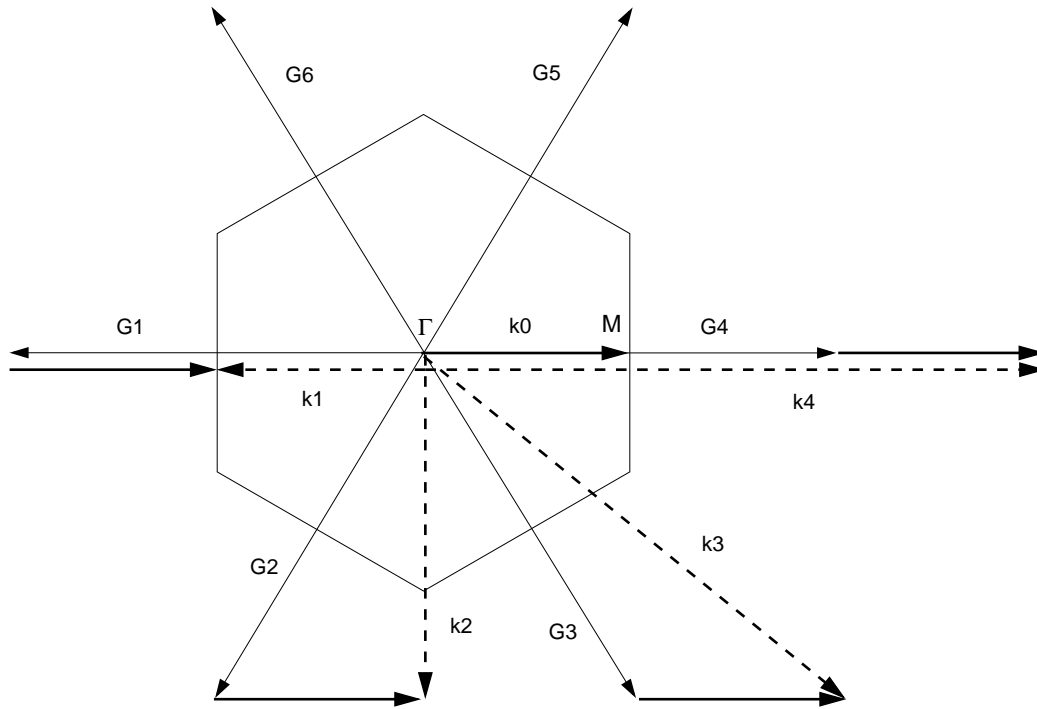


Figure 4.5: Schematic illustration of the backfolding process along $\Gamma - M$ -direction.

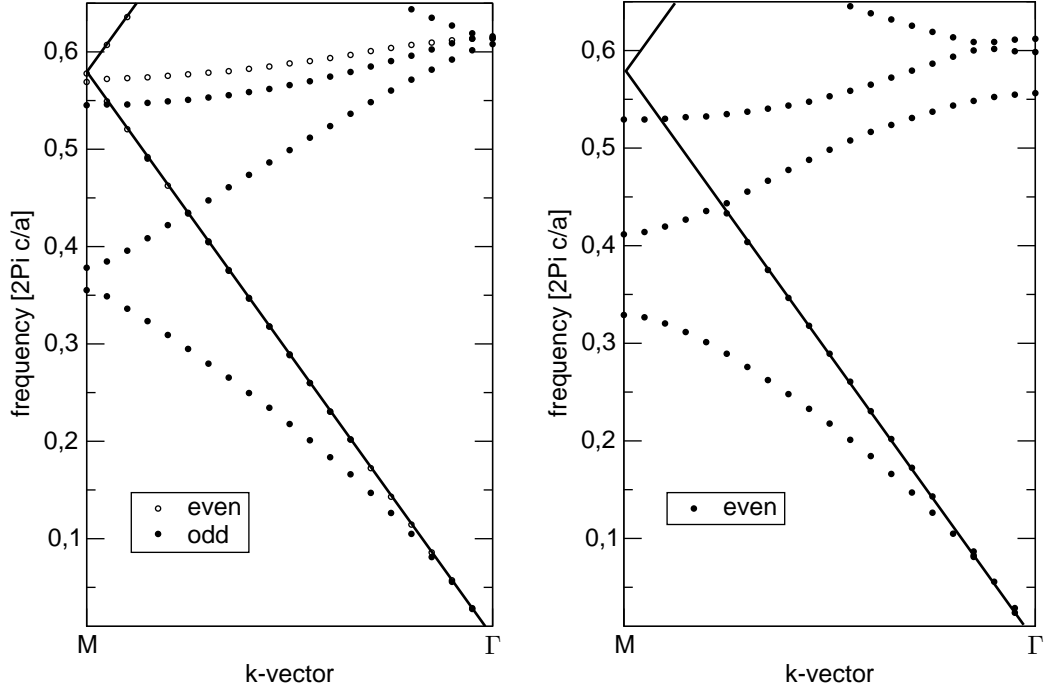
that this interaction is caused by Bragg scattering at the periodic structure and therefore a consequence of the introduction of real plane-wave-components with wavevectors $k_0 + G_i$.

4.3 Interaction of In-Plane Periodicity and Vertical Structure.

4.3.1 Air-Bridge Structure

We will now investigate the gradual transition of the backfolded modes of an unpatterned dielectric slab surrounded by air as described in 4.2.2 to a hexagonal photonic crystal consisting of air holes with radius r .

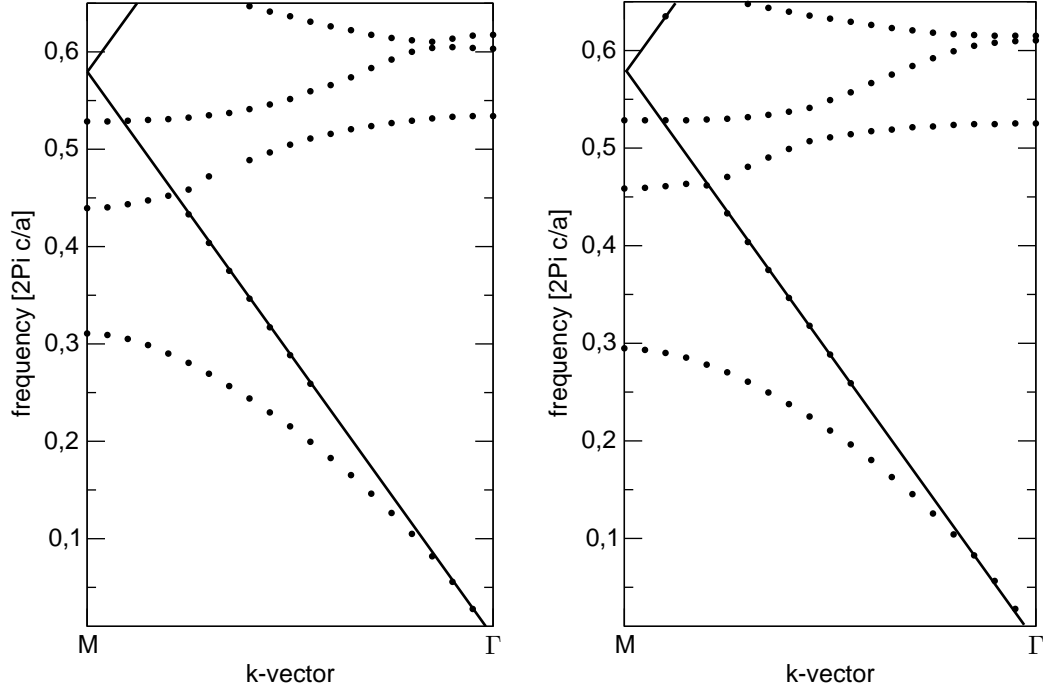
For a better comparability of the structures for increasing hole radius r we keep the geometrically averaged refractive index n_{avg} , given by


 Figure 4.6: Left: $r = 0.133a$, $n_2 = 2.25$ Right: $r = 0.266a$, $n_2 = 2.58$

$$n_{avg} = \frac{(\sqrt{3}a^2 - 2\pi r^2)n_2 + 2\pi r^2 n_h}{\sqrt{3}a^2} \quad (4.2)$$

of the slab constant, where n_2 is the refractive index of the slab and n_h the refractive index within the holes. As r and $n_r = 1.0$ are given, the adjustable parameter to keep n_{avg} constant is n_2 .

We start with a radius $r = 0.133a$ and a corresponding $n_2 = 2.25$. Fig. 4.6 (left) shows the Γ - M bandstructure of the system. We can see the following effects: The two-fold degeneracy of the first and second band at M is lifted and a small bandgap appears. The corresponding spatial distributions of the electric energy (fig. 4.8 and fig. 4.11) show that the original plane waves in the x-y-plane are only slightly disturbed by the hole. However, while in the unperturbed slab the in-plane phase of the waveguide modes was arbitrary, now the superposition of two counterpropagating waves form either a standing wave with a minimum or a maximum in a hole, respectively. This causes different energies and therefore the frequency splitting that leads to a gap. This mechanism is qualitatively


 Figure 4.7: Left: $r = 0.333a$, $n_2 = 2.96$ Right: $r = 0.375a$, $n_2 = 3.40$

the same as the one in the ideal two dimensional system. The difference is that the basis for these considerations are now eigenmodes of the unperturbed slab instead of plane waves.

We also want to investigate the next branch of the slab, caused by the counterpropagating G_2 and G_6 waves of the unperturbed slab, which is two-fold degenerate. These two G -vectors correspond at the M -point to modes with a k -vector pointing perpendicular to the selected Γ - M -direction. As expected the branch also splits into two when introducing a periodic modulation by a similar mechanism as for the band gap. The difference is now that because the original slab modes propagate perpendicular to the Γ - M -direction the two possibilities of adjusting the phase of the counterpropagating parts result in an even and an odd mode with respect to the $(\Gamma$ - M)- z mirror plane. This can be seen in the bandstructure in fig. 4.6 (left) and the energy distribution in fig. 4.14 and fig 4.17. As we want to restrict ourselves here to modes that can couple to fundamental excitations in Γ - M -direction (that are always odd), we will from now on neglect the

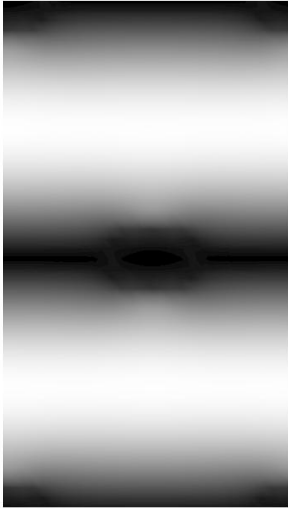


Figure 4.8: 1st TE at M,
 $r = 0.133a$.

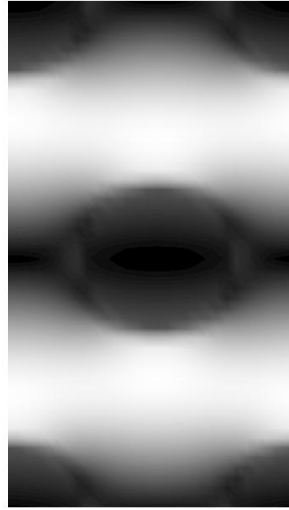


Figure 4.9: 1st TE at M,
 $r = 0.266a$.

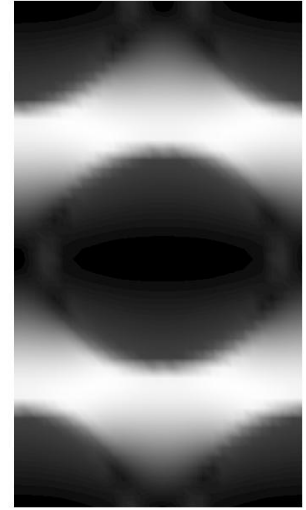


Figure 4.10: 1st TE at M,
 $r = 0.375a$.

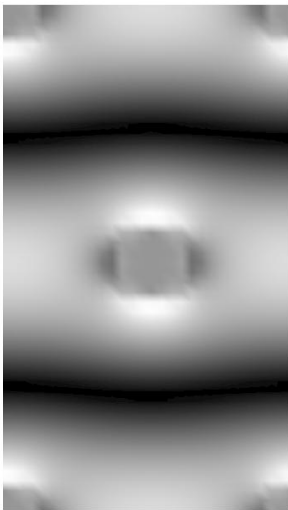


Figure 4.11: 2nd TE at M,
 $r = 0.133a$.

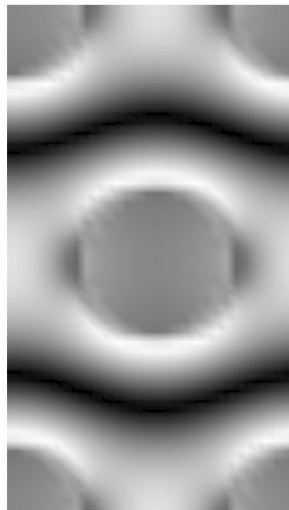


Figure 4.12: 2nd TE at M,
 $r = 0.266a$.

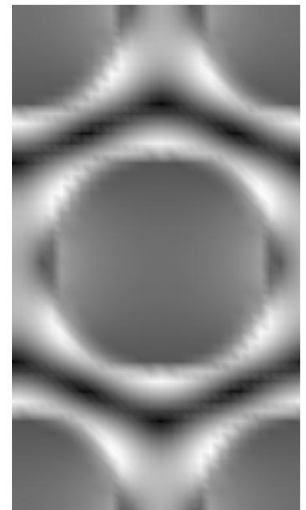


Figure 4.13: 2nd TE at M,
 $r = 0.375a$.

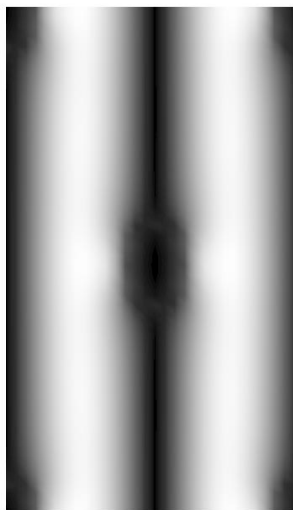


Figure 4.14: 3rd TE at M,
 $r = 0.133a$.

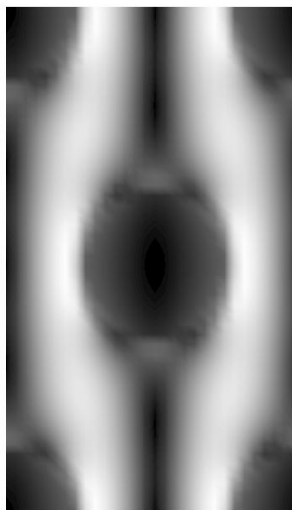


Figure 4.15: 3rd TE at M,
 $r = 0.266a$.

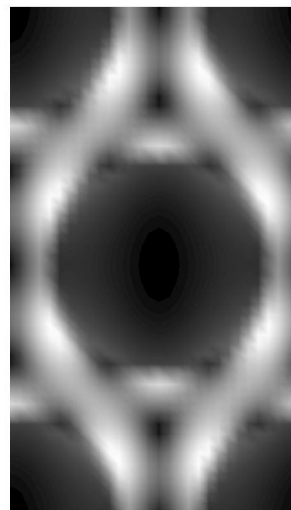


Figure 4.16: 3rd TE at M,
 $r = 0.375a$.

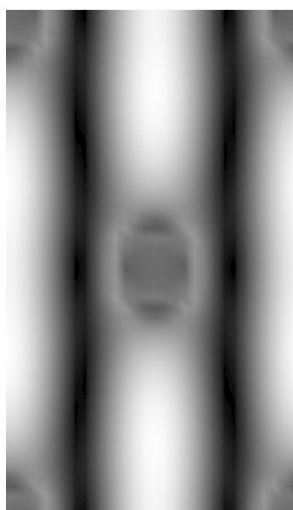


Figure 4.17: 4th TE at M,
 $r = 0.133a$.

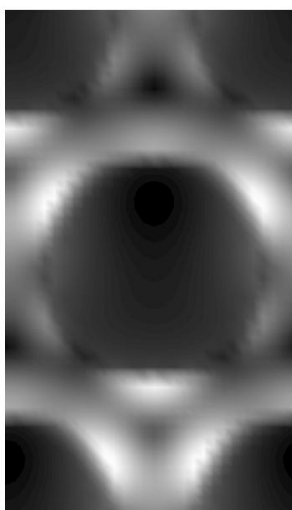


Figure 4.18: 2nd TE at
interaction
point.



Figure 4.19: 3rd TE at
interaction
point.

even band. Higher branches of the backfolded bands of the unperturbed slab modes behave in similar ways. We refrain from discussing them in detail now because for most applications we are only interested in the few bands limiting the bandgap.

Now we increase the radius of the holes as well as the refractive index of the background to keep the effective index constant and calculate bandstructures and energy distributions for $(r = 0.266a, n_2 = 2.58)$, $(r = 0.333a, n_2 = 2.96)$ and $(r = 0.375a, n_2 = 3.4)$. The last set of parameters corresponds to silicon which is typically used in experiment for high contrast applications and represents the material class that we will study further in this work. Fig. 4.6 (left) to 4.7 (right) show the gradual development of the bandstructures while fig. 4.8 to fig. 4.16 show the corresponding energy distributions at the M -point for the three lowest odd bands. With increasing index contrast the bandgap becomes larger and has approximately a constant center frequency because of the constant effective index. The third band is effected least by this procedure. We can also see that for higher index contrast the energy distributions are more and more distorted compared with the nearly plane wave low perturbation case.

Since up to now the discussion was not qualitatively different from the two dimensional case, we will now have a closer look at properties that are unique to slab structures. We have argued before that backfolded modes with matching symmetry should couple, resulting in an avoided crossing and mixing of the field distributions around the crossing. This should also be valid for the crossing of photonic crystal slab modes with the lightline that represents the modes allowed in the surrounding layers. Unfortunately, in the bandstructure the resolution in k - and ω -space that is achievable with our FDTD-algorithm is too small to identify the avoided crossing. However, especially for the second band and higher index contrast we can see a distortion of the band when crossing the light line (fig. 4.7 (right)). As an interaction with modes of the environment continuum above the lightline would make the slab modes lossy, we will now study the loss behaviour for the second and the third band. Therefore we define the losses of an eigenmode

$$\vec{E}_k^\omega(\vec{r}, t) = e^{i\omega t} \vec{E}_k^\omega(\vec{r}) = e^{i Re(\omega)t - Im(\omega)t} \vec{E}_k^\omega(\vec{r}) \quad (4.3)$$

as the imaginary part $Im(\omega)$ of the (now complex) frequency ω . This exponential decay in time corresponds to a Lorentzian lineshape in frequency with a linewidth related to $Im(\omega)$. For practical calculations we can either analyse the linewidths of the FDTD-spectra in frequency domain or the decay behaviour in time after a monochromatic excitation (see 6.3.1). For most examples in this chapter we use the latter, but in this section we also show spectra for illustration. Qualitatively, it should be a reasonable assumption that structures with larger holes should have higher losses because there is no guiding by total internal reflection above the holes. To see this we calculate the relative linewidths of modes for $k = 0.7\pi/a$ in Γ - M -direction for the four systems with constant n_{avg} and varying radius described above. The modes corresponding to this k -value lie just above the lightcone. Fig. 4.20 shows the normalised Lorentzian lines. The

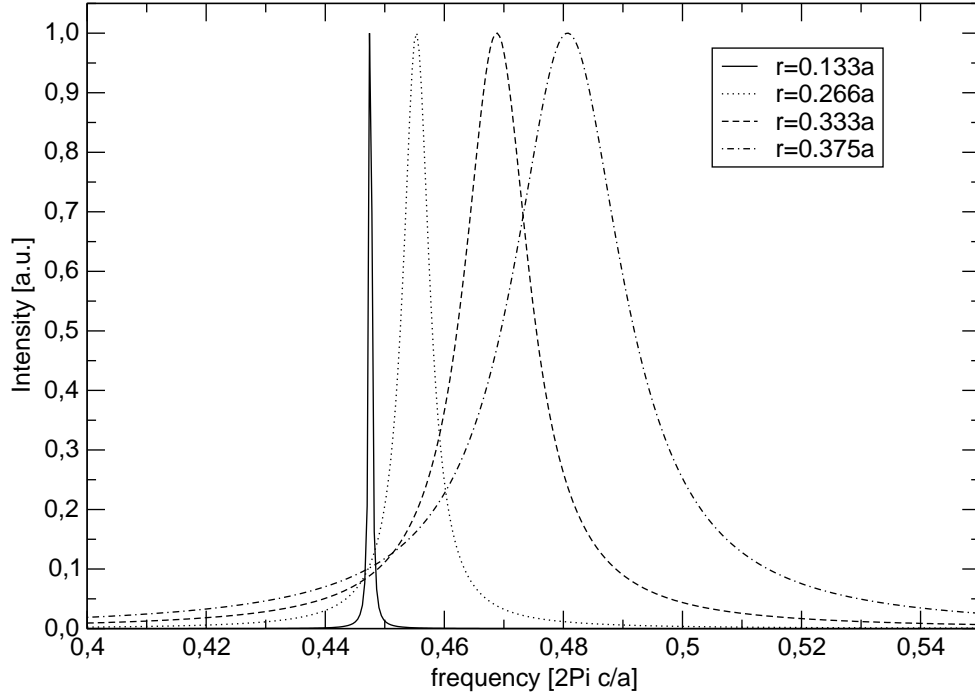


Figure 4.20: Spectral lineshape in dependence of hole size above the lightcone (2^{nd} TE-band).

strong increase of the linewidth with hole radius is clearly visible. From the smallest to the largest holes investigated here we have approximately a factor of 20. If the hole size is a determining parameter of the losses it should also make a difference how much energy is localised within the holes. Therefore a comparison of the second band (energy localised mainly in the holes) and the third band (energy localised mainly in the high dielectric) region would be desirable. Unfortunately this is difficult because as can be seen in the bandstructure fig. 4.7 (right) these bands interact in an avoided crossing and mix field profiles there. This can be seen in fig. 4.18 and 4.19 where the electric energy is shown for both bands close to the interaction point. Nevertheless, we calculate $Im(\omega)$ for the second and third band of the silicon crystal. The result, as can be seen in fig. 4.21 (left), shows that there are vanishing losses for modes below the lightline as expected theoretically. Above the lightline $Im(\omega)$ strongly increases for the second band and drops when approaching the interaction point with the third band. The third band shows a complementary behaviour, reaching its maximum value behind the anticrossing.

This behaviour supports our assumption that the large losses occur for modes with high intensity within the holes, because the air band dominates the field distribution of the second band left of the anticrossing and the third band right of the anticrossing. Close to the Γ -point the losses for both bands tend to zero. This effect can be explained by symmetry considerations. For a detailed discussion see [27].

After we clarified the most important physical mechanisms that are responsible for the band structure and the loss behaviour of an air-bridge structure, we now want to discuss in more detail the technologically relevant quantities, band gap and losses, for the silicon-based structure. From an application point of view it is desirable to have a large band gap which means a big operating window for devices based on defects (cavities, waveguides). On the other hand we need low losses because optical signals should propagate over some distance without the need of amplification. From our discussion so far we know that these conditions cannot be fulfilled simultaneously because we need large holes for an optimum band gap and small holes for minimum losses. We will now study the dependance of these quantities in the silicon structure on hole size to clarify which process is dominating. We address this problem from three directions: the bandstructure, $Im(\omega)$ of the lossy second and third band and finally by propagation simulations through a finite number of hole layers. The latter has the following reason: $Im(\omega)$ only describes the temporal losses while in applications often the losses per propagation length are relevant. These two quantities are related by the group velocity of the mode. As the group velocity is difficult to calculate by time-domain methods due to the need of a very high accuracy in frequency, we choose another approach for estimating the propagation losses. We calculate the transmission through finite samples of different lengths. The difficulty of this method is that we have a superposition with Fabry-Perot-resonances in the transmission spectrum that are due to the finite length of the sample. Moreover, there are also coupling losses when the exciting pulse enters the photonic crystal. Although these difficulties allow us only to give an estimation of the propagation losses, the results are very important because they are directly comparable with experiments in contrast to calculations that are based on infinitely extended structures. Fig. 4.21 compares bandstructure, losses and transmission through 21 and 41 rows of holes, respectively, for the silicon system with $r = 0.375a$. In the transmission calculations we only see two narrow transmission peaks for frequencies corresponding to the second band below the lightline ($\omega \approx 0.46$) and close to the Γ -point ($\omega \approx 0.52$). The second peak does not correspond to the third band at M which also seems possible from the band structure, but to the second band at Γ , because the part of the third band lying below the lightcone is very flat (low group velocity) and cannot couple properly to the excitation due to impedance mismatch. These results match well with the corresponding $Im(\omega)$ values. The bandgap can be clearly identified in the transmission calculations as well as the transmission close to one for the first band that is located entirely below the lightline. Now we reduce the hole radius to $r = 0.333a$ and show the corresponding results in fig 4.22. As expected, the bandgap decreases as well as

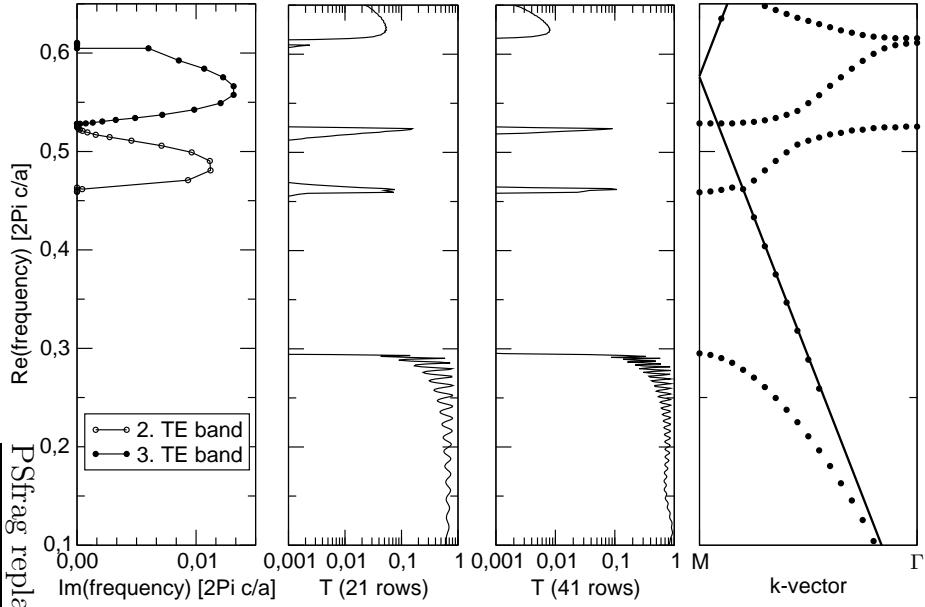


Figure 4.21: Losses, transmission results and bandstructure for $r = 0.375$.

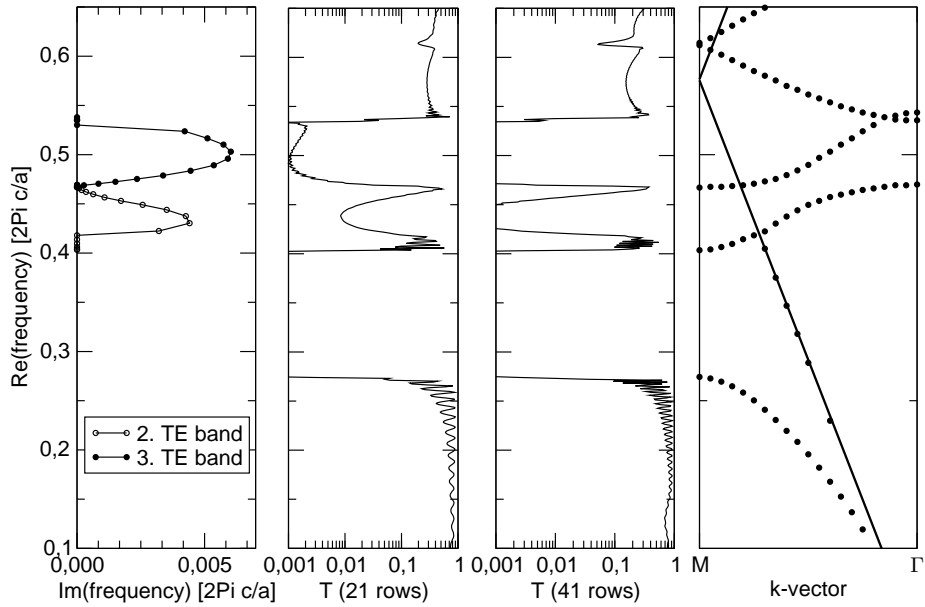


Figure 4.22: Losses, transmission results and bandstructure for $r = 0.333$.

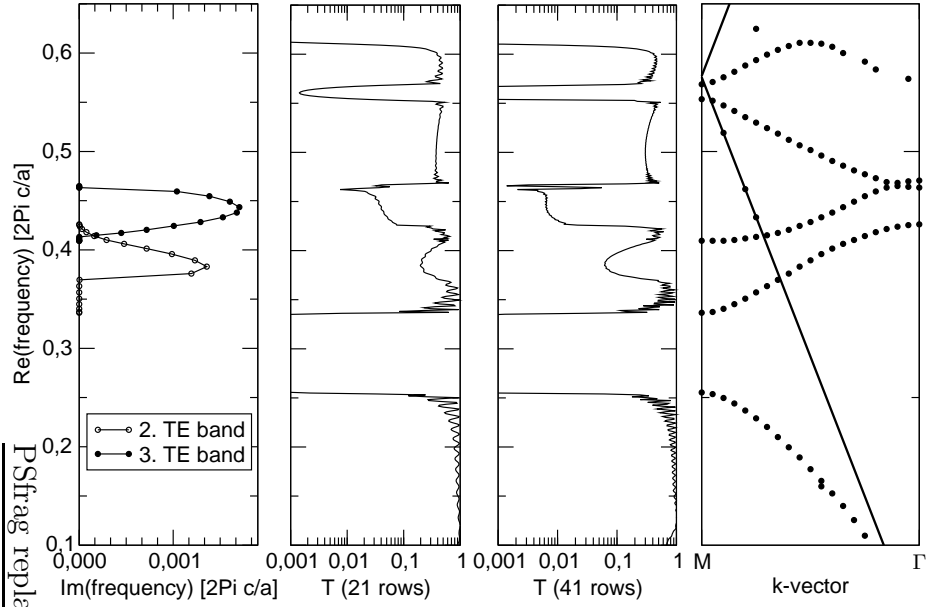


Figure 4.23: Losses, transmission results and bandstructure for $r = 0.266$.

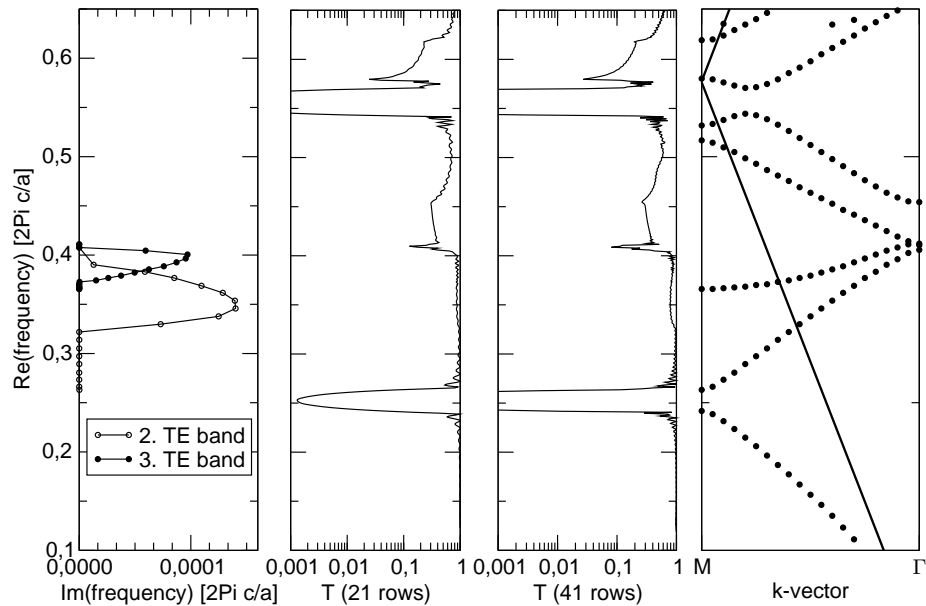


Figure 4.24: Losses, transmission results and bandstructure for $r = 0.133$.

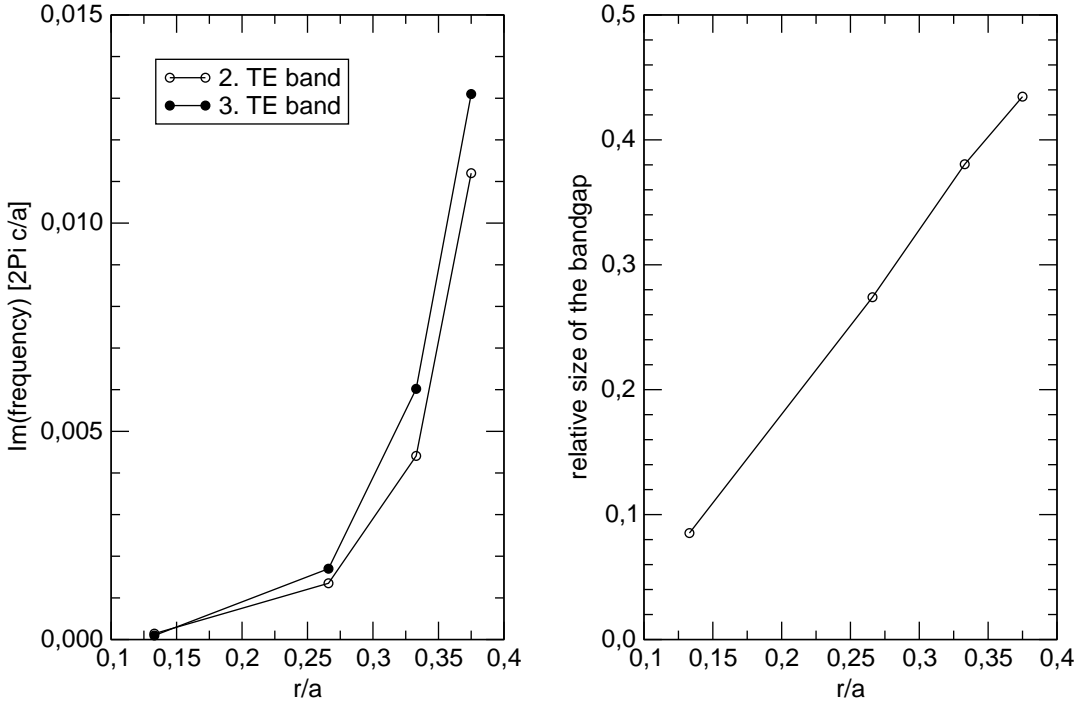


Figure 4.25: Left: Maximum losses of second and third TE-band for varying hole radius r . Right: Relative gap width for varying hole radius r .

the losses, leading to observable transmission of the second band in the order of 1% at least for 21 rows. Also the absolute height of the transmission peaks at Γ and below the lightcone increases strongly. This is not due to lower losses but to better coupling for two reasons. First, the bands are generally slightly steeper for smaller radius, leading to a smaller impedance mismatch. Second, the (allover) effective index difference between the photonic crystal and the incoupling waveguide is smaller, also leading to a smaller impedance change at the interface.

We further decrease the hole size to $r = 0.266a$ and $r = 0.133a$ and see the tendencies described above confirmed. The corresponding results are shown in fig. 4.23 and fig. 4.24. We now want to compare the decrease of the bandgap with the decrease of losses for smaller holes quantitatively. Fig. 4.25 compares the relative width of the bandgap ($\Delta\omega/\omega_c$) with the maximum value of $Im(\omega)$ along the second and the third band for the described systems. While the size of the bandgap increases nearly linearly with the hole size, the losses have a much stronger dependence of the radius. The message for technical applications is clear: The price (in terms of losses) one has to pay

for an optimum bandgap is very high. It should be carefully balanced how large the bandgap really has to be to keep losses small.

4.3.2 Infinite Low-Index Cladding

The structures described in the preceding section (often referred to as membrane or air-bridge structures) have some intrinsic disadvantages from an experimental point of view. They are difficult to fabricate because after a standard lithography process the substrate below the guiding layer has to be removed. Moreover, the resulting structures are sensitive to mechanical perturbations and therefore not useful for many applications. A possible solution of these problems is to embed the guiding layer in a material with lower index instead of air. Consequently, our next step toward a realistic and more applicable photonic crystal slab is to consider a high index guiding layer, surrounded by a low index cladding of infinite thickness. This cladding can either be structured like the guiding layer or can consist of homogeneous material. We will focus here on the first case, because in the second the physical principles are not different from the air-bridge case with the exception that the air-lightline is replaced by the linear dispersion of the cladding material. Another reason is that in fabrication it is much more convenient to entirely pattern a layer-by-layer system instead of surrounding an air-bridge structure with another material.

This type of system can be seen as a high index photonic crystal slab surrounded by two semi-infinite two-dimensional photonic crystals. It has been pointed out in [28] that total internal reflection is now described by the lowest band of the two-dimensional crystal cladding. Therefore, to distinguish regions of guided and lossy modes, we have to supplement the three dimensional slab-bandstructures by the corresponding two-dimensional calculations. As we are dealing with mirror symmetric (with respect to the mirror plane in the center of the guiding layer) structures this can be done for different polarisations separately.

Fig. 4.26 (left) shows the bandstructure of a silicon slab with an infinite cladding of SiO_2 with refractive index $n_{clad} = 1.45$ (solid circles), including the corresponding 2D-bands of the SiO_2 -crystal (hollow circles). We can see that only the first slab band is guided but nearly the entire bandgap lies below the lightline. We can therefore expect losses in applications relying on refractive properties of higher bands. However, there is a good chance of defect bands lying at least partially below the lightline. This is discussed for W1-waveguides in [20]. It is obvious that with increasing effective refractive index of the cladding the slope of the lightline will decrease and therefore less frequency ranges are guided by total internal reflection and therefore a small cladding index is desirable. However, there exists a counteracting mechanism that makes the ideal material choice more sophisticated.

The strength of the spatial localisation to the guiding layer is proportional to the difference in the refractive index between core and cladding. Therefore, for a low index cladding we have a very strong confinement to the guiding core layer. However, a

strong spatial localisation means a weak localisation in k-space and consequently strong out-of-plane plane-wave-components. This is not relevant if there is total internal reflection. However, if coupling to the cladding-modes is allowed in principle (in regions above the lightline), this should lead to larger losses. We will analyse this now quantitatively by increasing the cladding index, while keeping all other parameters constant. Fig. 4.26 (right) shows the bandstructure for $n_{clad} = 2.0$. As expected, there is only a slight decrease of the frequencies in the bandstructure due to a slight increase of the effective index of the crystal modes.

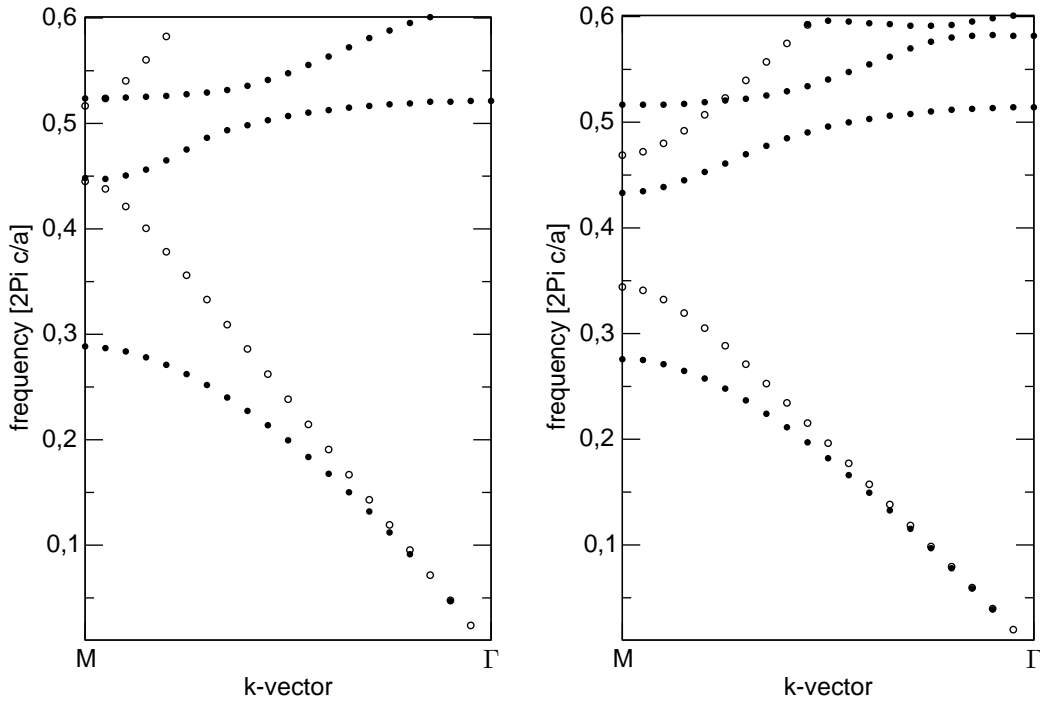


Figure 4.26: Bandstructure for a slab with $n_{core} = 3.4$, core thickness $d = 0.4a$, hole radius $r = 0.375a$ and infinitely extended cladding with refractive index $n_{clad} = 1.45$ (left) and $n_{clad} = 2.0$ (right).

However, the lightline lies significantly lower, indicating a smaller operating window for guided modes. Consequently we now also compare the losses of the second band that is above the lightline for both cases.

Fig. 4.27 shows $Im(\omega)$ for the described systems and also for $n_{clad} = 2.5$ along the Γ - M -path. We can see a very strong dependance of the losses on the cladding index.

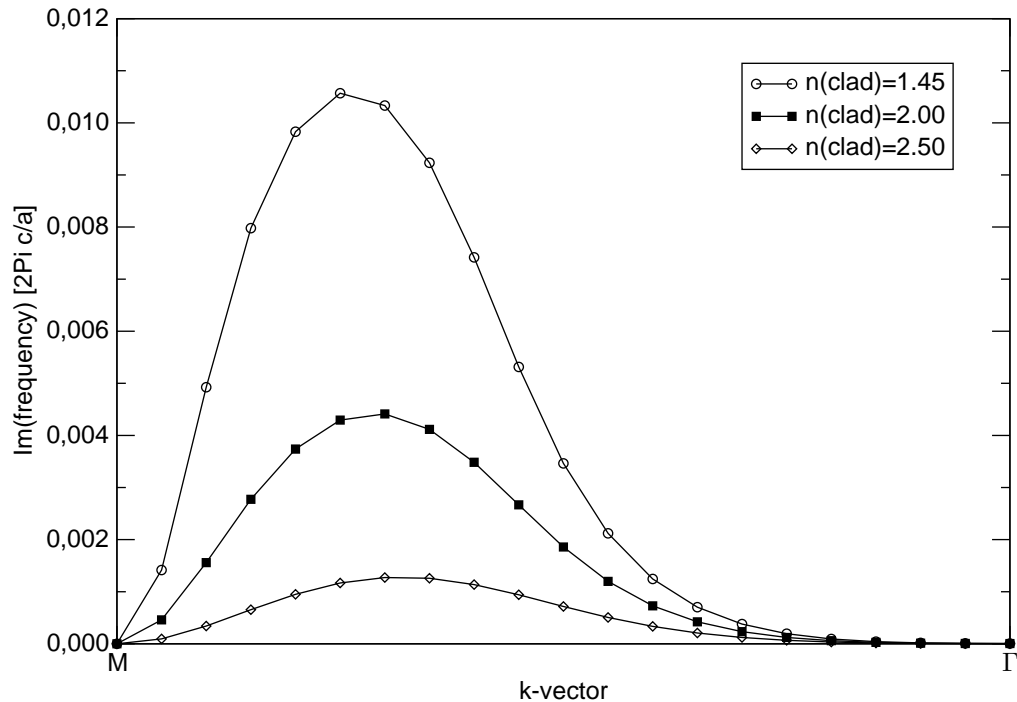


Figure 4.27: $Im(\omega)$ for the second TE-band of a slab with $n_{core} = 3.4$, core thickness $d = 0.4a$, hole radius $r = 0.375a$ and infinitely extended cladding with varying refractive index n_{clad} .

Additionally, the localisation and the corresponding k-space distribution does not only influence intrinsic losses of the perfect system but also causes a higher tolerance of low index-contrast structures against fabrication tolerances, especially surface roughness and hole shape [25].

This fundamental property of photonic crystal slabs has caused the development of two oppositely directed streams within the photonic crystal community. On one side there are groups that investigate high-index-contrast structures mainly based on silicon and silicon-oxid layers, relying entirely on the intrinsically lossless guided parts below the lightline, because the high losses above make these frequency regions unusable [29]. On the other hand there is the philosophy of using low-index-contrast structures, mainly based on III-V semiconductors like GaAs or InP, which have intrinsic low losses but have much higher tolerance against practical imperfectness, but also an additional need of deeper holes because of the the weaker localisation. In future investigations it has to be demonstrated, which ansatz is more successful with respect to technological applications.

4.3.3 Finite Low-Index Cladding

Consequently, the next step towards a realistic description of a a photonic crystal slab is to assign a finite thickness d to the cladding layers. An illustration of the systems under consideration in this section can be seen in fig. 4.28.

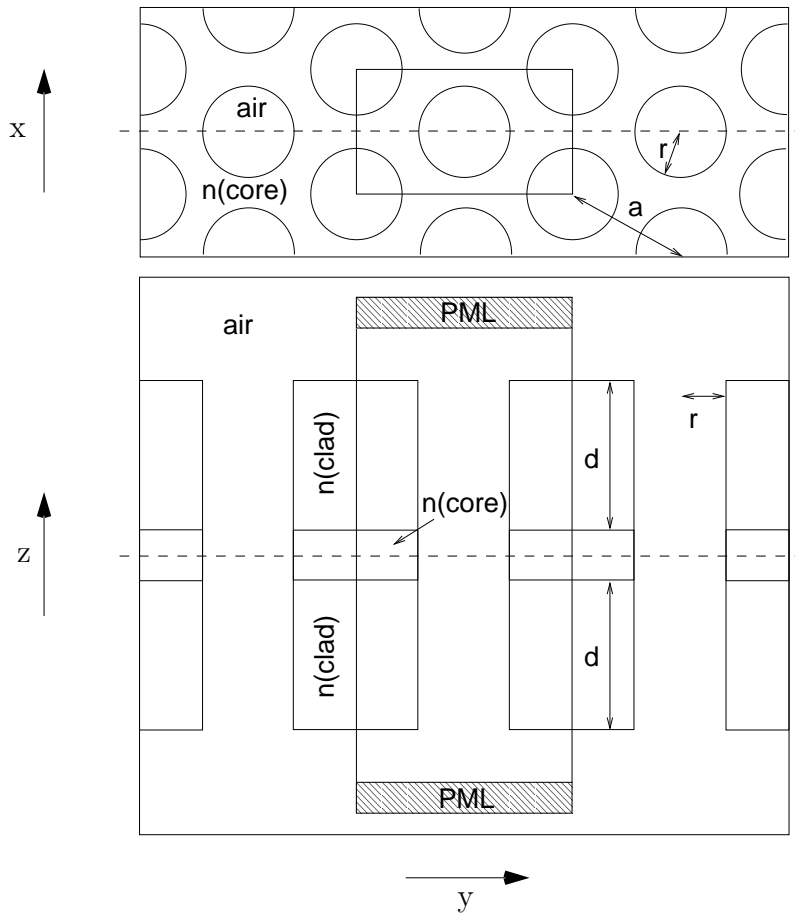


Figure 4.28: Schematic cross-sections of the symmetric finite cladding structure with hole radius r , cladding thickness d and lattice constant a . The insets show the numerical unit cell. All boundaries with exception of the marked PML's are periodic. For more details see text.

The insets show the cross-sections of the unit cell used in the FDTD-calculations, while the dashed lines show the position of the opposing cross-section. Intensity profiles that will be discussed in this section always correspond to these insets. Moreover, we restrict ourselves to a Si/SiO_2 -system with $n(\text{core}) = 3.4$ and $n(\text{clad}) = 1.45$, respectively. The core thickness is $0.4a$.

Before we analyse particular systems we will discuss the principal physical effects associated with the finite cladding thickness. First, we expect that the modes which are confined to the core and decay exponentially into the cladding exist in a similar way as in 4.3.2 and are quantitatively the same for a sufficiently large d . Second, we would also expect modes which are confined to the hole three-layer-structure (because it has a higher refractive index than the surrounding air) that decay exponentially into the air region but not within the cladding. These modes are guided when they are lying below the air-light-line while for the core modes a definition for a lightline is not obvious.

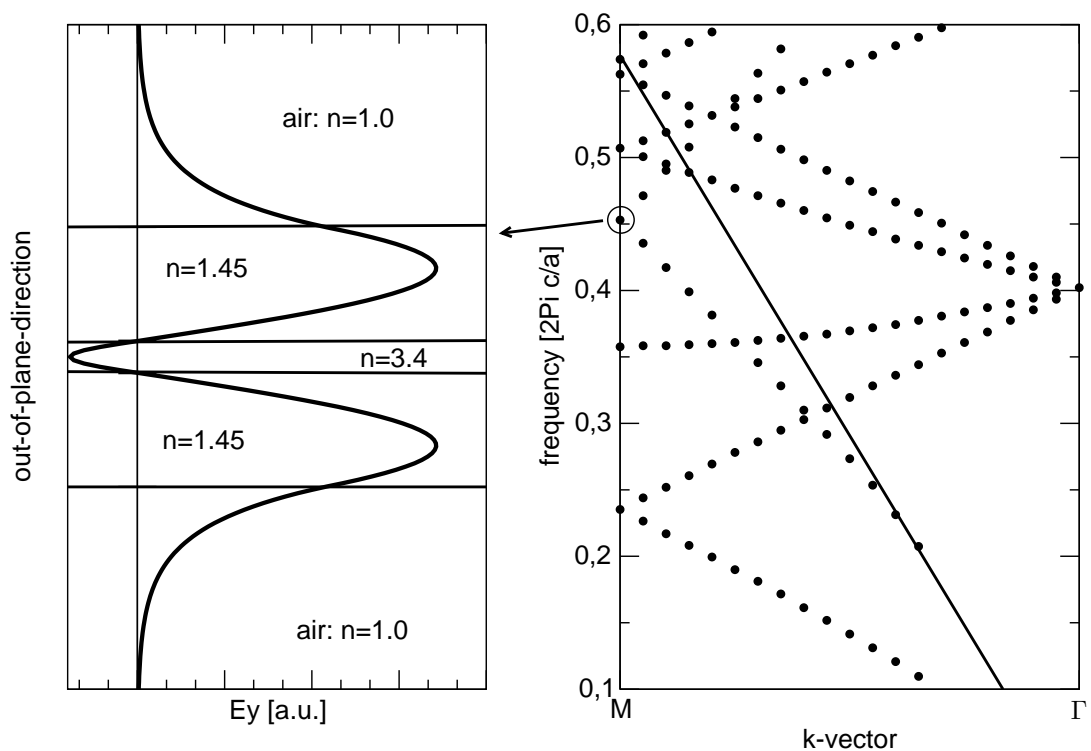


Figure 4.29: Left: Mode profile of the cladding mode at M . The insets correspond to dielectric interfaces in the three-layer-system. Right: Artificially backfolded dispersion of the three-layer-system with $d = 1.2a$.

Third, when these two types of modes - from now on referred to as core- and cladding-modes - have crossings in the dispersion relation they should in principal be able to interact, resulting in an avoided crossing behaviour and modes with mixed spatial characteristics.

To address these suggestions quantitatively we first analyse the artificially backfolded

banddiagram of an unpatterned slab structure with $d = 1.2a$. The result in fig. 4.29 (right) shows a very similar picture as for the air-bridge structure discussed in 4.3.1. However, we can clearly identify an additional band that comes up close to the lightline with a higher frequency than the fundamental core mode. We calculate the spatial profile of this band at the M -point and see in fig. 4.29 (left) that this mode, indeed, satisfies the definition of a cladding mode. Moreover, we can see that it has also some significant field strength in the core, which means it is able to couple to core-modes. The band diagram also suggests two crossings of the lowest branch of the cladding modes with two backfolded core modes.

In the next step we pattern the three-layer-structure with small holes with $r = 0.2a$. The bandstructure in fig. 4.30 (right) shows the already discussed splitting of the core modes as well as for the cladding modes, while the interaction of cladding and core bands is difficult to determine due to a low resolution in k -space.

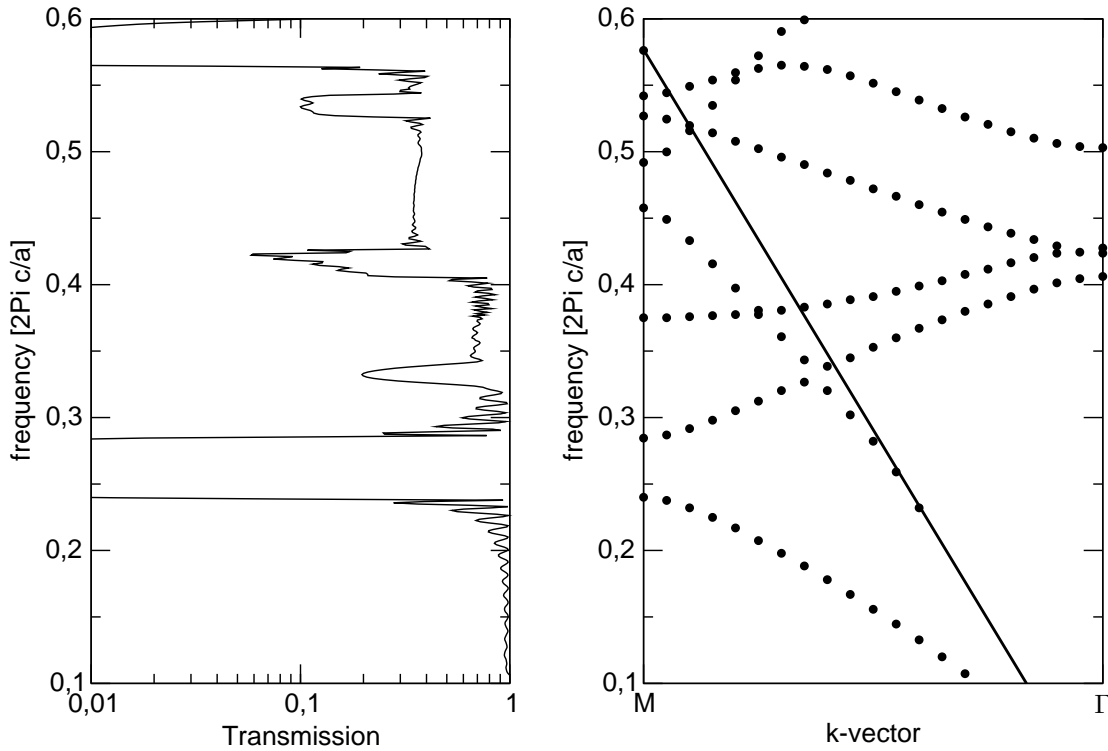


Figure 4.30: Left: Transmission through 21 rows. Right: Bandstructure for $r = 0.2a$ and $d = 1.2a$.

Instead of increasing the k -space resolution we perform a transmission simulation of

a finite sample of 21 crystal rows in Γ - M -direction (fig. 4.30 (left)). Here we can clearly identify a transmission dip corresponding to the frequency of the crossing between the second core- and the cladding-band which indicates an avoided crossing. The interaction between the third core- and the cladding-band is weaker and does not leave its "foot-print" in transmission.

To explain this behaviour we calculate the spatial distribution of the electric energy for the second and the third core band as well as the two lowest cladding modes at the M -point.

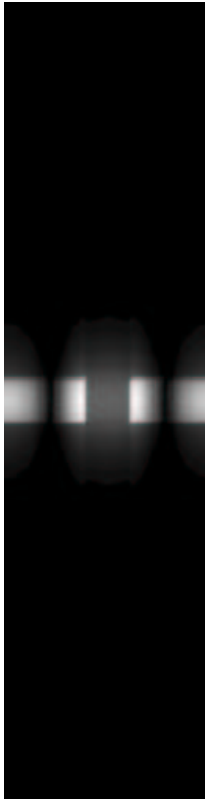


Fig. 4.31: Second core band at M .

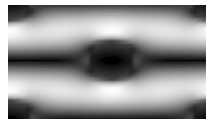
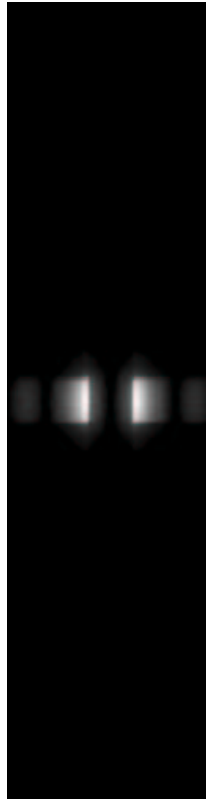


Fig. 4.32: Third core band at M .

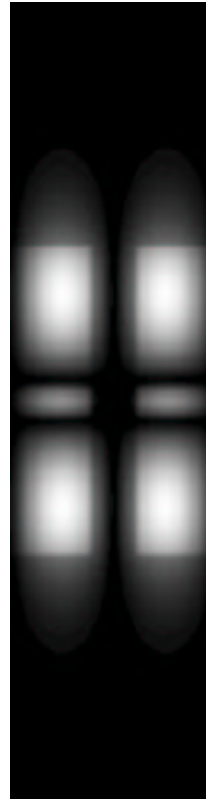
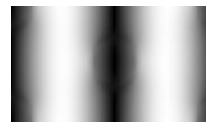


Fig. 4.33: First cladding band at M .

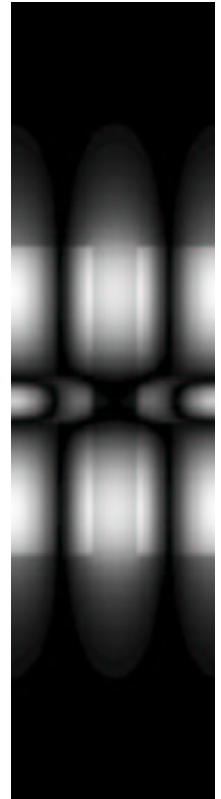
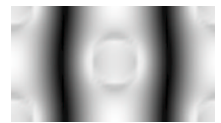


Fig. 4.34: Second cladding band at M .

In fig. 4.31 to 4.34 (and all following figures of this type) we display cross-sections along y-z-plane (in the center) and x-y-planes in the core region (top) and the cladding (bottom). The electric energies are always scaled to the maximum within the particular cross-section.

As all modes are calculated at the M -point and therefore far away from interaction points, the x-y-distributions in core and cladding do not differ qualitatively. However, it is obvious that both the second core- and the first cladding-band have dominating plane-wave components pointing in y-direction while the third core band has dominating components in x-direction. The resulting spatial overlap explains the different coupling strength at the two discussed anti-crossings.

The second cladding-band has a x-y-cross-section similar to the second core band. This is not surprising because we expect the same type of degeneracy splitting at M for the cladding bands as for the core bands.

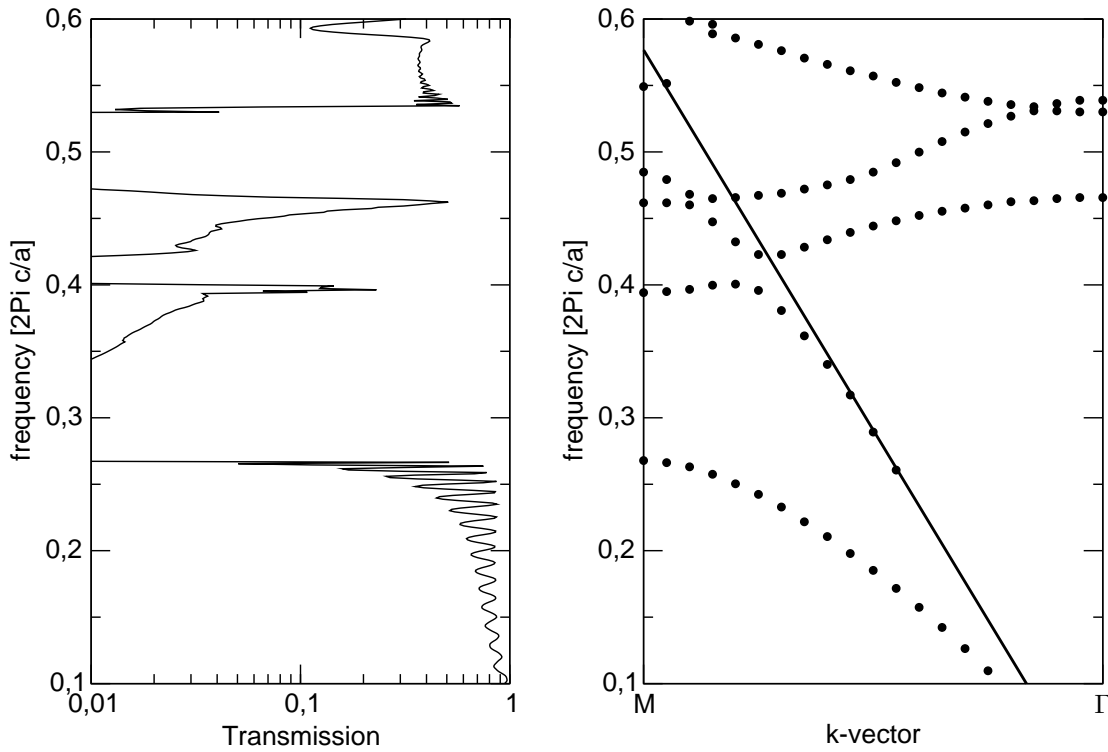


Figure 4.35: Left: Transmission through 21 rows. Right: Bandstructure for $r = 0.333a$ and $d = 1.2a$.

If we further increase the hole size to $r = 0.333a$ we see an even stronger avoided crossing behaviour that now causes a significant gap of ≈ 0.02 that is clearly visible

as well in bandstructure (fig. 4.35 (right)) and transmission (fig. 4.35 (left)) and also a small avoided crossing between the third core and the first cladding band. This can be explained by the decreasing filling fraction. The modes that mainly concentrate their energy in the high dielectric regions are forced to extend more into y-direction, with the result of a stronger interaction.

Moreover, the strong avoided crossing of the second core and the first cladding band is now quite close to the frequency of the second core band at the M -point. This has important consequences, because this frequency marks the upper edge of the bandgap of the core modes. We know that the mode profiles mix around the crossing. Consequently, there exists a branch of the cladding band that reaches into the bandgap of the core modes and has significant core intensity and therefore can couple to fundamental waveguide excitations. The result is that the bandgap of the core modes is effectively destroyed and we can observe transmission of a few percent at the upper edge of the core bandgap (fig. 4.35 (right)) that becomes smaller towards lower frequencies with decreasing interaction of core and cladding modes.

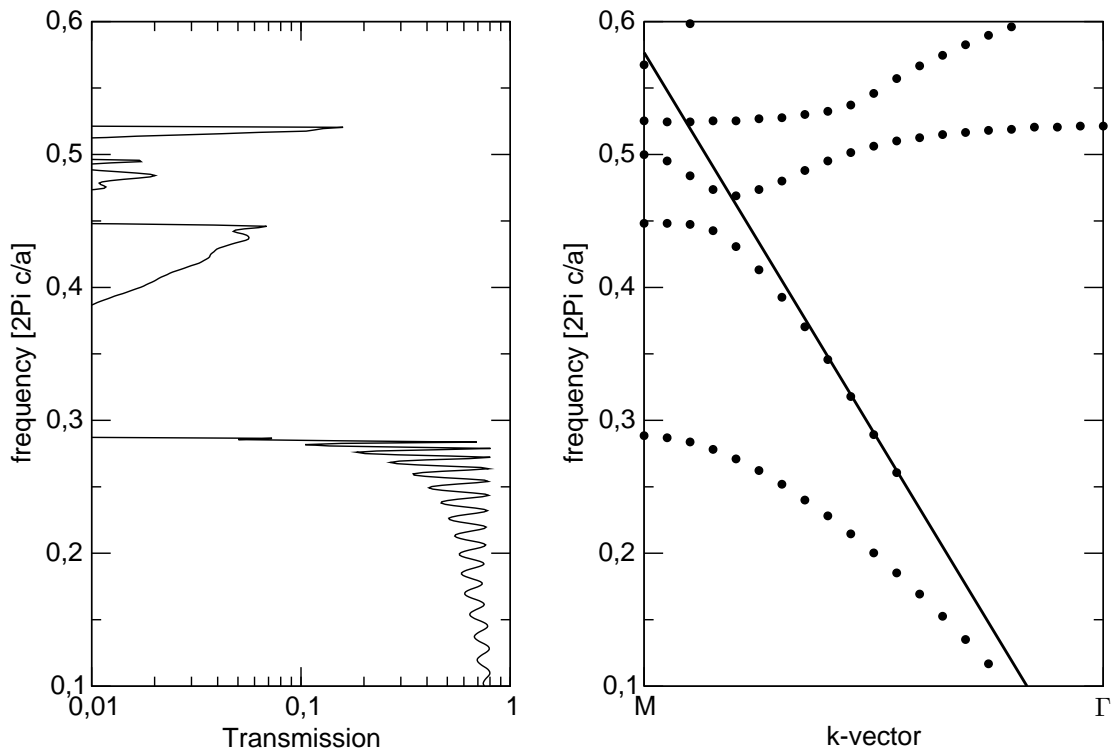


Figure 4.36: Left: Transmission through 21 rows. Right: Bandstructure for $r = 0.375a$ and $d = 1.2a$.

This effect drastically changes the picture of how photonic crystal slab structures can be addressed theoretically. It shows that it is not sufficient to treat the slab as an effective two dimensional system including losses as the only process caused by the layer structure. A comprehensive three dimensional treatment as discussed here uncovers completely new effects.

To increase the interaction of the core and cladding modes further, we now increase the hole radius to $r = 0.375a$. The lower overall effective index shifts the bands to higher frequencies.

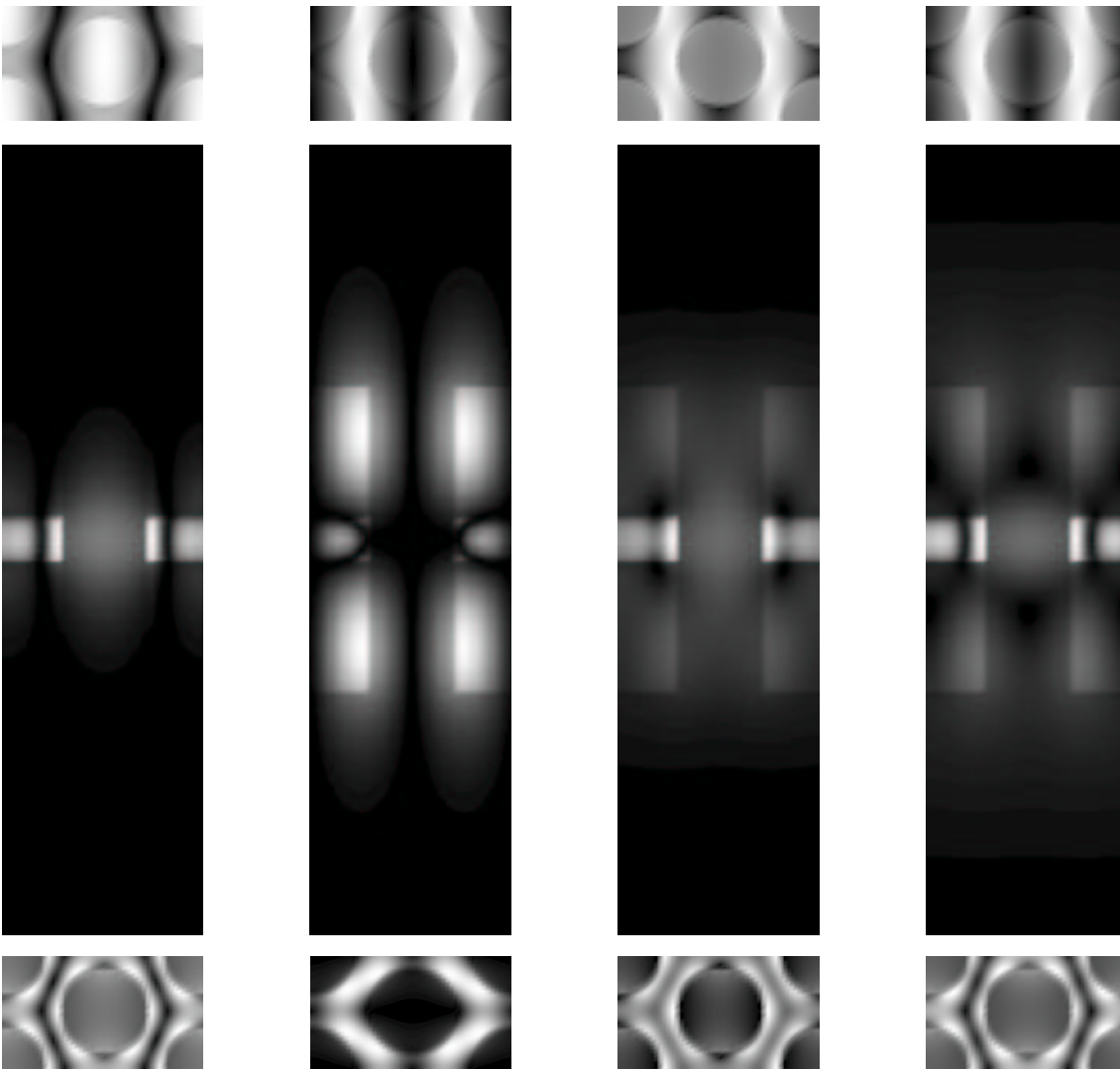


Fig. 4.37: Second core band at M .

Fig. 4.38: Cladding band at M .

Fig. 4.39: Clad. band at interaction.

Fig. 4.40: 2. core band at interaction.

As the core modes are effected more strongly than the cladding modes by this variation, the bandstructure in fig. 4.36 (right) shows only one avoided crossing of the second core and the first cladding band. We can now study this effect in more detail.

Fig. 4.37 shows the energy distribution of the second core band at M , which is far away enough from the avoided crossing so that we do not expect large mixing of the field profiles. The energy is strongly localised to the core and the in-plane cross-sections of core and cladding show no qualitative difference. The situation is similar for the cladding mode at M as shown in fig. 4.38, where we also have a "pure" cladding mode that can be derived from the cladding mode of the unpatterned layers (cp. fig. 4.29 (left)). The situation becomes different, however, when we choose a k -value closer to the avoided crossing. For the fourth k -value of the bandstructure (corresponding to $0.85\pi/a$) the mode profiles are strongly mixed as can be seen in fig. 4.39 and fig. 4.40. The energy distributions have the same qualitative properties and the energy splitting is only caused by small details of the energy localisation. The transmission behaviour through a finite sample (fig. 4.36 (left)) shows all expected features like transmission within the gap (with a maximum of $\approx 6.5\%$) and an additional gap caused by the avoided crossing of core and cladding bands. It should be mentioned here that these properties do not depend on the length of the finite sample because the involved modes lie below the air-lightline. For different sample lengths there would be only a different spacing of the Fabry-Perot oscillations.

To prove that the unexpected transmission within the core bandgap is really caused by the cladding modes, we will now look at the spatial profile of the transmission at the output planar waveguide of the transmission sample. Therefore we plot the normal component of the Poynting vector for certain frequencies along the output-plane. For the transmission spectra shown so far, the Poynting vector has been integrated along this plane for each frequency.

Fig. 4.41 shows the result for frequency 0.263. There is only transmission in the core region that does not depend on the horizontal direction. This means that only k -vectors perpendicular to the interface or, equivalently, parallel to Γ - M -direction are involved. This is also equivalent to the mode that is used as excitation in the incoupling channel. This direct mapping of incoupling and outcoupling modes without scattering into other guided modes can easily be understood, because in the bandstructure we can see that for this frequency only the fundamental core band of the crystal can be excited. The transmission value < 1 is caused by out-of-plane scattering losses at the coupling interfaces and backreflection into the incoupling waveguide. For frequency 0.430 we have a completely different picture. This frequency lies in the core bandgap. Therefore only the cladding mode can contribute to transmission. In fig. 4.42, consequently, we see strong transmission in the claddings that does not depend on the horizontal direction, because the first cladding band has (analogously to the first core band) a dominant k -component in Γ - M -direction. In the core region, nevertheless, we see a weak horizontal structure.



Fig. 4.41: P_x at $\omega = 0.263$

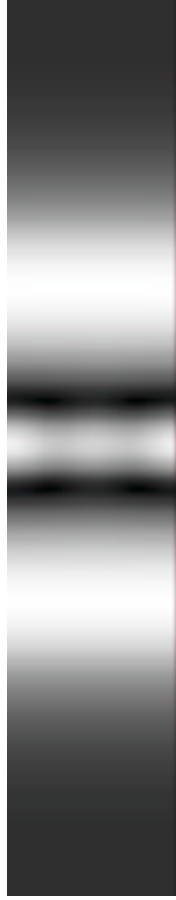


Fig. 4.42: P_x at $\omega = 0.430$



Fig. 4.43: P_x at $\omega = 0.487$



Fig. 4.44: P_x at $\omega = 0.520$

This is due to the interaction with the second core band that also allows higher order perpendicular (with respect to Γ - M) G -vector values and therefore Bragg-like spots in transmission. This can be seen more clearly if we go to a higher frequency 0.487 where the cladding mode can be excited as well as the core mode. The corresponding spatially resolved transmission in fig. 4.43 therefore shows a stronger higher order behaviour in the core while the transmission in the claddings remains the same. To complete this argumentation we also calculate the spatial distribution for frequency 0.520 which is in a region where no cladding mode should be involved. As expected, fig. 4.44 shows only transmission in the core with a horizontal pattern that clearly indicates the presence of higher order Bragg-components.

So far, we have kept the thickness of the cladding layers constant. Now we want to investigate the influence of d on the cladding modes and their interaction with the core bands. Therefore we reduce the cladding size to $d = 0.8a$ while keeping the hole radius $r = 0.375a$ and show the corresponding bandstructure and transmission results in

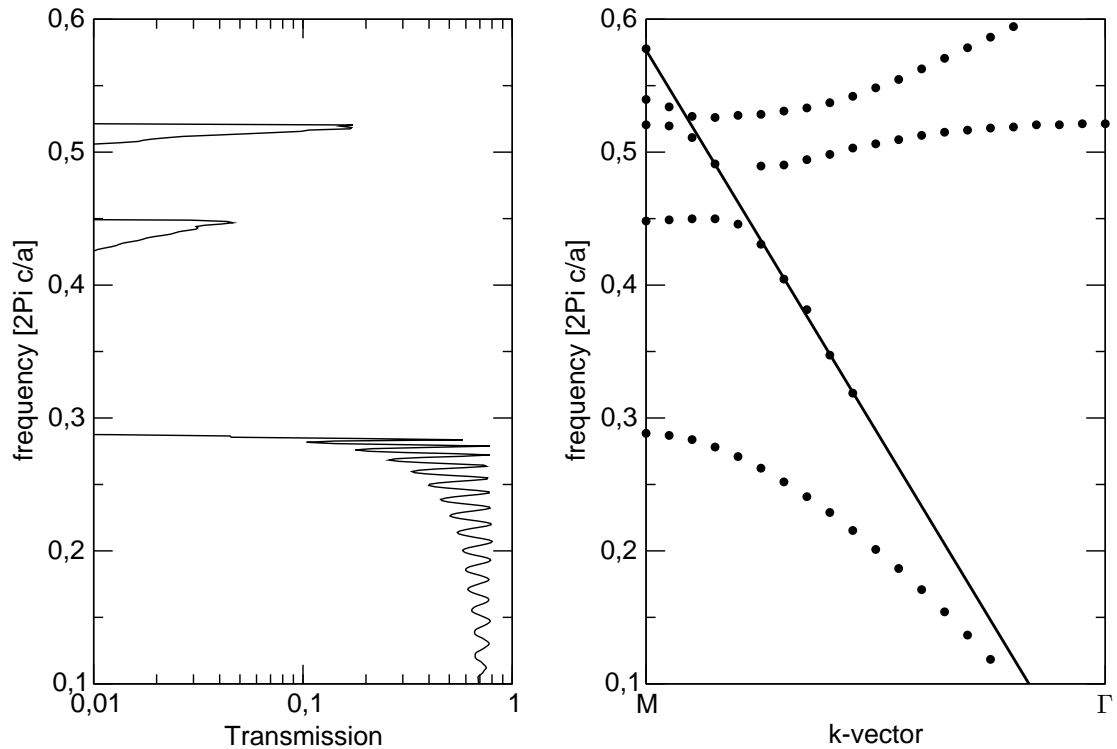


Figure 4.45: Left: Transmission through 21 rows. Right: Bandstructure for $r = 0.375a$ and $d = 0.8a$.

fig. 4.45. The smaller effective index of the cladding increases the slope of the cladding mode while the core modes are nearly unaffected. This results in an additional avoided crossing of the cladding band with the third core mode. In transmission there are only significant values for the guided first core band, the branch below the lightline of the second band and peaks for modes close to high symmetry points. For a further decrease of d we would expect a more and more negligible role of the cladding mode, because its cutoff-frequency increases while the interaction with the core decreases. Finally for $d = 0$ the system coincides with the air-bridge case. In the following, however, we will increase the cladding thickness.

As expected, for $d = 1.6a$, the slope of the cladding mode decreases as shown in fig. 4.46 (right). This causes a stronger interaction with the core band for lower frequencies and therefore a cladding transmission in fig. 4.46 (left) that is higher and reaches further into the bandgap.

However, the bandstructure also shows a peculiar new feature. The second core band

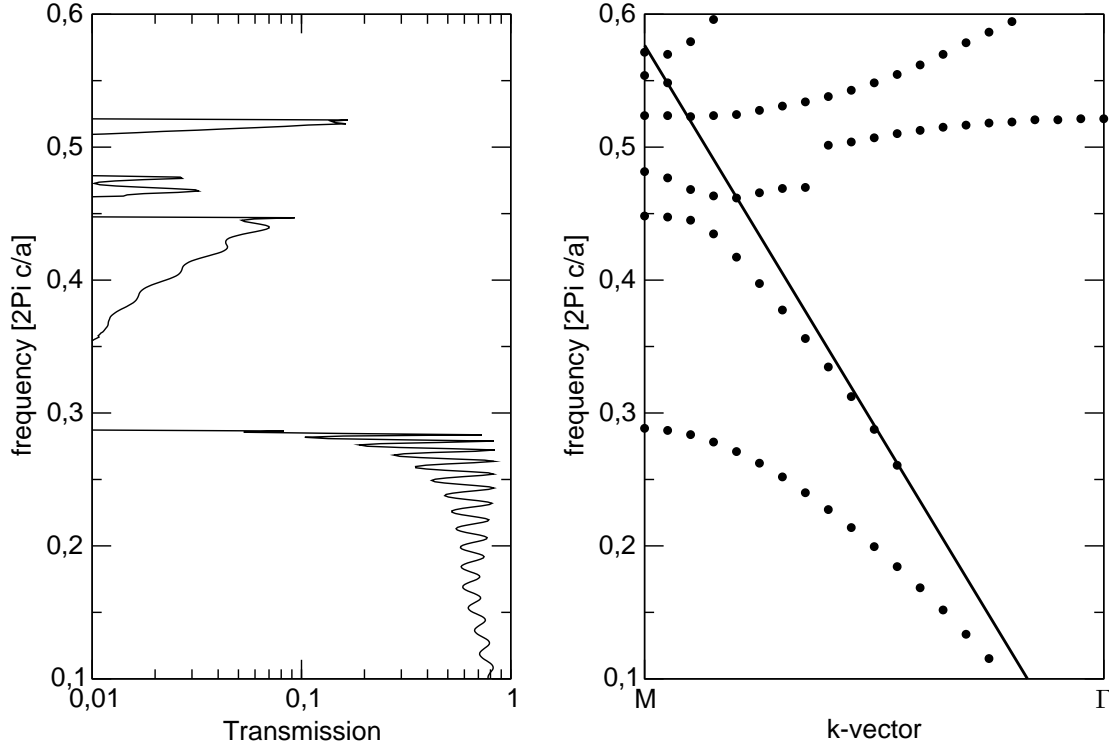


Figure 4.46: Left: Transmission through 21 rows. Right: Bandstructure for $r = 0.375a$ and $d = 1.6a$.

seems to have a discontinuous step around frequency 0.49. However, as this is not possible due to the structure of Maxwell's equations we have to look for a different explanation. We therefore calculate the mode profiles for the second core and the cladding mode at M to look if there is a fundamental change in this bands. However, as can be seen in fig. 4.47 and fig. 4.48, the core and cladding modes look very much the same as in the cases discussed before. Next we calculate the mode profiles of the second core band directly before and behind the "discontinuity". We find that these modes are extremely lossy and are difficult to excite properly. Therefore in the energy distributions in fig. 4.49 and fig. 4.50 we can even see spurious rests of the numerical excitation sources (bright small spots above and below the core in fig. 4.50 which is a typical effect when a mode is only very weakly excited or extremely lossy. However, what we can also see is a faint notion of an additional nodal plane within the cladding, leading to the suggestion that the "discontinuity" originates from an avoided crossing with a very lossy second order cladding mode, that cannot be detected itself due to fundamental limitations inherent

of the numerical method itself.

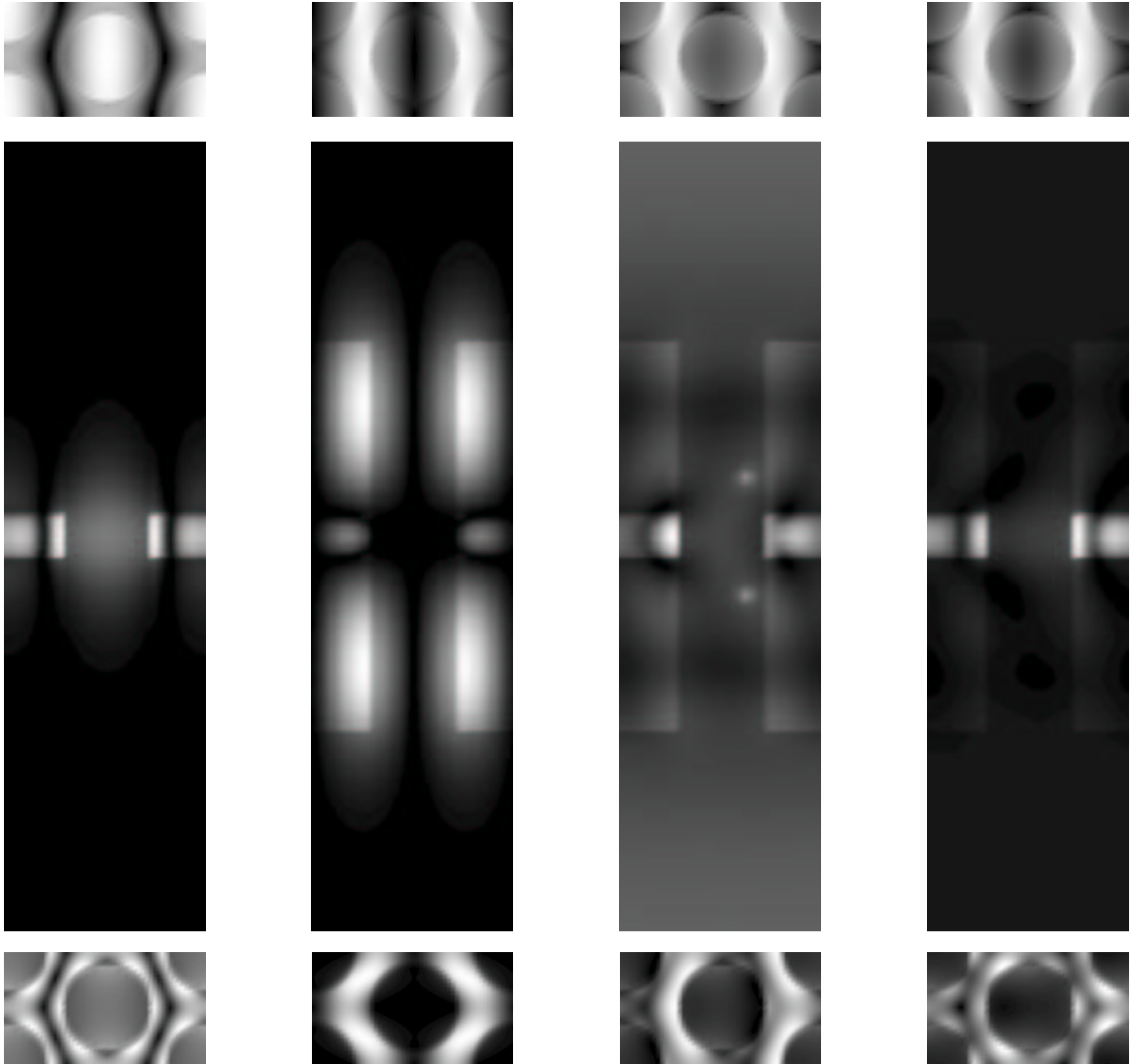


Fig. 4.47: Second core band at M .

Fig. 4.48: Cladding band at M .

Fig. 4.49: 2. core band before interaction.

Fig. 4.50: 2. core band behind interaction.

If this assumption is true, the second order cladding mode should be stabilised by a further increase of the cladding thickness. Moreover, it must exist also in an unpatterned layer-by-layer structure. Therefore we first calculate the artificially backfolded bandstructure for the unpatterned system with $d = 2.0a$. As predicted, fig. 4.51 (right) shows beside the known features an additional band (marked by a line) that has spatial properties of a higher order cladding mode as shown in fig. 4.51 (left). This band also

continues as a lossy band above the lightline. It becomes undetectable to the numerical method due to the high losses before it reaches the Γ -point.

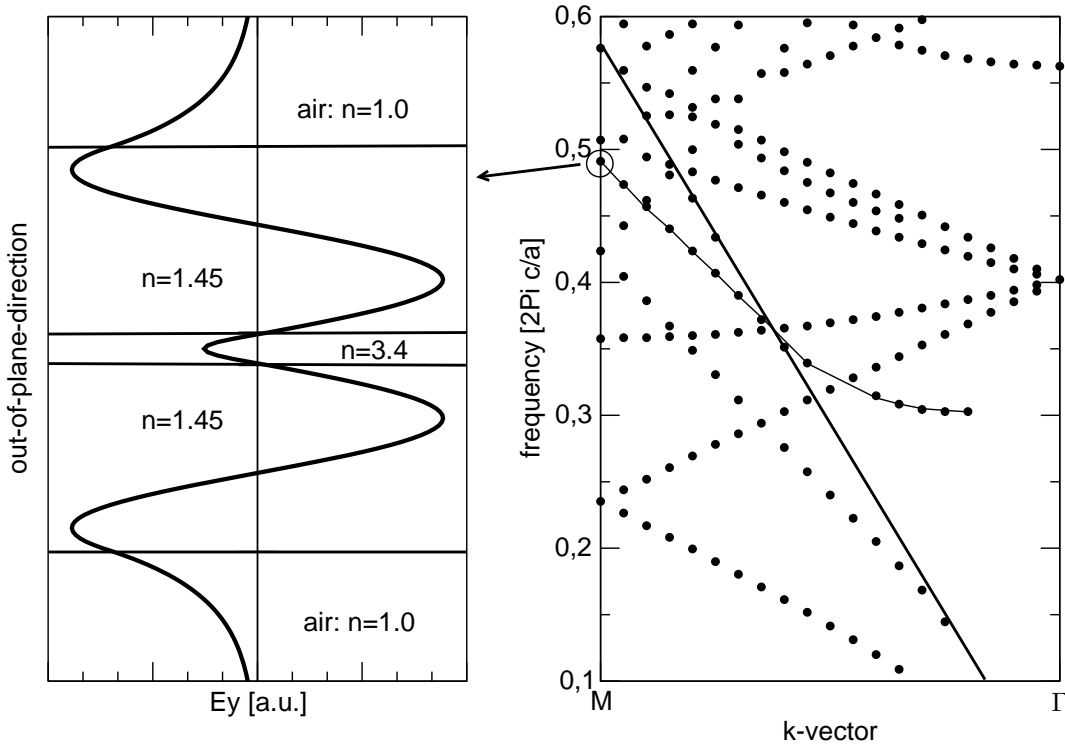


Figure 4.51: Left: Mode profile of the 2. cladding mode at M . The insets correspond to dielectric interfaces in the three-layer-system. Right: Artificially backfolded dispersion of the three-layer-system with $d = 2.0a$.

In the next step we pattern the $d = 2.0a$ -slab with $r = 0.375a$ holes. In the bandstructure in fig. 4.52 (right) we can clearly see the interaction of the second order cladding mode with the second core band. The corresponding transmission result (fig. 4.52 (left)) shows all already known features. The additional gap due to the higher order interaction cannot be proven here, because it already lies in a frequency region that has low transmission due to high losses.

To complete the proof that we found a second order cladding mode, we calculate the mode profiles of the cladding modes at $L = 0.7\pi/a$. Fig. 4.53 shows the already known first order cladding mode, while fig. 4.54 the new second order cladding mode. The still hardly detectable solution above the avoided crossing of the second cladding and the second core mode is shown in fig. 4.55 while 4.56 shows the third core band.

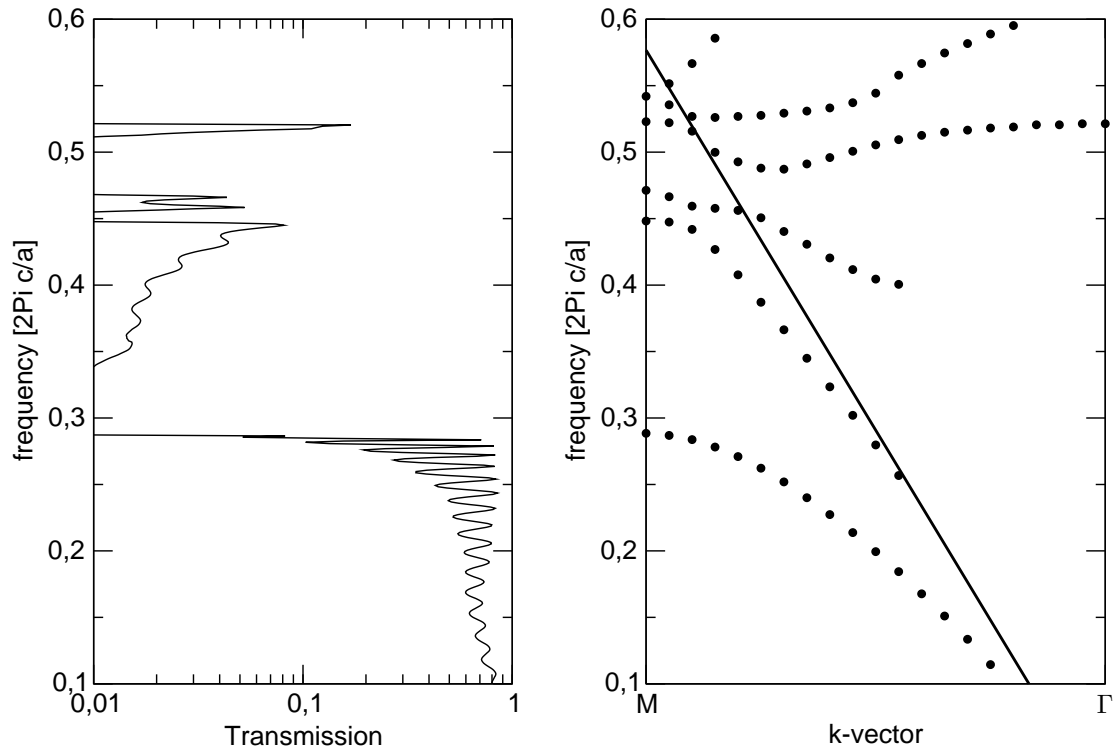


Figure 4.52: Left: Transmission through 21 rows. Right: Bandstructure for $r = 0.375a$ and $d = 2.0a$.

At the end of this section we want to summarise and generalise the picture we have obtained: Finite claddings support a new type of mode that can strongly interact with the core bands. If this happens close to the upper band edge of the core bandgap, unwanted transmission through the claddings for frequencies within the bandgap occurs. With increasing cladding thickness higher order modes appear. What does this mean in the limit $d \rightarrow \infty$? We know that in this limit we can go back to a picture with a continuum of background modes that are responsible for losses and are described by the modified lightline (see 4.3.2). The truncation to a finite cladding thickness introduces an additional boundary that discretises the background continuum. Additionally, the surrounding air introduces a new continuum of modes. From the point of view of the core modes, that are normally wanted with respect to bandgap applications, this means we have to deal with two loss mechanisms. First, the coupling to the air-continuum and second, the coupling to a discrete set of cladding modes.

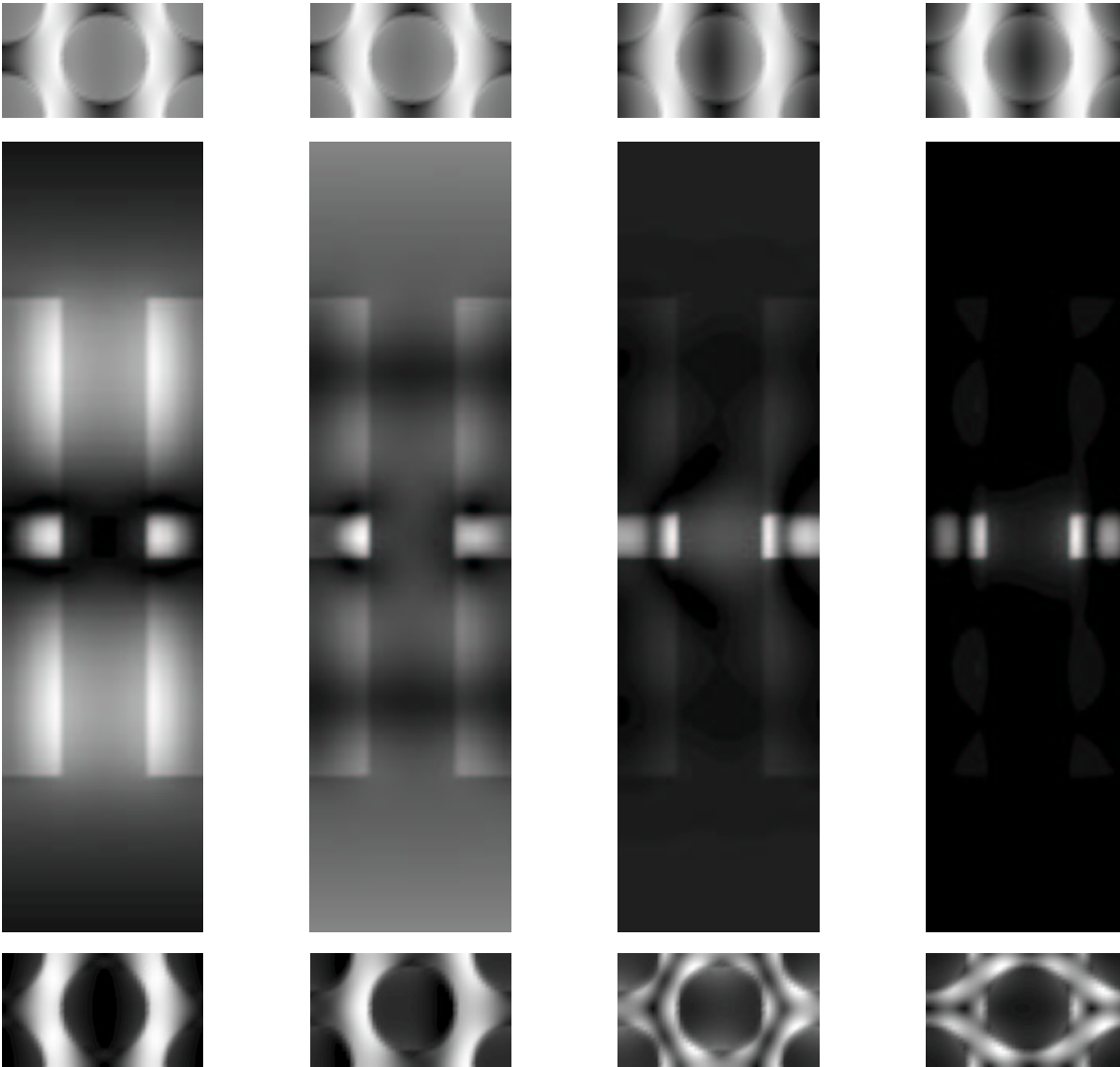


Fig. 4.53: 1. order cladding band at L .

Fig. 4.54: 2. order cladding band at L .

Fig. 4.55: 2. core band at L .

Fig. 4.56: 3. core band at L .

In the first case, the losses actually leave the system, while in the second they can be guided within the claddings and can cause unwanted effects in applications.

4.3.4 Influence of Substrate

In a final step we mount the structures presented in 4.3.3 on a bulk substrate made of SiO_2 and therefore obtain a structure that closely resembles to the realistic experimental situation. Before we analyse this structure quantitatively we argue what effects of the substrate we will expect:

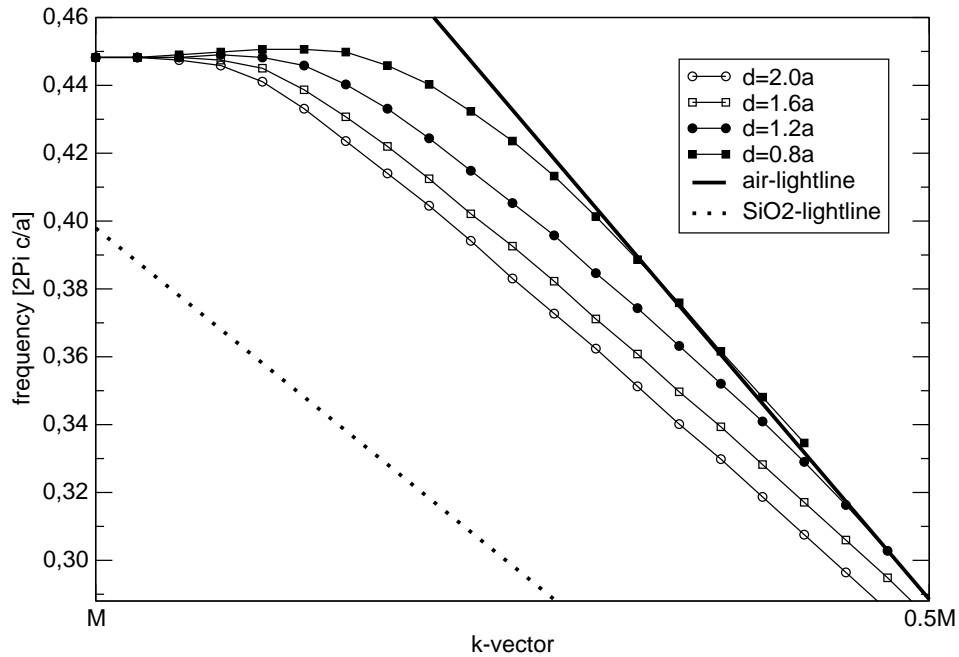


Figure 4.57: Bandstructure of cladding modes for varying cladding thickness in the frequency range of the core bandgap.

- For a sufficient cladding thickness the substrate should only have a small effect on core modes because they exponentially decay in the cladding and have only a very small spatial overlap with the substrate.
- As the substrate has a higher refractive index than the cladding, the guided cladding modes will become lossy. More generally, the lightline of air must be replaced by the dispersion relation of SiO_2 with refractive index $n = 1.45$. This should also cause losses for the second and higher core bands that were partially guided without substrate. These losses are small compared to those of the cladding modes for the reason explained, however, above.
- The losses of the cladding modes should decrease with increasing cladding thickness due to the weaker localisation.
- The substrate breaks the vertical mirror symmetry of the system. The result is a possible interaction of the even TE-modes discussed so far with odd TE- and TM as well as even TM-modes. The interaction again is larger for cladding modes,

while the separation for core modes is still valid within a certain limit.

Strictly speaking, the last item destroys the bandgap of the core modes even without considering the cladding modes at all because in the structures discussed there is no simultaneous bandgap for TE- and TM-modes. However, symmetric claddings of a sufficient thickness minimize the strength of polarisation mixing.

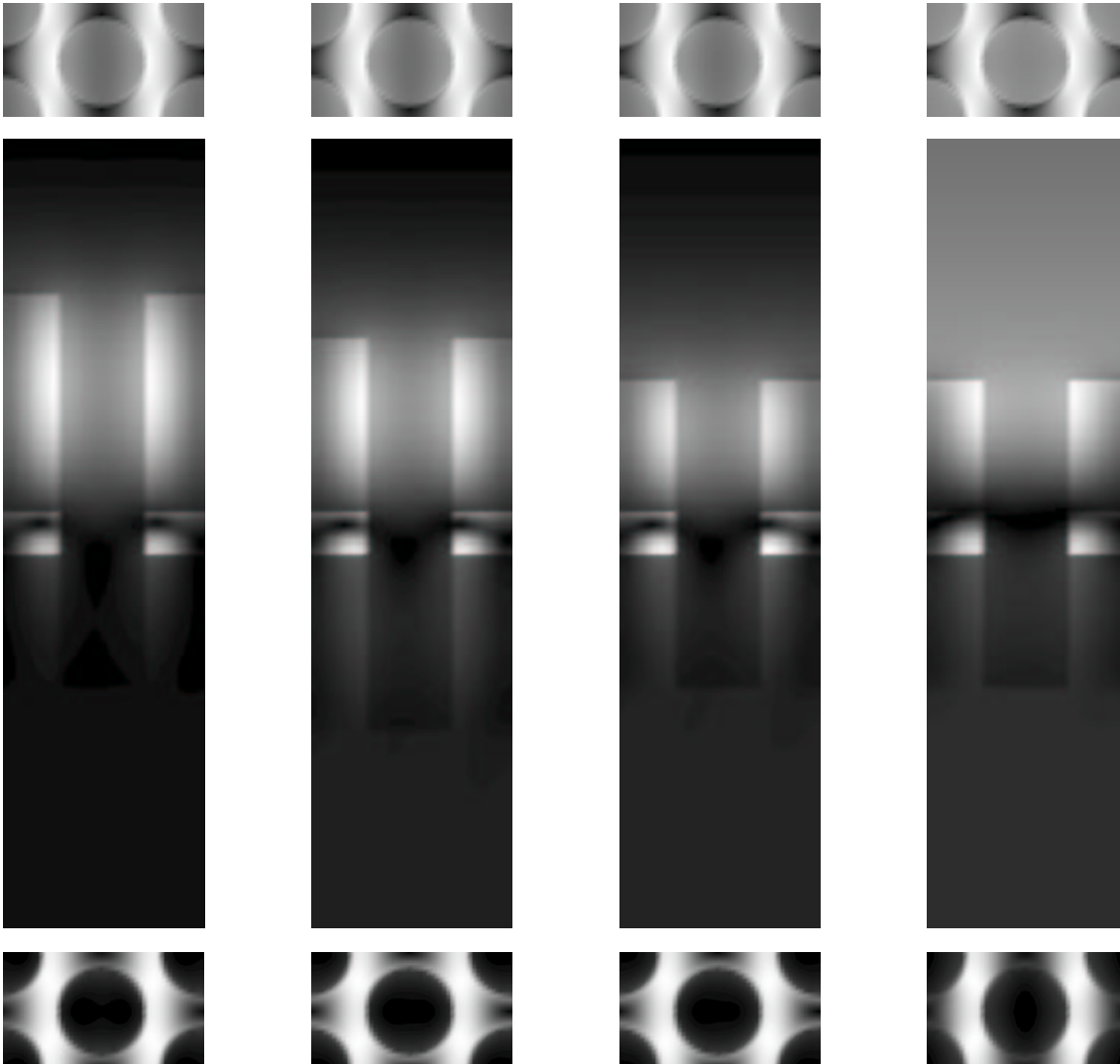


Fig. 4.58:
Cladding band
at $\omega = 0.4$ for
 $d = 2.0a$.

Fig. 4.59:
Cladding band
at $\omega = 0.4$ for
 $d = 1.6a$.

Fig. 4.60:
Cladding band
at $\omega = 0.4$ for
 $d = 1.2a$.

Fig. 4.61:
Cladding band
at lightline for
 $d = 1.2a$.

In fact, this is besides an increased mechanical stability the main reason for using cladding structures instead of membranes where these effects are intrinsically avoided.

In this context the claddings act as an optical isolator for the core modes to reduce substrate effects.

For a quantitative analysis the coupling with modes of different symmetry and polarisation unfortunately causes problems within our numerical framework because the large variety of modes that now exists in the system cannot be resolved in reasonable computation time. We will therefore focus on the most important effect, the cladding band in the core bandgap, that we can excite selectively by spatially localised excitations (see 6.3.1).

Fig. 4.57 shows the cladding bands for varying cladding thickness in the frequency range covering the bandgap of the core modes. Also included are the lightlines for SiO_2 and air that indicate that the cladding modes can in principle radiate into the substrate in all cases. For $d = 0.8a$ and $d = 1.2a$ it is difficult to determine if the modes are guided with respect to the cladding-air-interface because the bands come very close to the air-lightline within the displayed frequency range.

To clarify the influence of the cladding thickness on the spatial energy distribution we calculate the spatial profile at frequency $\omega = 0.4$ for cladding thicknesses $d = 1.2a$, $d = 1.6a$ and $d = 2.0a$ as displayed in fig. 4.58 to 4.60. It can be clearly seen that the modes strongly localise energy in the top cladding and the core while in the lower cladding there are negligible values. With respect to mode symmetry this means that the modes are neither odd nor even but a superposition of both with contributions in similar order of magnitudes. Also the maximum in the core region is shifted out of the center with the consequence of a smaller but still non-vanishing coupling to even waveguide excitations. Moreover it can be seen that the relative part of energy localised in the core decreases with increasing cladding thickness. This is an indication that the coupling to an external waveguide excitation is weaker for increasing cladding thickness. Normally, these issues should be clarified by corresponding transmission simulations. However, as the cladding modes are lossy we would see no transmission at all for sample lengths large enough to sort out finite size (especially Fabry-Perot) effects.

Therefore we will now analyse the strength of these losses for the bands displayed in fig. 4.57. Fig. 4.62 shows the corresponding imaginary parts of the frequencies. The behaviour close to the upper band edge is complicated because here the interaction with the second core band takes place and the mode profiles and, consequently, also the different loss behaviours mix. However, if we go further into the bandgap we can see that, as expected, the losses increase with decreasing cladding thickness. For $d = 2.0$ and $d = 1.6$ we can observe a small smooth increase of the losses towards the lower band edge. In the case of lower cladding thicknesses there is an additional minimum that corresponds roughly to the frequency where the cladding band reaches the air-lightline. For frequencies below, the loss behaviour increases stronger than for frequencies above,

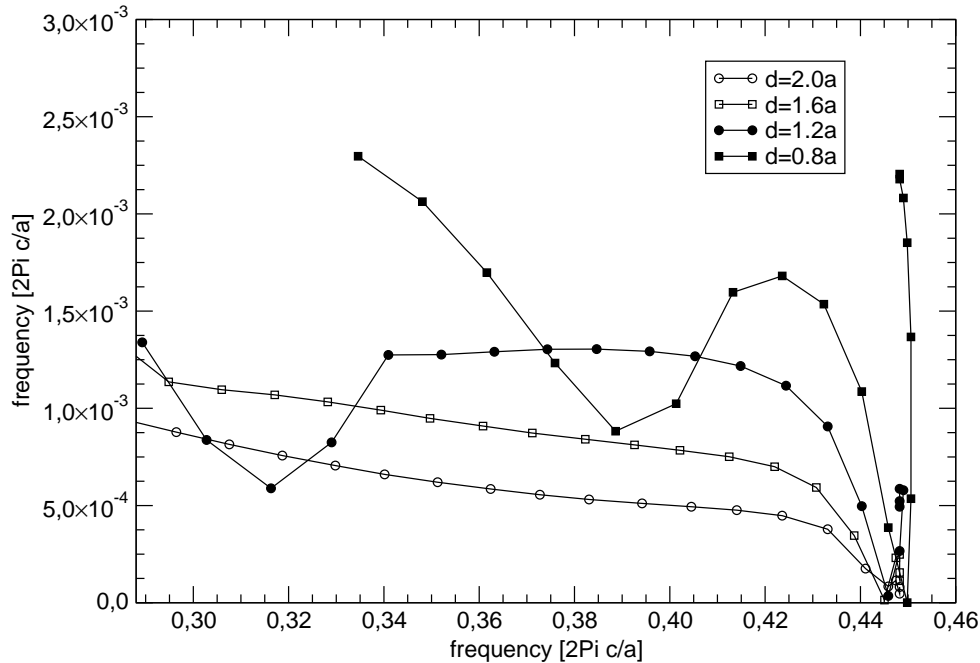


Figure 4.62: Losses of the cladding bands for varying cladding thickness in the frequency range of the core bandgap.

indicating that radiation losses now occur into the air as well as into the substrate. The energy distribution at this minimum for $d = 1.2$ as displayed in fig. 4.61 shows that the mode is extended into the air region very strongly but still guided in this respect. The origin of the formation of this minimum in losses is not yet clear and will be subject of further investigations.

The results in this subsection indicate that lossy cladding modes may act as a loss mechanism in realistic photonic crystal slab structures in Si/SiO_2 -structures. Due to the computational effort and the large variety of parameters the comprehensive understanding of all related effects will require intensive further research.

4.4 Conclusion

In this section we have analysed several aspects of the interaction of a two-dimensional photonic crystal slab with a vertical layer structure into which the slab is embedded.

Starting with the fundamental optical properties of an unpatterned dielectric slab we developed a simple air-bridge structure, where we discussed the bandstructures as well as eigenmodes, gap size, radiation losses and transmission properties in dependance of hole radius. Gradually, this simple structure has been modified to more realistic cases. For symmetric semi-infinite claddings we discussed the influence of the cladding index. Then we focused on finite claddings of varying thickness in an Si/SiO_2 -system. We discovered the existence of cladding modes, i.e. modes with significant, non-decaying intensity in the cladding layers for frequencies lying in the bandgap of the core modes and identified these cladding modes to lead to unexpected transmission. To our knowledge this has not been reported before. A detailed analysis of the dependance on the cladding thickness also revealed the existence of higher order cladding modes. In the last part we demonstrated that these cladding modes become lossy when the structure is mounted onto a SiO_2 -substrate. Cladding modes may act as a loss mechanism in bandgap applications and will be therefore subject of intensive further investigations.

5 Spontaneous Emission in Inverted Opals

5.1 Introduction

The discussion of the optical properties of photonic crystals presented in the preceding chapters has been done in terms of bandstructure and eigenmodes for the ideal infinitely extended structure and in terms of an optical response to external field excitations as far as more realistic finite systems were concerned. Now we want to focus on the physical processes that occur when the emitter itself (in the simplest case an atomic dipole) is placed within the structure. It was well known before the conception of photonic crystals that a dielectric distribution in the vicinity of an emitter can modify its emission process because, in a classical picture, field components that are reflected back to the emitter can interact with it. In a frequency domain picture this can be explained by the local coupling strength of the emitter with the mode bath. A simple example is a one-dimensional resonator that supports standing waves as eigenmodes. When the emitter is located in a node of the standing wave it cannot couple to the mode bath and spontaneous emission is suppressed, while enhancement can be observed when the emitter is located at maxima of the resonator mode. In a photonic crystal there ideally is a range of frequency (the bandgap) where no modes exist at all. Therefore there should be no coupling for emitters having a transition frequency lying in the bandgap regardless of position. Actually, this was the original motivation for the suggestion of photonic crystals by John and Yablonovitch in 1987 [1, 2]. The technological applications described in chapter 4 that now mainly drive the progress in the field of photonic crystals are a later development. In this chapter we will present the physical basis of the spontaneous emission process in a dielectric environment and show results for the modified spontaneous emission in a finite inverse opal structure within the weak coupling regime. For the discussion of the fundamental theoretical description we will closely follow the argumentation of [30].

5.2 Weak and Strong Coupling Regime

In the first studies of a single two-level atom coupling to a single electromagnetic cavity mode by Jaynes and Cummings (for further reading about the Jaynes-Cummings model see e.g. [31]) it became obvious that the coupling strength κ between atom and cavity mode, estimated by

$$\kappa = \frac{\mu_{12}}{\hbar} \sqrt{\frac{2\pi\hbar\Omega}{V}} \quad (5.1)$$

is an important parameter to classify the system qualitatively. It is determined by the atomic transition frequency Ω , the cavity volume V , and the dipole matrix element μ_{12} of the atom. \hbar represents Planck's constant divided by 2π . If we compare κ with the dipole dephasing rate γ_{12} and the decay rate of the cavity photon Γ_{cav} we have to distinguish the strong coupling regime

$$\kappa \gg (\gamma_{12}, \Gamma_{cav}) \quad (5.2)$$

from the weak coupling regime

$$\kappa \ll (\gamma_{12}, \Gamma_{cav}) \quad (5.3)$$

which are also referred in literature as the non-Markovian and Markovian regime, respectively. Physically, in the strong coupling regime we have a significant probability of reabsorption of the emitted photon, leading to an oscillatory behaviour of the expectation value of the excited state occupation number of the atom. The quantum optical phenomena related to this behaviour and the particular optical properties of photonic crystals have been extensively studied in [5, 6, 32, 33, 34, 35] but are also controversially discussed [36, 37, 38]. In this work we will limit ourselves to the discussion of the weak coupling regime where we can assume an exponential decay due to a pure dipole dephasing rate γ_{12} . In particular, we will study the influence of a photonic crystal environment on the spontaneous emission rate

$$\gamma = \frac{\frac{d}{dt} \langle \hat{N}_2 \rangle}{\overline{n_2}} \quad (5.4)$$

where $\langle \hat{N}_2 \rangle$ is the expectation value of the occupation number operator of the excited state and $\overline{n_2}$ the ensemble averaged occupation number.

5.3 Classical and Quantum Description Within the Weak Coupling Regime

In this section we will give the key relations for deriving the spontaneous emission rate within the weak coupling regime and show an analogy between the classically and quantum mechanically obtained expressions that will allow us later to calculate γ within a

classical FDTD-scheme. The derivation is not comprehensive but will only show the steps that are important for the physical understanding. For a more detailed discussion see [30]. Following the argumentation in [30] we do not use electric or magnetic fields for the derivation but the vector potential $\vec{A}(\vec{r}, t)$ under the Coulomb gauge condition

$$\nabla \left[\epsilon(\vec{r}) \vec{A}(\vec{r}, t) \right] = 0 \quad (5.5)$$

We will denote classical vector fields by an overarrow while quantum mechanical vector operators are written bold with an overhat.

5.3.1 Quantum Approach

If we want to discuss the vector potential in terms of the eigenmodes of a photonic crystal we should first introduce a general expansion of the vector field operator into a complete set of eigenfunctions:

$$\hat{\mathbf{A}}(\vec{r}, t) = \sum_n \sqrt{\frac{2\pi\hbar c^2}{\omega_n}} \left[\hat{a}_n \vec{A}_n(\vec{r}) + \hat{a}_n^\dagger \vec{A}_n^*(\vec{r}) \right] \quad (5.6)$$

with \hat{a}_n and \hat{a}_n^\dagger the annihilation and creation operator of a photon in the n^{th} mode, which has frequency ω_n and spatial profile $\vec{A}_n(\vec{r})$. The star denotes the complex conjugated value. If we couple this mode system to a two-level system with transition frequency Ω we obtain an Hamiltonian of the form

$$\hat{H} = E_2 \hat{b}_2^\dagger \hat{b}_2 + E_1 \hat{b}_1^\dagger \hat{b}_1 + \sum_n \hbar \omega_n \hat{a}_n^\dagger \hat{a}_n + \sum_n \left[\hbar \kappa_n \hat{b}_2^\dagger \hat{b}_1 \hat{a}_n + \hbar \kappa_n^* \hat{a}_n^\dagger \hat{b}_1^\dagger \hat{b}_2 \right] \quad (5.7)$$

where \hat{b}_i and \hat{b}_i^\dagger are the annihilation and creation operator of state i ($i = 1$: ground state, $i = 2$: excited state) and E_i the corresponding energies. κ_n represents the coupling strength of the two-level system with mode n and is given by

$$\kappa_n = -\frac{e}{\hbar m} \sqrt{\frac{2\pi\hbar}{\omega_n}} \vec{p}_{12} \cdot \vec{A}(\vec{r}_0) \quad (5.8)$$

in dipole approximation for an emitter located at \vec{r}_0 and dipole matrix element \vec{p}_{12} . e and m are electron charge and mass, respectively.

As we are interested in the time derivative

$$\frac{d}{dt} \hat{N}_2 = \frac{d}{dt} (\hat{b}_2^\dagger \hat{b}_2) \quad (5.9)$$

of the occupation number operator of the excited state for the calculation of the spontaneous emission (see eq. 5.4) we now use eq. 5.7 to set up the Heisenberg equations of motion for \hat{N}_2 . To keep this equation of motion consistent with our weak coupling assumptions we have to introduce a quantum Langevin operator that represents the dephasing and therefore the decay of the excited state into the modes of the dielectric structure. Further analysis of this Langevin operator results in an interpretation as a fluctuating quantum current $\hat{\mathbf{j}}_{fluc}(\vec{r}, t)$ that is responsible for the spontaneous emission now described by the equation

$$\frac{d}{dt}\hat{N}_{2,spont} = \frac{i}{\hbar c} \int d^3\vec{r} \left[\hat{\mathbf{j}}_{fluc}^+(\vec{r}, t) \cdot \hat{\mathbf{A}}^-(\vec{r}, t) - \hat{\mathbf{A}}^+(\vec{r}, t) \cdot \hat{\mathbf{j}}_{fluc}^-(\vec{r}, t) \right] \quad (5.10)$$

where the + and - superscripts denote parts belonging to positive and negative frequencies, respectively. To evaluate eq. 5.10 we have to relate $\hat{\mathbf{j}}_{fluc}(\vec{r}, t)$ and $\hat{\mathbf{A}}(\vec{r}, t)$. This can be done by a classical Green's function ansatz that results in

$$\hat{\mathbf{A}}(\vec{r}, \omega) = -\frac{4\pi}{c} \int d^3\vec{r}' \vec{e}_\alpha G_{\alpha\beta}^\omega(\vec{r}, \vec{r}') \hat{\mathbf{j}}_{fluc,\beta}(\vec{r}', \omega) \quad (5.11)$$

in frequency domain and the subscripts α and β denoting Cartesian vector components while \vec{e} represents the polarisation vector. Using eq. 5.11 in eq. 5.10 and taking the ensemble average finally results in the spontaneous emission rate

$$\gamma = \frac{\frac{d}{dt} \langle \hat{N}_2 \rangle}{\bar{n}_2} = -\frac{4}{\hbar c^2} \frac{e^2}{m^2} p_{12,\alpha} p_{12,\beta} \int d\omega \frac{2\gamma_{12}}{(\Omega - \omega)^2 + \gamma_{12}^2} \cdot \text{Im} [G_{\alpha\beta}^\omega(\vec{r}_0, \vec{r}_0)] \quad (5.12)$$

5.3.2 Classical Approach

Now we calculate the electromagnetic energy W_{rad} radiated by a classical oscillating dipole current and try to derive a form similar to eq. 5.12. We start with the equation that describes the work that is done by an electric field \vec{E} to a current \vec{j}

$$W_{rad} = - \int dt \int d^3\vec{r} \vec{j}(\vec{r}, t) \cdot \vec{E}(\vec{r}, t) \quad (5.13)$$

For convenience at a later stage, $\vec{j}(\vec{r}, t)$ and $\vec{A}(\vec{r}, t)$ are split into positive and negative frequency parts (each the conjugate complex of the other) when fourier transformed

$$\vec{j}(\vec{r}, t) = \frac{1}{2\sqrt{2\pi}} \left[\int_{-\infty}^{\infty} d\omega \vec{j}(\vec{r}, \omega) e^{-i\omega t} + \int_{-\infty}^{\infty} d\omega \vec{j}^*(\vec{r}, \omega) e^{i\omega t} \right] \quad (5.14)$$

$$\vec{A}(\vec{r}, t) = \frac{1}{2\sqrt{2\pi}} \left[\int_{-\infty}^{\infty} d\omega \vec{A}(\vec{r}, \omega) e^{-i\omega t} + \int_{-\infty}^{\infty} d\omega \vec{A}^*(\vec{r}, \omega) e^{i\omega t} \right] \quad (5.15)$$

In frequency domain we can, analogously to the quantum case, relate the vector potential to the current by the classical Green's function

$$\vec{A}(\vec{r}, \omega) = -\frac{4\pi}{c} \int d^3\vec{r}' \vec{e}_\alpha G_{\alpha\beta}^\omega(\vec{r}, \vec{r}') j_\beta(\vec{r}', \omega) \quad (5.16)$$

For a pointlike current source of the form

$$\vec{j}(\vec{r}, \omega) = \frac{e}{m} j_\omega \delta(\vec{r} - \vec{r}_0) \vec{p}_{12} \quad (5.17)$$

eq. 5.16 simplifies to

$$\vec{A}(\vec{r}, \omega) = -j_\omega \frac{4\pi e}{mc} \vec{e}_\alpha G_{\alpha\beta}^\omega(\vec{r}, \vec{r}_0) p_{12,\beta} \quad (5.18)$$

Now we insert eq. 5.14 and eq. 5.18 into eq. 5.13 and evaluate the resulting expression. After replacing ω by Ω , which is equivalent to ignoring a small term of the order γ_{12}/Ω we end up with

$$W_{rad} = -\frac{2\pi e^2}{c^2 m^2} p_{12,\alpha} p_{12,\beta} \Omega \int d\omega |j_\omega|^2 \text{Im} [G_{\alpha\beta}^\omega(\vec{r}_0, \vec{r}_0)] \quad (5.19)$$

It is now obvious that if we choose a Lorentzian lineshape for j_ω

$$j_\omega = \frac{1}{i(\Omega - \omega) + \gamma_{12}} \quad (5.20)$$

the classically radiated energy is proportional to the quantum mechanically obtained spontaneous emission rate obtained in eq. 5.12. In particular this means that if we know the values for the spontaneous emission rate and the radiated energy in free space (which is accessible analytically) we can calculate the spontaneous emission in the vicinity of a dielectric structure via a purely classical approach with an oscillating current source, according to

$$\gamma_{cav} = \gamma_{free} \frac{W_{cav}}{W_{free}} \quad (5.21)$$

or, as used in this work, we can directly define a modification factor normalised by the free space rate as

$$\Gamma_{cav} = \frac{W_{cav}}{W_{free}} \quad (5.22)$$

where $\Gamma < 1$ can be interpreted as suppression and $\Gamma > 1$ as enhancement of the free space spontaneous emission rate.

Up to this point we made no statement about the dielectric structure and therefore the precise structure of the eigenmode basis. It is clear that the modification factor Γ can be strongly dependant on the transition frequency and the position within the dielectric structure. To obtain the full knowledge about $\Gamma(\vec{r}, \omega)$ we would have to know the complete mode structure. In most practical cases, especially in complex photonic crystals, this cannot be achieved. Moreover, even if the mode structure of the ideal crystal is known, interesting questions concern finite structures that are principally lossy. The big advantage of the classical approach presented is that within an FDTD-algorithm $\Gamma(\omega)$ can be determined at a single position \vec{r}_0 without the explicit knowledge of the eigenmodes, by inserting a probe current source at \vec{r}_0 and time integrating the radiated energy. The physical origin of the modification of the radiated energy is the interaction of backreflected parts of the emitted field that interact with the current. The derivation of equivalency of classical and quantum mechanical results was done for a classical emitter with a Lorentzian emission spectrum corresponding to the exponential decay in time caused by the Langevin operator within the weak coupling regime. In the classical picture this is not mandatory because γ_{12} is an arbitrary parameter. We can assume a vanishing linewidth leading to a monochromatic excitation and as a result get the strength of the interaction of backreflected fields with the current source for just a single frequency. Generalising these arguments and using the linearity and fourier properties of the classical fields we can excite the system by a temporal arbitrary shaped pulsed source $\vec{j}(\omega, \vec{r}_0)$, fourier transform the electric field at the position of the source and calculating $\Gamma_{cav}(\omega, \vec{r}_0)$ as

$$\Gamma_{cav}(\omega, \vec{r}_0) = \frac{W_{cav}}{W_{free}} = \frac{\vec{E}_{cav}(\omega, \vec{r}_0) \vec{j}_{cav}(\omega, \vec{r}_0)}{\vec{E}_{free}(\omega, \vec{r}_0) \vec{j}_{free}(\omega, \vec{r}_0)} \quad (5.23)$$

Then, the spontaneous emission rate of an emitter with dephasing rate γ_{12} can be calculated by a convolution of $\Gamma_{vac}(\omega, \vec{r})$ with the corresponding Lorentzian with width γ_{12} . This procedure requires obviously that γ_{12} is independant of the dielectric structure which is also a consequence of the weak coupling assumption. We also note that $\Gamma_{cav}(\omega, \vec{r})$ is equivalent to the local density of states as used in [33].

5.4 Single Dielectric Sphere

Before we start to analyse the spontaneous emission in a photonic crystal structure we want to verify our numerical method by the comparison with results that are obtainable analytically. We choose as a test system a dielectric sphere of radius r and refractive index $n = 3.0$ embedded in free space which means the application of absorbing boundary conditions in all three dimensions of the numerical domain. The analytical expressions for the spontaneous emission modification factor $\Gamma(\omega, \vec{r})$ are given in [39, 40]. For simplicity we will only consider the case of an emitter placed in the center of the sphere because by this we circumvent polarisation issues due the rotational symmetry of the resulting system. Fig. 5.1 shows the comparison of the analytical results with the numerical calculation. The excellent quantitative agreement legitimates the application of this method for general dielectric structures.

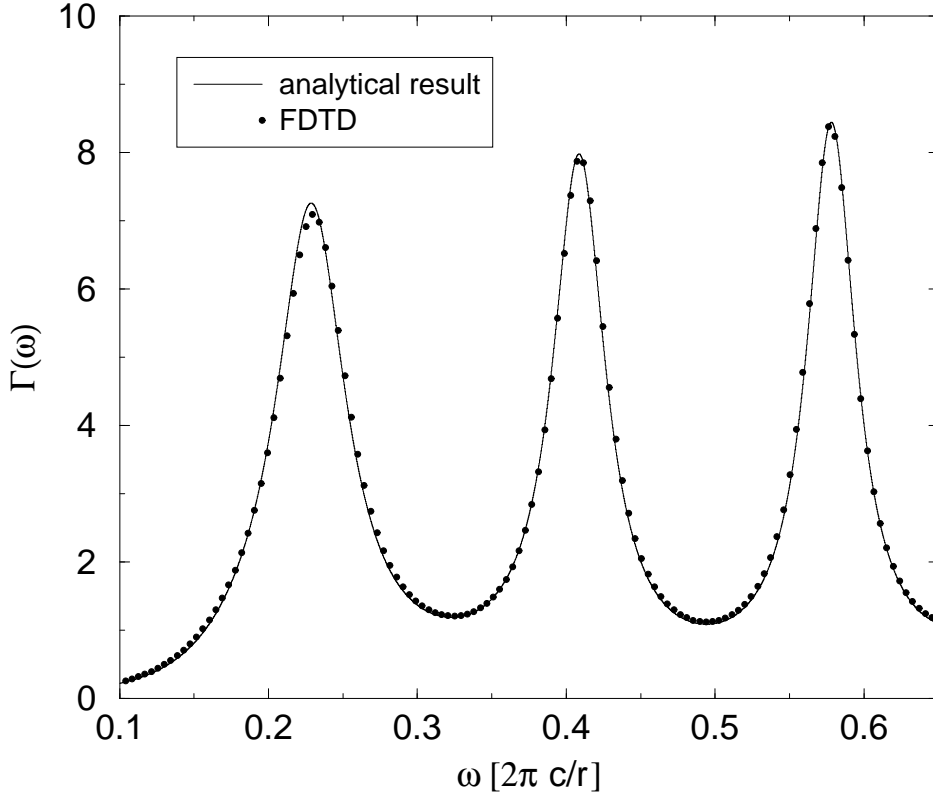


Figure 5.1: Modification factor $\Gamma(\omega)$ for a dipole in the center of a dielectric sphere with radius r and refractive index $n = 3.0$: Comparison between analytical result (line) and FDTD (dots).

5.5 Inverted Opals

For the investigation of the modification and especially the suppression of spontaneous emission within the bandgap, the two-dimensional structures considered so far in this work are not ideally suited because they do not exhibit a bandgap in the sense of a vanishing local density of states. While for the application for passive optical devices this is not prohibiting because we can selectively excite desired modes (e.g. the guided or quasi-guided ones) an emitter embedded in the structure will more or less couple to the whole mode bath including the radiative modes that destroy the gap. This has been investigated e.g. in [41]. We therefore have to choose a full three dimensional periodic structure to clearly identify the physical effects. From the variety of three dimensional photonic crystals exhibiting a full bandgap that have been proposed theoretically and/or realised experimentally we choose the class of inverted opal structures. This class of crystals has distinguished itself as easy to fabricate by self-organising processes [42, 43, 44] on a relative large scale. Therefore it is widely used for the investigation of fundamental physical processes in photonic crystals [3, 12] where its largest disadvantage, the difficult controlled inclusion of defects that is necessary for most technological applications, does not play an important role. It is not the purpose of this work to discuss the structure itself or dependencies on geometry and material parameters because this is described extensively in literature [45]. We just choose one example system with parameters that are on one hand as realistic as possible from a fabrication point of view but are adjusted in a way that the desired optical properties like the bandgap are easily observable.

5.5.1 Geometrical Setup

The geometrical distribution of dielectric material in an inverted opal can be understood most easily by shortly reviewing the fabrication process: Polystyrene spheres of radius r are allowed to sediment slowly in a liquid, e.g. an alcohol. Due to self-organising processes they arrange in a face-centered-cubic (fcc) close packed lattice. Then the liquid is evaporated and the system infiltrated by an high index material. Ideally, as will be assumed here, all voids between the spheres are completely filled. In practice oftenly the high index material only covers the polystyrene sphere leading to a more complicated structure. After the infiltration the system is heated and the polystyrene spheres are also evaporated leaving an fcc-arrangement of air-spheres in a dielectric matrix with refractive index n . In practice, the evaporation of the polystyrene spheres leads to a sintering of the ideally touching air spheres. This effect is incorporated in our model by cylindrical connections of the air spheres with radius $r_s = 0.4r$. Fig. 5.2 shows the dielectric interfaces of a conventional unit cell of the structure. The lattice constant a is defined as the edge length of the conventional cell and not, as often done for other lattices, as the length of a primitive lattice vector which is $\sqrt{3}/2 \cdot a$ in this case. The conventional unit cell (which consists of four primitive cells) is highly symmetric. As we want to analyse spatial dependencies of the spontaneous emission later on we can

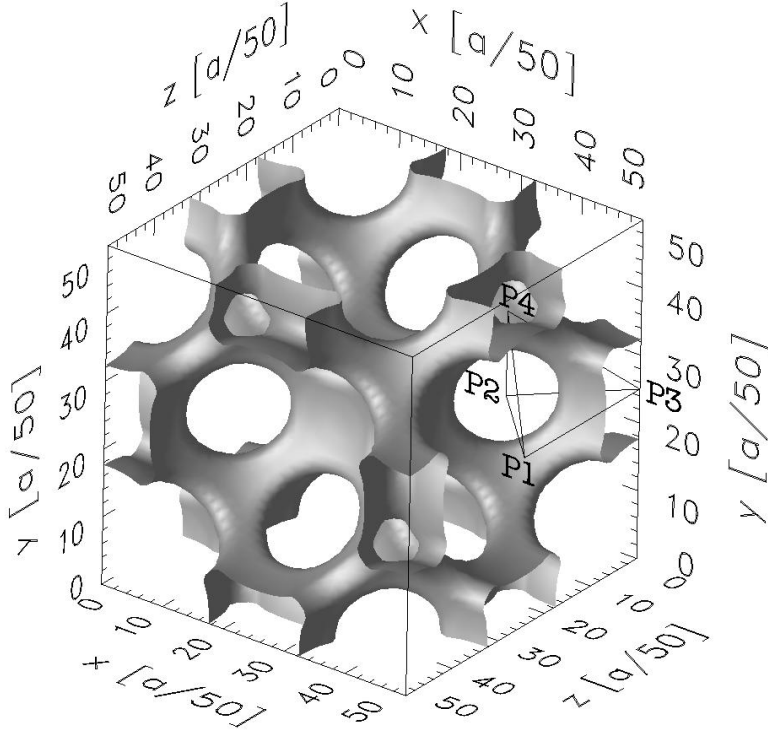


Figure 5.2: Dielectric structure of a conventional unit cell of an inverse opal. The inset shows the irreducible tetragonal volume in real space limited by the high symmetry point P_1 - P_4 . The units are given in discrete gridpoints of the numerical mesh.

reduce the problem by identifying the irreducible part of the unit cell that cannot be mapped by symmetry operations to another. We find that the conventional unit cell has a 48-fold symmetry and that we can reduce to a tetragonal space volume limited by the high symmetry points P_i ($i = 1..4$) as shown in the inset of fig. 5.2. This geometrical setup can also be interpreted as an interconnected lattice of octagonal and tetragonal volumes of high dielectric material. It is important for the further discussion to note that P_1 is located in the center of an air sphere, P_2 at the touching point of two air spheres (therefore in the center of the cylindrical interconnect), P_3 in the center of an octagonal volume and P_4 in the center of a tetragonal volume. This conventional unit cell is used for bandstructure calculation with periodic boundary conditions applied in all space directions.

For the calculation of the modified spontaneous emission we also want to include the finiteness of the system. Principally, the infinite case can be addressed by a frequency domain mode expansion as well. This has been already demonstrated with low accuracy due to numerical constraints in [47]. We therefore model cubic crystallites with edge

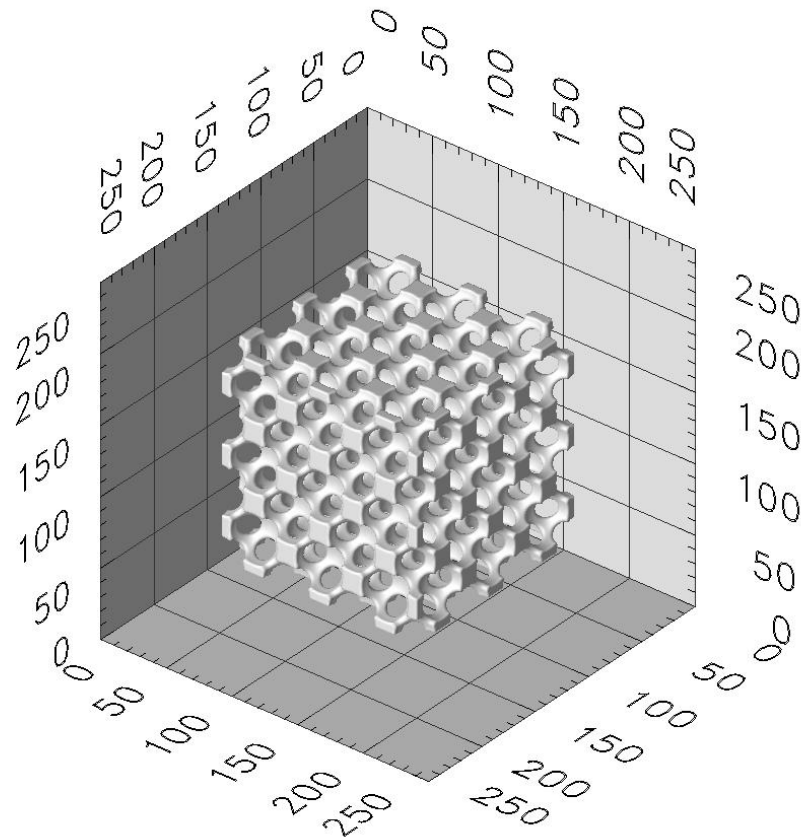


Figure 5.3: Finite crystallite of edge length $3a$ embedded in free space. The units are given in discrete gridpoints of the numerical mesh.

lengths of $l = 3a$, $l = 5a$ and $l = 7a$, respectively, that are enclosed by PML boundaries. This system sizes correspond to 108, 500 and 1372 single scatterers. Fig. 5.3 shows the crystallite with edge length $3a$. The surface termination is the same for all sizes and also according to fig. 5.3.

5.5.2 Bandstructure

It has been shown in literature [45] that the inverted opal structure provides a full three dimensional bandgap for an index contrast of more than 2.6. This bandgap opens up between the 8th and the 9th band. These values are strictly speaking for the ideal inverted opal without the cylindrical holes connecting the air spheres but the difference is neglectible for our purposes. The example system under consideration has a bandgap

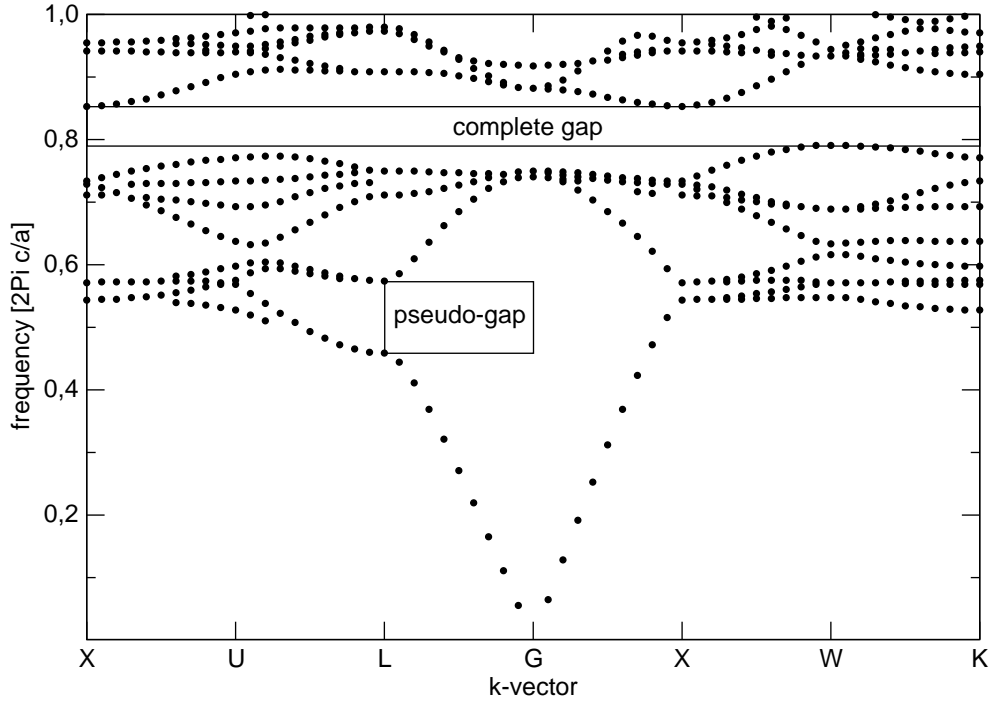


Figure 5.4: Bandstructure for the inverse opal with refractive index $n = 3.6$ and geometrical setup as described in fig. 5.2. The insets show the complete bandgap and the pseudogap in Γ - L -direction.

with a gap/midgap ratio of 6.7% between frequencies 0.795 and 0.85, as can be seen in fig. 5.4. Another remarkable feature of the bandstructure is the large pseudogap in Γ - L -direction. It is remarkable because it corresponds to the (111) crystallographic direction which is in the self-organising fabrication process perpendicular to the crystal surface. Therefore it is easily accessible for reflection experiments and also the preferred direction for the detection of light that is coming out of the crystal. For a detailed discussion of the irreducible BZ and the high symmetry points in k-space see e.g. [46].

5.6 Spontaneous Emission Rate

5.6.1 Space and Polarisation Dependence

As described in 5.3.2 we have to calculate $\Gamma(\omega, \vec{r}_0)$ separately for each emitter position and polarisation. In the finite crystallite moreover not every unit cell is equivalent and differs e.g. in the distance to the surface. However, even if we neglect this and under restriction to the irreducible tetragonal volume this is computationally too expensive to be done for all space points. We will therefore concentrate on selected positions and polarisations that represent interesting physical aspects.

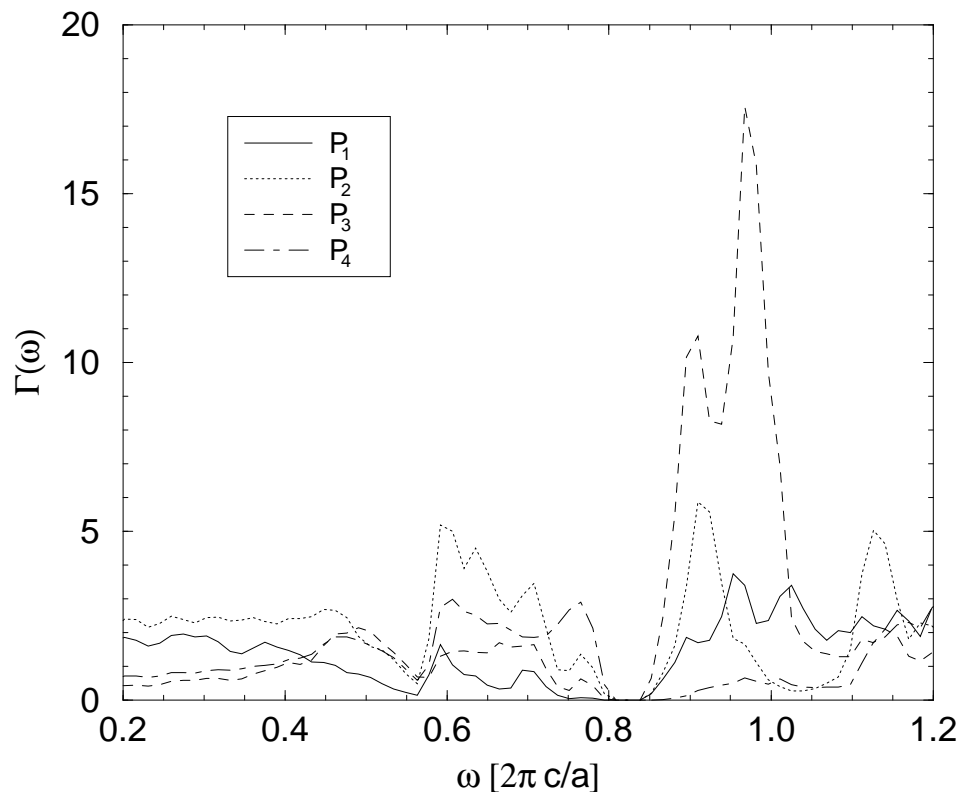


Figure 5.5: $\Gamma(\omega, \vec{r})$ for the high symmetry points $P_1 - P_4$.

First we calculate $\Gamma(\omega, \vec{r}_0)$ at the four high symmetry points within the center unit cell of a $l = 5a$ crystallite (We will justify later why this size is a reasonable choice.) and polarisation in z-direction. In fig. 5.5 we see that the bandgap can be clearly identified for all four symmetry points. Also the directional Γ - L -pseudogap at frequency 0.56 shows its effect at least qualitatively in all cases. However, for other frequencies we see a strong space dependence. Noticable is especially the high enhancement for frequencies

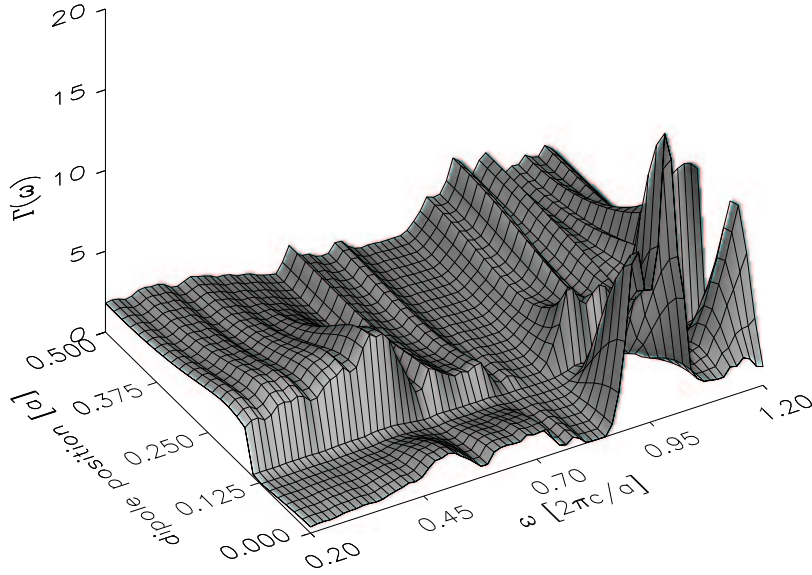


Figure 5.6: $\Gamma(\omega, \vec{r})$ for the path from P_3 to P_1 for a dipole orientated normal to the interface crossed at dipole position $0.15a$.

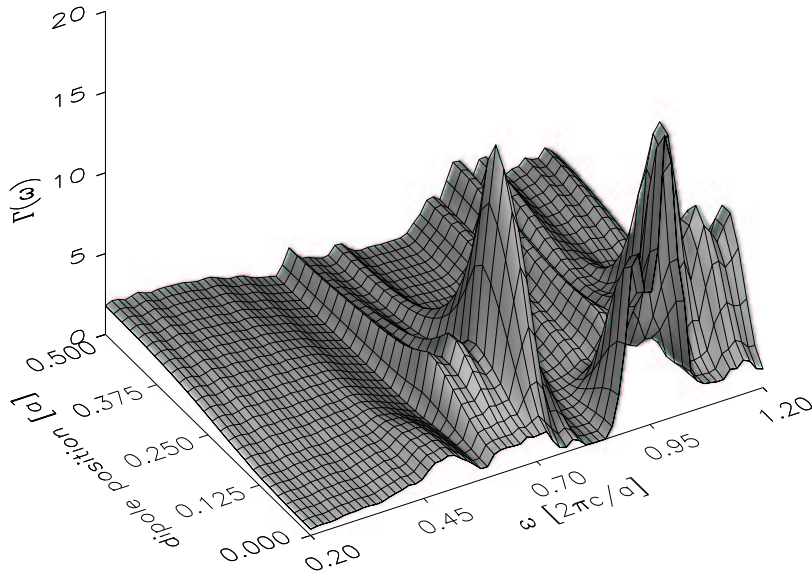


Figure 5.7: $\Gamma(\omega, \vec{r})$ for the path from P_3 to P_1 for a dipole orientated parallel to the interface crossed at dipole position $0.15a$.

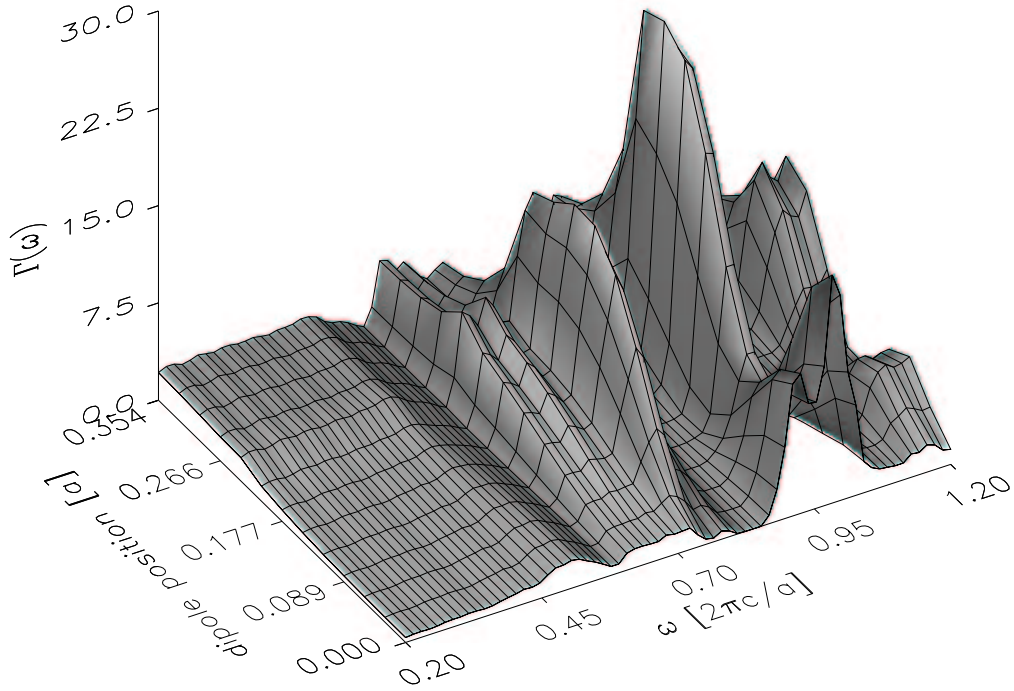


Figure 5.8: $\Gamma(\omega, \vec{r})$ for the path from P_3 to P_2 for a dipole orientated parallel to the interface crossed at dipole position $0.21a$.

just above the bandgap at P_3 with $\Gamma(\omega, \vec{r}_0) \approx 18$. This is not unexpected because many modes tend to concentrate their energy within the high dielectric material and P_3 is in the center of the largest conglomerate of high dielectric material. It should be therefore interesting to investigate what happens if we go from P_3 to another symmetry point, e.g. P_2 , and thereby crossing a dielectric interface. It is obvious that now polarisation has also to be carefully accredited because of the different continuity behaviour for normal and parallel components relative to the interface. We therefore calculate $\Gamma(\omega, \vec{r}_0)$ along the path P_3 - P_2 for perpendicular and parallel polarisation with respect to the dielectric interface crossed at dipole position $0.15a$. For both polarisations the obvious physical features can be clearly identified in fig. 5.6 and fig. 5.7: We have a strong suppression of emission within the bandgap regardless of position. Also the different continuity behaviour at the dielectric interface can be clearly seen. While we have a discontinuous step for normal polarisation in fig. 5.6, Γ is continuous for parallel polarisation in fig. 5.7.

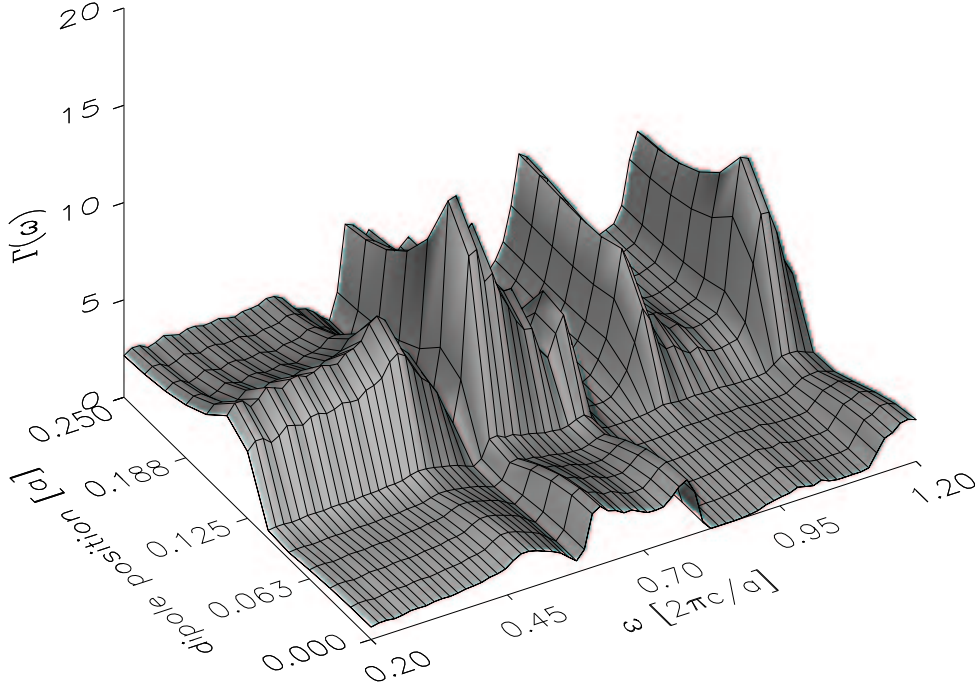


Figure 5.9: $\Gamma(\omega, \vec{r})$ for the path from P_4 to P_2 for a dipole orientated normal to the interface crossed at dipole position $0.14a$.

Moreover, we can see that the enhancement peak for frequencies above the bandgap is spatially localised to the high index octagonal volume independent of polarisation. For the case of parallel polarisation there appears a new enhancement peak below the bandgap for emitters located close to the interface. When we start at P_3 and analyse the path to symmetry point P_2 (that is also lying in air) we see for parallel polarisation a similar picture with high enhancement localised in the octagonal volume but also enhancement peaks for frequencies above as well as below the bandgap at the dielectric interface at dipole position $0.21a$. This can be seen in fig. 5.8. The maximum value for Γ is around 26.

A third possibility of crossing a dielectric interface can be found on the path from P_4 to P_2 . The results for normal dipole polarisation can be found in fig. 5.9. The discontinuous behaviour at the interface can be clearly observed while the maximum enhancement values are not as large as in the other cases. In particular, the enhancement within the

tetragonal volume is much smaller than in the octagonal volume analysed before. From the presented results we can draw two conclusions that are essential for the interpretation of luminescence experiments that are typically done by the infiltration of dye molecules into the inverted opal [12]. First, the strong space dependence of Γ makes the knowledge of the precise distribution of the emitters necessary. Moreover, the strongest effects can be found on dielectric interfaces where the infiltrated dyes will very likely adsorb. Second, the orientation of the adsorbed molecules relative to the interface is also not neglectible. This will especially influence results of experiments done with large dye molecules.

5.6.2 Influence of Finite Size

So far we have analysed the position and polarisation dependence of Γ within the center unit cell. However, as we are dealing with crystallites of finite size, not all unit cells are equivalent.

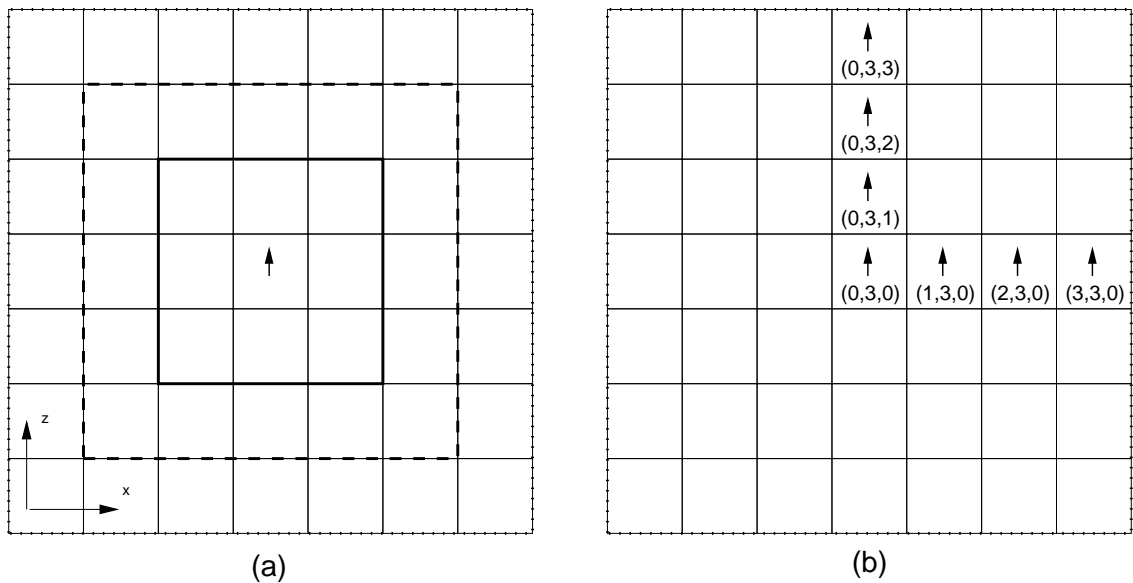


Figure 5.10: Schematic illustration of the finite crystals and dipole positions. One square stands for one conventional unit cell with edge length a . The center unit cell of a crystallite is denoted by $(0,0,0)$ and each unit cell has an integer coordinate in all space directions. (a): Crystals of size $7a$ (dotted), $5a$ (dashed) and $3a$ (solid) with z-polarised dipole in the center unit cell. (b) $y = 3$ plane of the $7a$ crystallite with dipole positions for calculation of surface effects.

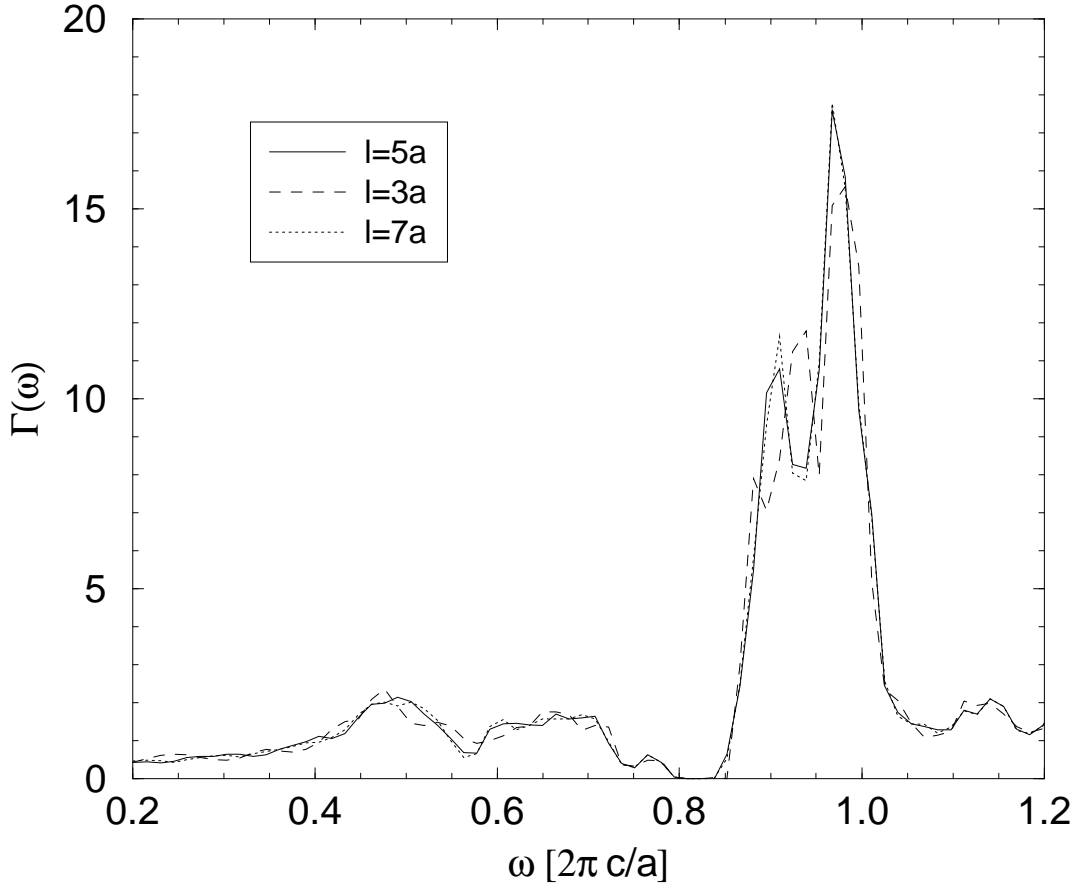


Figure 5.11: $\Gamma(\omega)$ at P_3 for the center unit cell of crystallites with edge length $3a$, $5a$ and $7a$.

We will therefore now study the effects of the absolute size of the crystallite and the proximity of a dipole to the crystallite's surface.

First we calculate Γ at P_3 for the center unit cell of crystallites with size $3a$, $5a$ and $7a$. The geometrical setup is sketched in fig. 5.10 (a). Fig. 5.11 shows that the results are qualitatively the same for $5a$ and $7a$ but differ substantially for $3a$, especially for the enhancement at frequencies between 0.85 and 1.0 where the confinement of the electromagnetic eigenmodes obviously becomes weaker. This result also justifies the choice of a $5a$ crystal in 5.6.1 where we intended to get results that are relatively independent of the finiteness of the system. We should mention here also that the resolution in frequency space is not fine enough to resolve Fabry-Perot interferences that are expected to appear due to the finite size.

In the next calculation we take a $7a$ crystallite and again dipole position P_3 , and move the dipole from the center unit cell closer to the surface. Due to the dipole polarisation

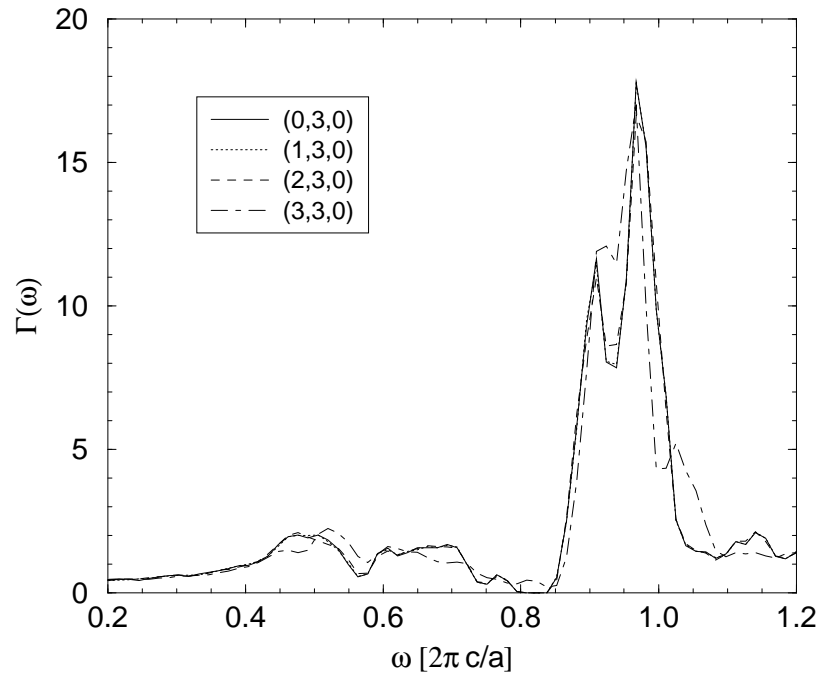


Figure 5.12: $\Gamma(\omega)$ at P_3 for a z-polarised dipole approaching a $x = \text{constant}$ surface.

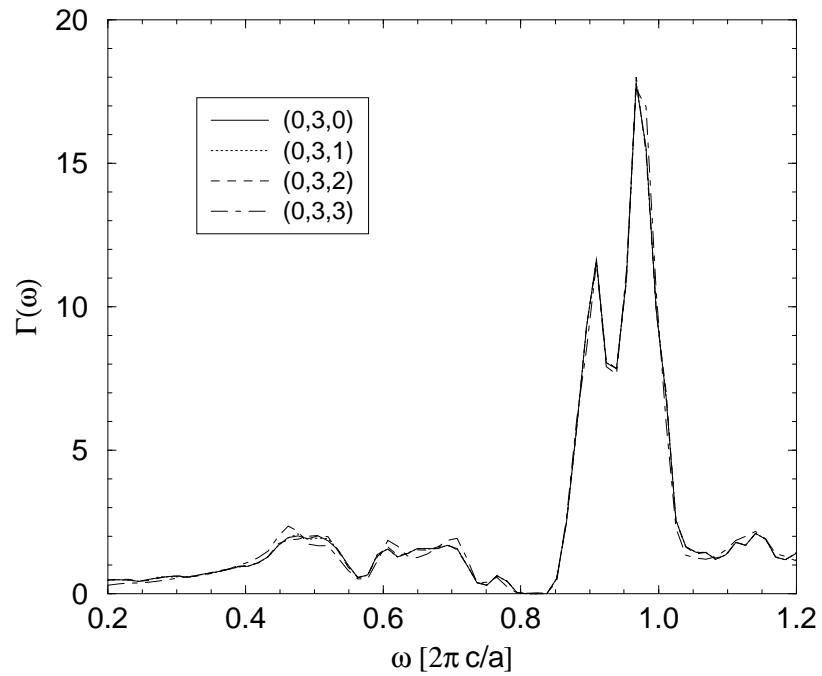


Figure 5.13: $\Gamma(\omega)$ at P_3 for a z-polarised dipole approaching a $z = \text{constant}$ surface.

this can be done in two different ways. If we assume a z -polarised dipole, a shift in x - and y -direction would be equivalent because both surfaces are parallel to the dipole orientation, but a shift in z -direction is physically different, because the dipole is orientated normal to the surface. The geometrical setup is sketched in fig. 5.10 (b). Fig. 5.12 shows Γ for a shift in x -direction. We can see that an effect is only observed for the unit cell directly at the interface and (much weaker) for the next cell. Dipoles lying in the center and the neighboring cells are not effected by the surface.

For a shift in z -direction the influence of the surface is even smaller, as can be seen in fig. 5.13. This can be explained by recalling the emission pattern of a dipole which has a maximum perpendicular to the dipole axis and vanishing components parallel to it. A z -polarised dipole at a $z = \text{constant}$ surface will therefore radiate only a little in direction of the surface.

5.7 Conclusion

This chapter has been devoted to the study of spontaneous emission in inverted opals. The classical approach for obtaining the spontaneous emission rate within the weak coupling regime has been compared with the quantum-mechanical derivation. The numerical FDTD-implementation that builds on this quantum-classical correspondence has been verified by calculating the analytically accessible case of a spherical scatterer showing excellent agreement between the analytical solution and the numerics. The application of the numerical method to finite cuboical cristallites of an inverse opal with refractive index 3.6 lead to the following results:

- The spontaneous emission rate clearly reflects the existence of a bandgap regardless of dipole position.
- Outside the bandgap there is a strong space, polarisation and frequency dependence.
- The strongest enhancement can be observed in the center of the dielectric regions and at dielectric interfaces. The absolute enhancement factor is up to ≈ 26 for the dipole positions under investigation.
- The behaviour at dielectric interfaces shows a polarisation dependence that corresponds to the continuity conditions of the electric field and is therefore strongly varying for perpendicular or parallel polarisation. This result shows the importance of the knowledge of adsorbtion processes of dye molecules in luminescence experiments.
- The finite size of the crystallite has only small influence on the results for dipole positions more than 2-3 lattice constants away from the surface. In other words,

a crystallite with edge length $5a$ represents an "infinite" crystal for an emitter positioned in the center unit cell. This substantially lowers the requirements for experimental analysis.

6 The FDTD-Method and its Application in Photonic Crystal Analysis

6.1 Introduction

All numerical results in this work have been obtained by using several variations of the Finite-Difference Time-Domain algorithm (FDTD) initially presented by Yee in 1966 [48]. The FDTD method represents a very general way of solving the time and space dependent Maxwell's equations using a specialised linearisation scheme. It is used in many fields of electromagnetism and covers the whole range of electro-dynamical problems from nanooptics to accelerator physics. In this chapter we will give a short overview of the basic principles and components of an FDTD simulation as well as discussing in more detail the special modifications needed for analysing photonic crystals. For further reading about FDTD and its applications we suggest e.g. [49] or [50].

6.2 Basic Components and Methods

Very generally speaking, a FDTD-program consists of four fundamental building blocks: First, the spatial definition of the system with a distribution of dielectric or magnetic materials and the choice of a proper termination of the calculation space, the boundary conditions. Second, the core algorithm that calculates the electromagnetic fields at each spatial discretisation point and timestep. Third, an exciting source of some kind and fourth, routines for data extraction, especially when not only the fields but also derived quantities like energy are of interest. The structures of the different building blocks are closely related to each other depending on the problem under consideration. E.g. the use of anisotropic materials requires a special form of the core algorithm, periodic (Bloch) boundaries require complex fields in all other building blocks and so on. In this section we will focus on the components that are needed to obtain the results presented in this work, but there are many variations and extensions also within the field of photonic crystals [51, 52, 53].

6.2.1 The Time-Stepping Algorithm and the Yee-Cell

Our aim is to solve the time dependent curl Maxwell equations:

$$\nabla \times \vec{E}(\vec{r}, t) = -\frac{1}{c} \frac{\partial}{\partial t} \vec{H}(\vec{r}, t) \quad (6.1)$$

$$\nabla \times \vec{H}(\vec{r}, t) = \frac{1}{c} \epsilon(\vec{r}) \frac{\partial}{\partial t} \vec{E}(\vec{r}, t) \quad (6.2)$$

or in vector components:

$$\frac{\partial H_x(\vec{r}, t)}{\partial t} = \frac{\partial E_y(\vec{r}, t)}{\partial z} - \frac{\partial E_z(\vec{r}, t)}{\partial y} \quad (6.3)$$

$$\frac{\partial H_y(\vec{r}, t)}{\partial t} = \frac{\partial E_z(\vec{r}, t)}{\partial x} - \frac{\partial E_x(\vec{r}, t)}{\partial z} \quad (6.4)$$

$$\frac{\partial H_z(\vec{r}, t)}{\partial t} = \frac{\partial E_x(\vec{r}, t)}{\partial y} - \frac{\partial E_y(\vec{r}, t)}{\partial x} \quad (6.5)$$

$$\frac{\partial E_x(\vec{r}, t)}{\partial t} = \frac{1}{\epsilon(\vec{r})} \left(\frac{\partial H_z(\vec{r}, t)}{\partial y} - \frac{\partial H_y(\vec{r}, t)}{\partial z} \right) \quad (6.6)$$

$$\frac{\partial E_y(\vec{r}, t)}{\partial t} = \frac{1}{\epsilon(\vec{r})} \left(\frac{\partial H_x(\vec{r}, t)}{\partial z} - \frac{\partial H_z(\vec{r}, t)}{\partial x} \right) \quad (6.7)$$

$$\frac{\partial E_z(\vec{r}, t)}{\partial t} = \frac{1}{\epsilon(\vec{r})} \left(\frac{\partial H_y(\vec{r}, t)}{\partial x} - \frac{\partial H_x(\vec{r}, t)}{\partial y} \right) \quad (6.8)$$

where the vacuum speed of light c is set to 1 for numerical convenience. The ansatz is now to divide continuous space and time into discrete grid cells and replace spatial and temporal derivatives by finite differences on this discrete mesh. We define the spatial grid as

$$\vec{r} = (x, y, z) \rightarrow (i\Delta x, j\Delta y, k\Delta z) \quad (6.9)$$

for the general three dimensional case and the time dimension as

$$t \rightarrow n\Delta t \quad (6.10)$$

Δx , Δy , Δz and Δt are the discretisation stepwidths and i , j , k and n the integer coordinates within the discrete mesh. The vector components of the fields are therefore denoted as, e.g.

$$H_x(\vec{r}, t) \rightarrow H_x|_{i,j,k}^n \quad (6.11)$$

The next step is the linearisation of the derivatives, following the scheme

$$\frac{\partial f(x = i\Delta x)}{\partial x} \rightarrow \frac{f_{i+1} - f_{i-1}}{2\Delta x} \quad (6.12)$$

By this ansatz, which is used typically in applied mathematics and numerics, the linearisation is effectively done over a $2\Delta x$ -intervall. All components are localised at the same position (i, j, k) in space and will result in e.g. the following update equation for H_x

$$\frac{H_x|_{i,j,k}^{n+1}}{2\Delta t} = \frac{H_x|_{i,j,k}^{n-1}}{2\Delta t} + \frac{E_y|_{i,j,k+1}^n - E_y|_{i,j,k-1}^n}{2\Delta z} - \frac{E_z|_{i,j+1,k}^n - E_z|_{i,j-1,k}^n}{2\Delta y} \quad (6.13)$$

The revolutionary idea of Yee was now to take advantage of the special nature of Maxwell's curl equations to improve accuracy by a factor of two by changing the spatial localisation of the field components in the following way:

$$E_x [i\Delta x, j\Delta y, k\Delta z] \rightarrow E_x \left[\left(i + \frac{1}{2}\right)\Delta x, j\Delta y, k\Delta z \right] \quad (6.14)$$

$$E_y [i\Delta x, j\Delta y, k\Delta z] \rightarrow E_y \left[i\Delta x, \left(j + \frac{1}{2}\right)\Delta y, k\Delta z \right] \quad (6.15)$$

$$E_z [i\Delta x, j\Delta y, k\Delta z] \rightarrow E_z \left[i\Delta x, j\Delta y, \left(k + \frac{1}{2}\right)\Delta z \right] \quad (6.16)$$

$$H_x [i\Delta x, j\Delta y, k\Delta z] \rightarrow H_x \left[i\Delta x, \left(j + \frac{1}{2}\right)\Delta y, \left(k + \frac{1}{2}\right)\Delta z \right] \quad (6.17)$$

$$H_y [i\Delta x, j\Delta y, k\Delta z] \rightarrow H_y \left[\left(i + \frac{1}{2}\right)\Delta x, j\Delta y, \left(k + \frac{1}{2}\right)\Delta z \right] \quad (6.18)$$

$$H_z [i\Delta x, j\Delta y, k\Delta z] \rightarrow H_z \left[\left(i + \frac{1}{2}\right)\Delta x, \left(j + \frac{1}{2}\right)\Delta y, k\Delta z \right] \quad (6.19)$$

In the curl expressions this means that the neighboring components that are needed to calculate the derivative are only 0.5 steps away and the linearisation is only done over a one step interval. As E-fields only depend on H-fields and vice versa, the same can be done in time, shifting E-fields $0.5\Delta t$ relative to the H-fields. The resulting equations are therefore

$$\frac{H_x|_{i,j+\frac{1}{2},k+\frac{1}{2}}^{n+\frac{1}{2}}}{\Delta t} = \frac{H_x|_{i,j+\frac{1}{2},k+\frac{1}{2}}^{n-\frac{1}{2}}}{\Delta t} + \frac{E_y|_{i,j+\frac{1}{2},k+1}^n - E_y|_{i,j+\frac{1}{2},k}^n}{\Delta z} - \frac{E_z|_{i,j+1,k+\frac{1}{2}}^n - E_z|_{i,j,k+\frac{1}{2}}^n}{\Delta y} \quad (6.20)$$

$$\frac{H_y|_{i+\frac{1}{2},j,k+\frac{1}{2}}^{n+\frac{1}{2}}}{\Delta t} = \frac{H_y|_{i+\frac{1}{2},j,k+\frac{1}{2}}^{n-\frac{1}{2}}}{\Delta t} + \frac{E_z|_{i+1,j,k+\frac{1}{2}}^n - E_z|_{i,j,k+\frac{1}{2}}^n}{\Delta x} - \frac{E_x|_{i+\frac{1}{2},j+1,k}^n - E_x|_{i+\frac{1}{2},j,k}^n}{\Delta z} \quad (6.21)$$

$$\frac{H_z|_{i,j+\frac{1}{2},k+\frac{1}{2}}^{n+\frac{1}{2}}}{\Delta t} = \frac{H_z|_{i,j+\frac{1}{2},k+\frac{1}{2}}^{n-\frac{1}{2}}}{\Delta t} + \frac{E_x|_{i+\frac{1}{2},j+1,k}^n - E_x|_{i+\frac{1}{2},j,k}^n}{\Delta y} - \frac{E_y|_{i+1,j+\frac{1}{2},k}^n - E_y|_{i,j+\frac{1}{2},k}^n}{\Delta x} \quad (6.22)$$

for the H-field components and

$$\frac{E_x|_{i+\frac{1}{2},j,k}^n}{\Delta t} = \frac{E_x|_{i+\frac{1}{2},j,k}^{n-1}}{\Delta t} + \frac{1}{\epsilon|_{i+\frac{1}{2},j,k}} \cdot \left[\frac{H_z|_{i+\frac{1}{2},j+\frac{1}{2},k}^{n+\frac{1}{2}} - H_z|_{i+\frac{1}{2},j-\frac{1}{2},k}^{n+\frac{1}{2}}}{\Delta y} - \frac{H_y|_{i+\frac{1}{2},j,k+\frac{1}{2}}^{n+\frac{1}{2}} - H_y|_{i+\frac{1}{2},j,k-\frac{1}{2}}^{n+\frac{1}{2}}}{\Delta z} \right] \quad (6.23)$$

$$\frac{E_y|_{i,j+\frac{1}{2},k}^n}{\Delta t} = \frac{E_y|_{i,j+\frac{1}{2},k}^{n-1}}{\Delta t} + \frac{1}{\epsilon|_{i,j+\frac{1}{2},k}} \cdot \left[\frac{H_x|_{i,j+\frac{1}{2},k+\frac{1}{2}}^{n+\frac{1}{2}} - H_x|_{i,j+\frac{1}{2},k-\frac{1}{2}}^{n+\frac{1}{2}}}{\Delta z} - \frac{H_z|_{i+\frac{1}{2},j+\frac{1}{2},k}^{n+\frac{1}{2}} - H_z|_{i-\frac{1}{2},j+\frac{1}{2},k}^{n+\frac{1}{2}}}{\Delta x} \right] \quad (6.24)$$

$$\frac{E_z|_{i,j,k+\frac{1}{2}}^n}{\Delta t} = \frac{E_z|_{i,j,k+\frac{1}{2}}^{n-1}}{\Delta t} + \frac{1}{\epsilon|_{i,j,k+\frac{1}{2}}} \cdot \left[\frac{H_y|_{i+\frac{1}{2},j,k+\frac{1}{2}}^{n+\frac{1}{2}} - H_y|_{i-\frac{1}{2},j,k+\frac{1}{2}}^{n+\frac{1}{2}}}{\Delta x} - \frac{H_x|_{i,j+\frac{1}{2},k+\frac{1}{2}}^{n+\frac{1}{2}} - H_x|_{i,j-\frac{1}{2},k+\frac{1}{2}}^{n+\frac{1}{2}}}{\Delta y} \right] \quad (6.25)$$

for the E-field components. This procedure yields a one order higher accuracy in space

and time without increasing the total number of discretisation points. The arrangement of the shifted grids for each component is illustrated in fig. 6.1.

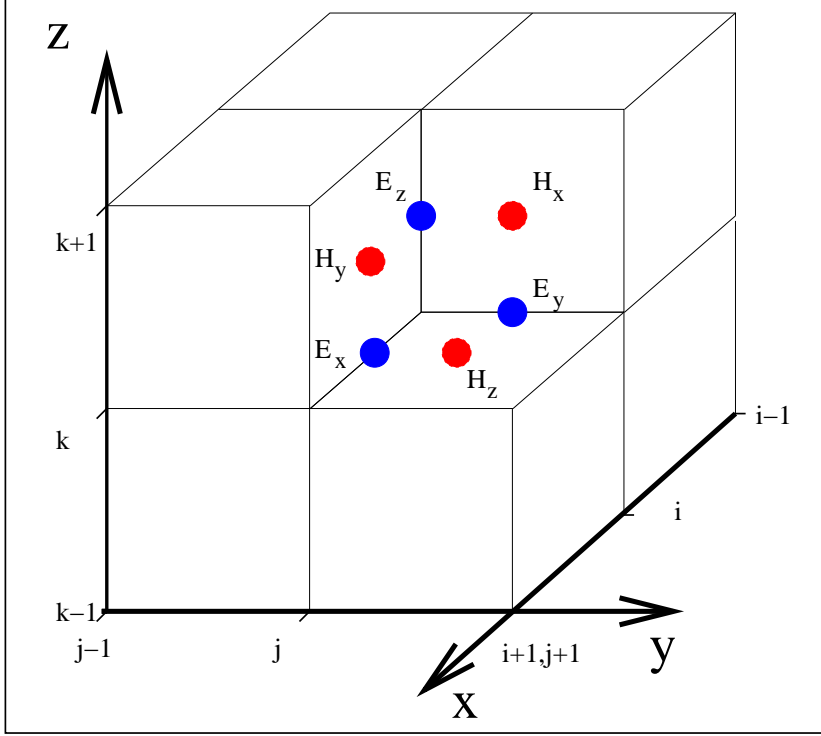


Figure 6.1: Illustration of the spatial localisation of the field components in a three dimensional Yee cell.

The field values at a new time step only depend on former values of other fields as can be seen in eq. 6.20-6.25. In applied mathematics this is called an explicit scheme and is well known to be unstable in general. However, in the case of Maxwell's curl equations we can force stability by obeying the condition

$$\Delta t \leq \frac{1}{c \sqrt{\left(\frac{1}{\Delta x}\right)^2 + \left(\frac{1}{\Delta y}\right)^2 + \left(\frac{1}{\Delta z}\right)^2}} \quad (6.26)$$

for the discrete step widths in space and time. The derivation is not given here in detail and can be studied in [49]. Principally, it is done by analysing the influence of the discretisation on the error of the energy content of a plane wave, assuring that the energy does not increase in time in average.

The accuracy of the discrete numerical scheme depends mainly on the discrete space and time steps. As a rule of thumb the smallest wavelength appearing in the calculations should be at least resolved with 12 numerical grid points.

6.2.2 Boundary Conditions

It is obvious that in practical calculations only a finite number of discretisation points and therefore a finite space volume (and time interval) can be calculated. The consequence is that the discrete curl equations can not be applied for certain field components at the edges of the computational domain because some of the required components would lie outside and are therefore not defined. If we look e.g. in x-direction and a domain bounded by $i = 0$ and $i = i_{max}$ we see that equations 6.20, 6.21 and 6.22 and 6.23 are still valid because they only require well defined field values for $i = 0$. However, in equations 6.24 and 6.25 the components

$$H_z|_{-\frac{1}{2},j+\frac{1}{2},k}^{n+\frac{1}{2}}$$

and

$$H_y|_{-\frac{1}{2},j,k+\frac{1}{2}}^{n+\frac{1}{2}}$$

are required but not defined.

The situation at $i = i_{max}$ is similar. Now we need the undefined values

$$E_z|_{i_{max}+1,j,k+\frac{1}{2}}^n$$

for updating H_y and

$$E_y|_{i_{max}+1,j+\frac{1}{2},k}^n$$

for H_z .

If we generalise this consideration, we have to take special care of the tangential components of the electric field at the interfaces $i, j, k = 0$ and $i, j, k = (i, j, k)_{max} + 1$ to obtain a completely defined system. In the next subsections, typical boundary conditions used for the calculations in this work are shortly described.

Metallic Boundaries

The simplest way of treating the tangential electric field components is to set them to zero after each time step. Mathematically this corresponds to the von Neumann-boundary condition of a constant potential at the interface and physically it describes a perfectly conducting material which is approximated best in experiment by metals. Therefore we speak of metallic boundary conditions. An incoming electromagnetic wave

that hits the boundary is entirely reflected back into the computational domain and no energy can escape from the system. This type of boundary does not represent the desired circumstances for most calculations. However, because of its easy implementation it is sometimes used in combination with other methods as will be described later.

Periodic Boundaries

For perfectly periodic systems (which means they are infinitely extended in the direction(s) of periodicity) we know from Bloch's theorem (see 3.1.2) that the field values at equivalent positions in different unit cells only differ by a phase factor. Numerically this has the consequence that we can describe the entire infinite system by just one unit cell and apply periodic boundaries that fulfill Bloch's theorem. We illustrate this for a one dimensional system extending in x-direction and bounded by $i = 0$ and $i = i_{max}$. We know from the introduction of this section that we have to take special care of $E_y|_{i=0}$, $E_y|_{i=i_{max}+1}$, $E_z|_{i=0}$ and $E_z|_{i=i_{max}+1}$. If we assume a periodicity of length $i_{max}\Delta x$ we can relate the components at the boundaries by applying Bloch's theorem in the following way:

$$E_y|_{i=0} = e^{+ik_x i_{max}\Delta x} \cdot E_y|_{i=i_{max}} \quad (6.27)$$

$$E_z|_{i=0} = e^{+ik_x i_{max}\Delta x} \cdot E_z|_{i=i_{max}} \quad (6.28)$$

$$E_y|_{i=i_{max}+1} = e^{-ik_x i_{max}\Delta x} \cdot E_y|_{i=1} \quad (6.29)$$

$$E_z|_{i=i_{max}+1} = e^{-ik_x i_{max}\Delta x} \cdot E_z|_{i=1} \quad (6.30)$$

For the application of Bloch's theorem we have to introduce a wavevector k_x in the direction of periodicity. This is a parameter in the calculation and has to be given from the outside. The restriction to only one k-value is the price one has to pay for the benefit of limiting the computational domain to just one unit cell. Moreover, the phase factor in Bloch's theorem is complex, requiring complex electric and magnetic fields also. In practice this doubles the memory requirements of the calculation. The generalisation to three dimensions is straightforward but requires a \vec{k} -vector with components in all space directions.

Open Boundaries

In many cases it is desirable to simulate a structure embedded in infinitely extended free space because this is closest to most experimental situations. Numerically this means we have to define boundary conditions with the property that waves approaching the interfaces of the computational domain are completely absorbed without any spurious reflection back into the system. This has to be achieved for waves of arbitrary frequency and angle of incidence. There are several propositions in literature for addressing this

task like Mur's boundary conditions [54] of first and second order or perfectly matched layers (PML) invented by Berenger [55] in several variations. In this work we use the so-called uniaxial perfectly matched layers (UPML) boundary [49] and will now give a short description of their fundamentals and practical implementation.

The idea of PML boundaries is simple: We introduce a layer of a certain thickness d (in units of numerical discretisation points) consisting of an artificial conducting material that absorbs incoming waves. The absorbing layer is terminated by metallic boundaries that reflect the rests of the wave entirely and the wave is damped again on its way back. Only a vanishing part of the original amplitude reenters the calculation domain. The obvious difficulty that has to be solved is that for conventional absorbing materials there would be a partial reflection at the interface between the calculation volume and the absorbing material due to impedance mismatch. We have to choose the material properties therefore in a way that there is no impedance discontinuity for any frequency and angle of incidence. It has been shown in [49] that this condition can be fulfilled for a plane wave with frequency ω by the modified frequency domain Maxwell's equations

$$\nabla \times \vec{H}(\vec{r}, \omega) = -i\omega\epsilon(\vec{r}) \underline{\underline{s}} \cdot \vec{E}(\vec{r}, \omega) \quad (6.31)$$

$$\nabla \times \vec{E}(\vec{r}, \omega) = i\omega\mu(\vec{r}) \underline{\underline{s}} \cdot \vec{H}(\vec{r}, \omega) \quad (6.32)$$

with a matrix $\underline{\underline{s}}$ of the form

$$\underline{\underline{s}} = \begin{pmatrix} \frac{s_y s_z}{s_x} & 0 & 0 \\ 0 & \frac{s_x s_z}{s_y} & 0 \\ 0 & 0 & \frac{s_x s_y}{s_z} \end{pmatrix} \quad (6.33)$$

where the components of the diagonal elements are given by

$$s_i = \kappa_i - \frac{\sigma_i}{i\omega} \quad (6.34)$$

The parameter σ_i is responsible for the damping of a wave with a k_i component of the wavevector while κ_i ensures the correct treatment of evanescent waves reaching into the PML layer. In a three dimensional volume we have six PML-layers (two for each dimension). Due to the finite thickness of the PML layers we have regions at edges where two PML layers overlap and corners where three PML layers overlap. This is shown schematically in fig. 6.2 . Depending on the region under consideration the matrix $\underline{\underline{s}}$ can be simplified because the s_i are only different from 1 for the components normal to the interface. This means we only need the general form of $\underline{\underline{s}}$ in the corners, while for areas where e.g. there is only a damping in x-direction $\underline{\underline{s}}$ reduces to

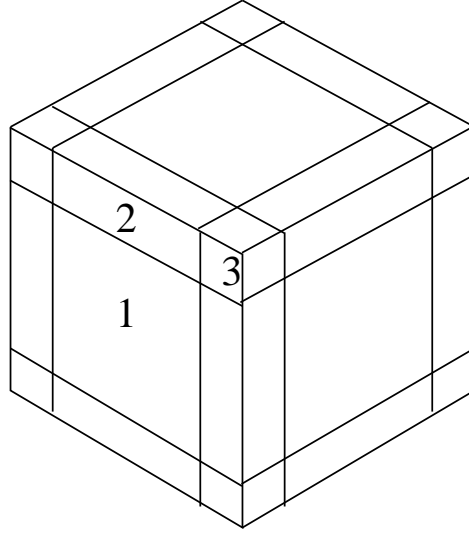


Figure 6.2: Schematic illustration of different PML-regions. (1): Plane, (2): Edge and (3): Corner

$$\underline{\underline{s}} = \begin{pmatrix} \frac{1}{s_x} & 0 & 0 \\ 0 & s_x & 0 \\ 0 & 0 & s_x \end{pmatrix} \quad (6.35)$$

Now we want to apply this concept in our FDTD algorithm. The first problem is that a direct fourier transformation of the frequency domain expressions would lead to a convolution in time. To circumvent this problem the additional fields \vec{B} and \vec{D} are introduced, leading to the following set of modified Maxwell's equations for the PML layers:

$$\nabla \times \vec{H}(\vec{r}, t) = \vec{\kappa} \cdot \frac{\partial \vec{D}(\vec{r}, t)}{\partial t} + \vec{\sigma} \cdot \vec{D}(\vec{r}, t) \quad (6.36)$$

$$\nabla \times \vec{E}(\vec{r}, t) = - \vec{\kappa} \cdot \frac{\partial \vec{B}(\vec{r}, t)}{\partial t} - \vec{\sigma} \cdot \vec{B}(\vec{r}, t) \quad (6.37)$$

$$\vec{\kappa} \cdot \frac{\partial \vec{D}(\vec{r}, t)}{\partial t} + \vec{\sigma} \vec{D}(\vec{r}, t) = \epsilon(\vec{r}) \left(\vec{\kappa} \frac{\partial \vec{E}(\vec{r}, t)}{\partial t} + \vec{\sigma} \cdot \vec{E}(\vec{r}, t) \right) \quad (6.38)$$

$$\vec{\kappa} \cdot \frac{\partial \vec{B}(\vec{r}, t)}{\partial t} + \vec{\sigma} \vec{B}(\vec{r}, t) = \epsilon(\vec{r}) \left(\vec{\kappa} \frac{\partial \vec{H}(\vec{r}, t)}{\partial t} + \vec{\sigma} \cdot \vec{H}(\vec{r}, t) \right) \quad (6.39)$$

The discretisation follows the standard FDTD scheme with \vec{D} localised at the same positions as \vec{E} and \vec{B} at the same positions as \vec{H} .

The last issues to consider are now the values for σ_i and κ_i . This has been the subject of many numerical experiments and studies. By a proper choice the performance of the PML boundaries can be optimised e.g. for certain frequency ranges or angles of incidence. Without a more detailed discussion we give now the expressions for $\sigma_i(i)$ and $\kappa_i(i)$ chosen for the photonic crystal calculations in this work which are spatially dependant of the direction perpendicular to the layers:

$$\sigma_i(i) = \sigma_{max} \cdot \left(\frac{i}{d}\right)^p \quad (6.40)$$

$$\kappa_i(i) = 1 + (\kappa_{max} - 1) \cdot \left(\frac{i}{d}\right)^p \quad (6.41)$$

where d is the total thickness of the PML layers and p an exponent that is usually between 3 and 4 [49]. For the calculations in this work d is normally between 8 and 20 discretisation points.

6.2.3 Sources

To calculate the optical response of a dielectric structure we obviously need some kind of excitation. The choice of a proper excitation for a given problem does not follow a general guideline but strongly depends on experience. In many cases, the expected results play an important role for the choice of the excitation. E.g. the symmetry or spatial localisation of the expected solutions can help to selectively excite the desired field distributions. This does not mean that FDTD is not an a-priori-method. However, its general character is one major disadvantage in this respect. A solution obtained by FDTD is always reliable. However, under circumstances to be discussed more detailed later on a solution can be "forgotten" due to an awkward excitation, which often means it is superposed by solutions that are excited orders of magnitude stronger. In this subsection we will discuss several types of excitations. The explicit forms how they are used in practice are given directly in the related chapters of photonic crystal applications later on.

Initial Fields

A method used quite often is the assignment of the field to certain values for $t = n\Delta t = 0$. When this type of excitation is used one has to take care of the following issues: The initial field distribution must fulfill the homogenous Maxwell's equations that are not directly incorporated in the FDTD-algorithm. Especially the condition

$$\nabla \vec{H}(\vec{r}, t = 0) = 0 \quad (6.42)$$

must be fulfilled because a violation would lead to unphysical results. A violation of

$$\nabla \left[\epsilon(\vec{r}) \vec{E}(\vec{r}, t = 0) \right] = 0 \quad (6.43)$$

would physically introduce static charges that may also modify the results.

Beside this physical considerations, there are also numerical ones that can influence the simulations. The initial condition will project to the solutions allowed by the system. This process takes some "relaxation" time. The proper choice of the initial condition can reduce this time significantly and thereby also reducing numerical noise. We will illustrate this now for a simple example.

Assume a one dimensional freespace ($n = 1.0$) system bounded by periodic boundaries with k-vector k_x . This system supports plane wave solutions with the spatial distribution

$$E_y(x) = E_y^0 e^{i(k_x + G_i)x} \quad (6.44)$$

where G_i are reciprocal lattice vectors as defined in 3.1.2. If we now set an initial field

$$E_y(x) = \sum_i E_y^0 e^{i(k_x + G_i)x} \quad (6.45)$$

for some reciprocal lattice vectors G_i the initial condition will instantaneously fit to the boundary conditions and i plane waves will propagate in time through the system without being disturbed.

Now we choose an initial condition of the same form but with a slightly different vector $k'_x = k_x + \delta k_x$ but keep k_x as the parameter of the periodic boundaries. In this case the values that are exchanged by the periodic boundaries do not fit and plane waves with the same k_x but slightly different phase enter the system. After some time the system consists of many plane waves that are all slightly phase shifted. The result is a destructive interference and no proper solutions are excited. Moreover, due to the approximative character of the discrete system the cancellation is not perfect, but will cause a random noise. Even if we have a mixture of fitting and non-fitting components of the initial condition this noise can superpose the real solutions and make them undetectable.

If we look at the frequency spectrum of the initial field excitation we see that due to the δ -like shape in time we can expect that all frequency components could principally be excited. Sometimes this is desirable, especially when all solutions are expected to have similar coupling strengths (or spatial overlap) to the excitation and a large spectrum of solutions is wanted. However, there are also cases when this property is a disadvantage, especially when solutions are investigated that couple only weakly to external excitations. Then a pulsed excitation with a narrow frequency spectrum around the expected solution should be preferred.

Current Sources

A very simple way of creating electromagnetic fields is the introduction of a pointlike oscillating current source at position \vec{r}_0 into the H-field curl equation:

$$\nabla \times \vec{H}(\vec{r}_0, t) = \epsilon(\vec{r}) \frac{\partial \vec{E}(\vec{r}_0, t)}{\partial t} + \delta(\vec{r} - \vec{r}_0) \cdot \vec{j}(t) \quad (6.46)$$

This is practically done by keeping the time-stepping algorithm unchanged and updating the corresponding electric field components after each timestep according to

$$E_x|_{i_0+\frac{1}{2},j_0,k_0}^n = E_x|_{i_0+\frac{1}{2},j_0,k_0}^{n-1} + \epsilon^{-1}|_{i_0+\frac{1}{2},j_0,k_0} \cdot j_x|_{i_0+\frac{1}{2},j_0,k_0}^n \quad (6.47)$$

e.g. for a x-polarised dipole with arbitrary temporal dependance $j_x|_x^n$. It should be mentioned that an arbitrary orientation of one pointsource is not straightforward to implement because of the different localisation of the E-field vector components.

In most cases dipoles instead of initial fields are used when only an excitation of a limited frequency spectrum is desired. A proper choice for $\vec{j}(\vec{r}_0, t)$ is then e.g. a sinusoidal function with center frequency ω_0 multiplied with a Gaussian envelope of width σ .

$$\vec{j}(\vec{r}_0, t) = \delta(\vec{r} - \vec{r}_0) \cdot \vec{j}_0 \sin(\omega_0 t) e^{-\frac{1}{2} \cdot \left(\frac{t-t_0}{\sigma}\right)^2} \quad (6.48)$$

where the spectral width of the pulse around ω_0 is determined by σ^{-1} . The radiation characteristics of a dipole are well known [56]. It should be taken care that this is considered for a proper excitation. E.g. a x-polarised dipole has no plane wave component directly pointing into x-direction and therefore maybe no good choice when a mode propagating in x-direction should be excited.

When it is desired to excite a field pattern of a certain symmetry there are two issues to be considered.

First, the spatial localisation of the excitation due to the spatial shift of the corresponding E-field component. It has been observed that even the small $0.5\Delta x$ -shift can significantly break the symmetry when not properly considered.

Second, when choosing two dipoles to excite odd or even mirror symmetry the transformation behaviour is different for dipoles polarised perpendicular or tangential to the mirror plane according to the discussion in 3.1.5.

One more issue of practical importance is the choice of t_0 in the envelope function. It should be assured that the current for $t = 0$ is small compared to the maximum amplitude because otherwise we have physically a step function at the beginning that can disturb results, especially after Fourier transforming by introducing Gibb's oscillations. It is also important to be aware that a point-source of the described type can introduce static charges after the temporal oscillation vanished. This can be seen in the continuity

equation for charges and currents

$$\frac{\partial}{\partial t}\rho(\vec{r}, t) + \nabla \cdot \vec{j}(\vec{r}, t) = 0 \quad (6.49)$$

If we integrate 6.49 from $t = 0$ to $t = T$ and assume that we had no static charges at the beginning of the calculation we get

$$\rho(\vec{r}, T) = - \int_0^T \nabla \cdot \vec{j}(\vec{r}, t) dt \quad (6.50)$$

To avoid static charges we can therefore choose a current distribution that has either no divergence, or that is zero when integrated in time. In practice, the second condition can be easily fulfilled by adjusting the phase of the sine function

$$\vec{j}(\vec{r}_0, t) = \delta(\vec{r} - \vec{r}_0) \cdot \vec{j}_0 \sin[\omega_0(t - t_0)] e^{-\frac{1}{2} \left(\frac{t-t_0}{\sigma}\right)^2} \quad (6.51)$$

because now we integrate over the product of a sine function that is odd with respect to t_0 with a Gaussian that is even with respect to t_0 .

Total-Field/Scattered-Field Method

The injection of external fields by electric dipole currents has the disadvantage that the radiation pattern of a dipole is given and therefore there is no choice of certain plane wave components exciting the system. This can be overcome e.g. by using lines or planes of dipoles that are arranged in a way that the plane wave components travelling in undesired directions cancel each other. This method is used widely because of its easy implementation. Nevertheless it has the disadvantage that e.g. for a plane of dipoles, energy is radiated in both directions away from the plane. In cases where reflection properties of a structure are investigated the waves travelling in the wrong direction away from the source plane can overlap with waves reflected by the dielectric structure and therefore influence results. This can be overcome for pulsed sources by choosing a long path between the incoupling plane and the structure. This allows the temporal separation of the different parts but requires a lot of additional system size and therefore computing resources (time and memory). A better way of injecting well defined plane wave components is the total-field/scattered-field (TFSF) method that is more complicated but more powerful and efficient. We will now describe TFSF for a simple one dimensional example.

Due to the superposition principle for electric and magnetic fields we can assume arbitrarily that the total fields are splitted in scattered parts \vec{E}_{scat} and \vec{H}_{scat} , and incident parts \vec{E}_{inc} and \vec{H}_{inc} :

$$\vec{E}_{total}(x, t) = \vec{E}_{scat}(x, t) + \vec{E}_{inc}(x, t) \quad (6.52)$$

$$\vec{H}_{total}(x, t) = \vec{H}_{scat}(x, t) + \vec{H}_{inc}(x, t) \quad (6.53)$$

Moreover, we can also arbitrarily define a certain position $x_0 = i_0\Delta x$ and demand that for $x < x_0$ only the scattered parts are considered while for $x \geq x_0$ the total fields are calculated. For the discrete FDTD equations this is consistent for most space points but not at the border i_0 where we have e.g.

$$E_{y,total}|_{i_0}^{n+1} = E_{y,total}|_{i_0}^n + \epsilon(i_0)^{-1} \frac{\Delta t}{\Delta x} \left(H_{z,scat}|_{i_0-\frac{1}{2}}^{n+\frac{1}{2}} - H_{z,tot}|_{i_0+\frac{1}{2}}^{n+\frac{1}{2}} \right) \quad (6.54)$$

with the finite difference of a total and a scattered part of the magnetic field that violates our assumptions. However, we can correct 6.54 by adding an external incident part:

$$\begin{aligned} E_{y,total}|_{i_0}^{n+1} &= E_{y,total}|_{i_0}^n + \epsilon(i_0)^{-1} \frac{\Delta t}{\Delta x} \left(H_{z,scat}|_{i_0-\frac{1}{2}}^{n+\frac{1}{2}} - H_{z,tot}|_{i_0+\frac{1}{2}}^{n+\frac{1}{2}} \right) \\ &\quad + \epsilon(i_0)^{-1} \frac{\Delta t}{\Delta x} \cdot H_{z,inc}|_{i_0-\frac{1}{2}}^{n+\frac{1}{2}} \\ &= E_{y,total}|_{i_0}^n + \epsilon(i_0)^{-1} \frac{\Delta t}{\Delta x} \left(H_{z,tot}|_{i_0-\frac{1}{2}}^{n+\frac{1}{2}} - H_{z,tot}|_{i_0+\frac{1}{2}}^{n+\frac{1}{2}} \right) \end{aligned}$$

The incident part $H_{z,inc}|_{i_0-\frac{1}{2}}^{n+\frac{1}{2}}$ can now be defined arbitrarily. Together with the analogous equations for the other tangential components E_z , H_y and H_z we can inject external fields at i_0 . E.g. we can assume the temporal characteristics of a plane wave and assign them to $E_{y,inc}$ and $H_{z,inc}$ and a wavevector in $+x$ -direction. The result would be a wave travelling into $+x$ -direction, starting at i_0 . For $x < x_0$ there would be no fields until a reflection occurs somewhere at $x \geq x_0$. The reflected parts of the wave cross i_0 unperturbed and represent the scattered part.

If we extend this principle to two dimensions we have to define the tangential components along a line. However, we have to take care at the end of the line depending on the boundary conditions used. In fig. 6.3 (a) we illustrate the case of a periodic boundary in the direction parallel to the incoupling line. As Bloch's theorem exactly relates the space points at the ends we can inject plane waves that need not necessarily propagate perpendicular to the incoupling line without further concerns. If we have absorbing boundaries we cannot just end the injection line because for the ends there would be inconsistent FDTD-equations. Instead we have to define a closed line as seen in fig. 6.3 (b) to ensure consistency. This method requires the complete knowledge of the temporal and spatial characteristics of the excitation at all injection lines and

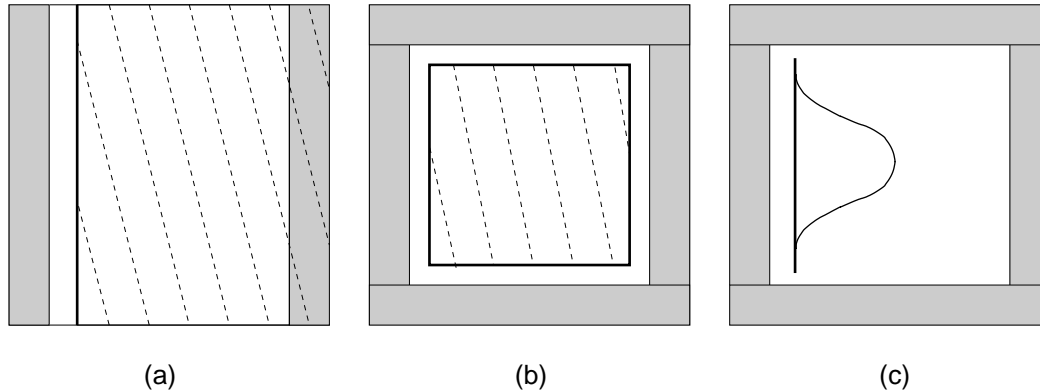


Figure 6.3: Different types of TFSSF-injections in 2D depending on the type of boundary conditions. The bold line represents the TFSSF-injection line, dashed lines phase fronts of incoupled plane waves and grey regions absorbing boundaries. The remaining boundaries in (a) are periodic.

is therefore often very complicated to implement. Also, one has to be very careful when interpreting the physical meaning of the fields inside and outside the closed line, when a complicated scattering occurs inside. An approximation used to circumvent this problem is to abandon the precise plane wave injection in favor of a spatially localised excitation as sketched in fig. 6.3 (c). In this case a spatial envelope function assures that the incident fields vanish at the ends of the injection line and therefore we do not need a closed line. Unfortunately, this spatially localised excitation has also plane wave components parallel to the incoupling line that cannot be injected properly by TFSSF. There is always an error in the order of a few percent, depending on the strength of these parallel plane wave components that does not only appear as a distorted field inside the calculation space but also as unwanted waves travelling away from the incoupling line in the wrong direction. The extension of the described two dimensional scheme to three dimensions is straightforward.

6.2.4 Data Extraction

The FDTD code principally provides all vector components of electric and magnetic fields for the whole integration space and time. However, in many cases the time and space dependant fields are not the relevant quantities to draw physical conclusions. Then we need derived or transformed quantities, e.g. energy or energy transportation information as well as fourier transforms. To obtain this information consistently within the FDTD-algorithm we have to properly include the effects of discretisation and shifted grids.

Poynting's Theorem

The energy in a space volume V with a dielectric structure $\epsilon(\vec{r})$ at a time t_0 follows a conservation equation known as Poynting's theorem:

$$\begin{aligned}
 & \int_V dr^3 \vec{j}(\vec{r}, t_0) \cdot \vec{E}(\vec{r}, t_0) \\
 & + \int_{\Omega(V)} dr^2 \left[\vec{E}(\vec{r}, t_0) \times \vec{H}(\vec{r}, t_0) \right] \\
 & - \int_V dr^3 \frac{1}{2} \left[\epsilon(\vec{r}) \vec{E}^2(\vec{r}, t_0) + \vec{H}^2(\vec{r}, t_0) \right] = 0
 \end{aligned} \tag{6.55}$$

The first term represents the energy that is created within the volume when the electric field $\vec{E}(\vec{r}, t)$ interacts with a current $\vec{j}(\vec{r}, t_0)$. The second term integrates the energy flow represented by the Poynting vector

$$\vec{S}(\vec{r}, t_0) = \vec{E}(\vec{r}, t_0) \times \vec{H}(\vec{r}, t_0) \tag{6.56}$$

over the surface $\Omega(V)$ and therefore stands for the energy leaving or entering the system. The third term finally represents the total electromagnetic energy stored within the volume.

Especially for transmission or reflection calculations the knowledge of energy related quantities is very important. However, obviously, we have a problem when we want to transfer eq. 6.55 to the discrete grid of an FDTD-calculation because the different field vector components are not localised at the same positions and therefore in a strict sense energy related quantities are not defined at any discrete grid point. The idea to overcome this problem is to interpolate the field values at a certain point and then calculating the correspondant local value of the derived quantities. This works fine if we e.g. want to calculate the electric field intensity $\vec{E}^2(\vec{r}_0, t_0)$:

$$\begin{aligned}
 \vec{E}^2(\vec{r}_0, t_0) \rightarrow \vec{E}^2|_{i_0, j_0, k_0}^{n_0} &= \frac{1}{4} \left[E_x|_{i_0 - \frac{1}{2}, j_0, k_0}^{n_0} + E_x|_{i_0 + \frac{1}{2}, j_0, k_0}^{n_0} \right]^2 + \\
 & \frac{1}{4} \left[E_y|_{i_0, j_0 - \frac{1}{2}, k_0}^{n_0} + E_y|_{i_0, j_0 + \frac{1}{2}, k_0}^{n_0} \right]^2 + \\
 & \frac{1}{4} \left[E_z|_{i_0, j_0, k_0 - \frac{1}{2}}^{n_0} + E_z|_{i_0, j_0, k_0 + \frac{1}{2}}^{n_0} \right]^2
 \end{aligned} \tag{6.57}$$

However, as soon as more than one interpolating operation is needed as e.g. when quantities contain E- and H-fields (spatial and temporal interpolation) we see that the interpolation operations do not commute. There are no unambiguous arguments for choosing

a certain order in which the interpolations are performed, but it has been pointed out in [57] that the consistency of Poyntings's theorem can be assured. Despite other existing possibilities we used the form introduced in [57] for a consistent version of Poynting's theorem in this work.

We therefore introduce the interpolation operators \hat{m}_i acting on a function $F|_{i,j,k}^n$

$$\hat{m}_t F|_{i,j,k}^n = \frac{1}{2} \left[F|_{i,j,k}^{n-\frac{1}{2}} + F|_{i,j,k}^{n+\frac{1}{2}} \right] \quad (6.58)$$

$$\hat{m}_x F|_{i,j,k}^n = \frac{1}{2} \left[F|_{i-\frac{1}{2},j,k}^n + F|_{i+\frac{1}{2},j,k}^n \right] \quad (6.59)$$

$$\hat{m}_y F|_{i,j,k}^n = \frac{1}{2} \left[F|_{i,j-\frac{1}{2},k}^n + F|_{i,j+\frac{1}{2},k}^n \right] \quad (6.60)$$

$$\hat{m}_z F|_{i,j,k}^n = \frac{1}{2} \left[F|_{i,j,k-\frac{1}{2}}^n + F|_{i,j,k+\frac{1}{2}}^n \right] \quad (6.61)$$

and the following discrete counterparts of the energy contributions in 6.55:

$$\vec{j}(\vec{r}, t) \cdot \vec{E}(\vec{r}, t) \rightarrow j_x \cdot \hat{m}_x E_x + j_y \cdot \hat{m}_y E_y + j_z \cdot \hat{m}_z E_z \quad (6.62)$$

$$S_x(\vec{r}, t) \rightarrow \hat{m}_y [\hat{m}_x E_y \cdot \hat{m}_t H_z] - \hat{m}_z [\hat{m}_t H_y \cdot \hat{m}_x E_z] \quad (6.63)$$

$$S_y(\vec{r}, t) \rightarrow \hat{m}_z [\hat{m}_y E_z \cdot \hat{m}_t H_x] - \hat{m}_x [\hat{m}_t H_z \cdot \hat{m}_y E_x] \quad (6.64)$$

$$S_z(\vec{r}, t) \rightarrow \hat{m}_x [\hat{m}_z E_x \cdot \hat{m}_t H_y] - \hat{m}_y [\hat{m}_t H_x \cdot \hat{m}_z E_y] \quad (6.65)$$

$$\epsilon(\vec{r}) \vec{E}^2(\vec{r}, t) \rightarrow \hat{m}_x [\epsilon E_x^2] + \hat{m}_y [\epsilon E_y^2] + \hat{m}_z [\epsilon E_z^2] \quad (6.66)$$

$$\begin{aligned} \vec{H}^2(\vec{r}, t) &\rightarrow \hat{m}_y \hat{m}_z \left[H_x^{n-\frac{1}{2}} H_x^{n+\frac{1}{2}} \right] + \\ &\hat{m}_z \hat{m}_x \left[H_y^{n-\frac{1}{2}} H_y^{n+\frac{1}{2}} \right] + \\ &\hat{m}_x \hat{m}_y \left[H_z^{n-\frac{1}{2}} H_z^{n+\frac{1}{2}} \right] \end{aligned} \quad (6.67)$$

and use these relations for all energy related calculations in this work.

Spectral Information

The solutions of Maxwell's equations investigated in this work can be decomposed into simple time-harmonic or exponentially damped time-harmonic modes. Especially the bandstructures and eigenmodes are defined in frequency domain. However, the FDTD-algorithm as a time-domain method produces time-dependant results and therefore we need a transformation into frequency domain to discuss results in the right terms. This is done by fourier transformation that is well known as

$$f(\vec{r}, \omega) = \frac{1}{\sqrt{2\pi}} \int dt f(\vec{r}, t) e^{i\omega t} \quad (6.68)$$

and its discrete equivalent for a finite number N of timesteps with width Δt

$$f(\vec{r}, \omega) = \frac{\Delta t}{\sqrt{2\pi}} \sum_{n=1}^N f(\vec{r}, n) e^{i\omega n \Delta t} \quad (6.69)$$

Due to the finite timestep and the finite summation interval we have limitations for the accuracy of $f(\vec{r}, \omega)$. It can be shown that Δt is proportional to the highest frequency ω_{max} that can be calculated properly, while N is proportional to the resolution in frequency space $\Delta\omega$.

Now we want to transform time-domain data obtained by a FDTD-simulation of $S = i_{max} \cdot j_{max} \cdot k_{max}$ spacepoints and N timesteps. We see that for the complete transformation we would have to store $S \cdot N$ (in units of required memory for all field components of one discrete space point) numbers to apply eq. 6.69. In most practical cases this is impossible due to constraints of computing resources. Depending on the problem under consideration we have to choose from one of the following two possibilities for reducing memory requirements: First, we have a problem where we want to cover precisely a large frequency interval with highest possible accuracy, but it is sufficient to calculate the spectrum at a few space points S_0 . In this case it is favourable to store the time series for the few space points and calculate the fourier transform in a post-processing step. One can also benefit then from highly efficient commercially available fast-fourier-transform (FFT) routines. The requirements of computing memory are essentially $S_0 \cdot N$. Second, if we need spectral information at so many different space points that we cannot store all time series in memory we can do the fourier transform on-the-fly. This means that after each integration step we calculate for each desired frequency $\omega_f (f = 0..F_0)$ the new contribution in the sum of 6.69.

$$f(\vec{r}, \omega_f, n + 1) = f(\vec{r}, \omega_f, n) + f(\vec{r}, n + 1) e^{i\omega_f(n+1)\Delta t} \quad (6.70)$$

This method reduces the memory requirements to $S_0 \cdot F_0$ because we only have to store the actual value of the fourier sum for each desired frequency and not the whole time series. This is obviously only an advantage if we do not want to calculate the fourier transform for all possible frequencies. The disadvantage is that the computation of the fourier sum is much less efficient than the post-processing fourier transform. It is only recommendable if one restricts to a smaller number of frequency values. This condition is fulfilled in most cases because the maximum frequency determined by Δt due to the stability condition is much larger than the frequencies to be considered for physical results.

Another important aspect of the fourier transform is the phenomenon known as Gibb's oscillations. It states the following: If the corresponding time signal of a Heavyside function is truncated and transformed back into frequency domain the discontinuity is not represented properly. In the vicinity of the discontinuity there are oscillations that grow towards the discontinuity. With an increasing integration interval the frequency of the Gibb's oscillation increases and the oscillations shift closer to the discontinuity while their amplitudes increase. Strictly speaking this phenomenon can not be avoided because we always deal with finite intervals. In practice, e.g. when we have a dielectric structure that acts as a Heavyside-shaped filter we always have the disturbing effects of Gibb's oscillations. This problem can be faced in different ways: One way is to choose an integration interval that is large enough so that the frequency of Gibb's oscillations is well below the desired frequency resolution. Then in most cases results are affected only negligibly. This has the disadvantage of significantly increasing the required computation time. Another way is to apply filter functions as it is well known in signal processing [58]. It means that the time signal is multiplied with a filter function before being fourier transformed. In frequency domain this results in a convolution of the filter function with the desired spectrum which influences the result. There exists a large variety of filter functions that try to minimise the error in different aspects, e.g. for low or high frequencies. Effectively this filter functions cause a smoothing of the discontinuity and thereby suppress the oscillations. The question, if or what filter functions should be used depends on the desired results. E.g. when we want to know a transmission spectrum over a wide range of frequencies a filter function would be desirable, while if we only want to know the precise position of the Heavyside function (e.g. the bandedge of a photonic crystal) the smoothing would make the result more inaccurate. The considerations so far in this subsection are more or less independent of the input quantities and are directly applicable to E- and H-fields. However, we want to stress now that one has to be careful when dealing with energy related quantities. If we want e.g. to calculate the spectral transmission via the spectral energy flow described by the Poynting vector $\vec{S} = \vec{E} \times \vec{H}$ we see that the outer product does not commute with the fourier transform $FT(f)$:

$$FT \left[\vec{E}(\vec{r}, t) \times \vec{H}(\vec{r}, t) \right] \neq FT \left[\vec{E}(\vec{r}, t) \right] \times FT \left[\vec{H}(\vec{r}, t) \right] \quad (6.71)$$

We will now illustrate by a simple example why the right hand side of 6.71 is the physically correct choice:

Assume a time signal that consists of two propagating plane waves with different frequency

$$E_y(x, t) = E_y^{(1)} \sin(\omega_1 t - k_1 x) + E_y^{(2)} \sin(\omega_2 t - k_2 x) \quad (6.72)$$

$$H_z(x, t) = H_z^{(1)} \sin(\omega_1 t - k_1 x) + H_z^{(2)} \sin(\omega_2 t - k_2 x) \quad (6.73)$$

Both plane waves superpose and carry energy of their frequency. In a power spectrum we would expect two delta-shaped peaks at ω_1 and ω_2 . This result is achieved by first fourier transforming E_y and H_z separately and then calculating the Poynting vector:

$$\begin{aligned} S(x, \omega) &= E_y(x, \omega) \cdot H_z(x, \omega) \\ &= [E_y^{(1)}\delta(\omega - \omega_1) + E_y^{(2)}\delta(\omega - \omega_2)] \cdot [H_z^{(1)}\delta(\omega - \omega_1) + H_z^{(2)}\delta(\omega - \omega_2)] \\ &= E_y^{(1)}H_z^{(1)} \cdot \delta(\omega - \omega_1) + E_y^{(2)}H_z^{(2)} \cdot \delta(\omega - \omega_2) \end{aligned} \quad (6.74)$$

while fourier transforming the time-dependant Poynting vector $\vec{S}(t)$ would give additional peaks for the beat frequencies $0.5(\omega_1 + \omega_2)$ and $0.5(\omega_1 - \omega_2)$ which is unphysical with respect to our assumptions. We should also note that Gibb's oscillations are energy conserving when integrated over the whole frequency space but can lead to local violations around the discontinuity. It has been observed by the author that e.g. for transmission $T(\omega)$ and reflection $R(\omega)$ simulations the sum $R + T$ that should be equal to one regardless of frequency also contains the oscillations around the discontinuity.

6.3 Application to Photonic Crystals

6.3.1 Bandstructure and Eigenmode Calculations

The eigenvalues and eigenmodes of a periodic dielectric system are often calculated as the solution of the frequency domain master equation 3.13, e.g. by the decomposition of the spatial dimensions into a finite plane wave basis and solving the resulting matrix equation. This is very effective and well established in the photonic crystal community and freeware computer codes are available [59]. Nevertheless, plane wave solvers have the intrinsic disadvantage that they require a periodicity in all space directions and therefore can not handle open systems with complex eigenvalues. There are several efforts to solve this problem in frequency domain but there is still no established solution for three dimensional systems [60].

In time-domain, the proper implementation of open boundaries is well known as described in 6.2.2. As the main aspect of this work concerns the optical properties of photonic crystal slabs we use a modified FDTD algorithm for bandstructure calculations in this work. In some sense this type of algorithm is less efficient than plane wave methods, because not all information provided by the master equation is used to optimize the algorithm. However, because of the possibility to address open system the FDTD-based method is much more general.

In the following subsections we will give a description of the principal setup of the used method as well as practical hints concerning convergence and efficiency.

Structure of Bandstructure and Eigenmode Calculation

The principle setup of a bandstructure calculation based on FDTD is as following: In a first step we model a unit cell of the photonic crystal containing the dielectric structure and apply proper, problem adapted boundary conditions. The unit cell is not necessarily primitive. There is also the possibility of choosing conventional unit cells or supercells. The first is e.g. necessary when the primitive unit cell is not rectangular and therefore cannot be fit into a cuboid computation domain as it is the case for a hexagonal two-dimensional structure or the face-centered-cubical structure in three dimensions, while the second is used for defect calculations. As it is the nature of photonic crystals we have periodic boundary conditions at least in one space dimension. The associated k -vector is therefore a parameter of the calculation and to obtain the complete bandstructure we have to repeat the following steps for each desired k -value of the Brillouin zone. Next we have to excite the system by an external source. The proper choice of the excitation depends strongly on the actual system and is therefore discussed in detail in the corresponding sections. Then the system is time-integrated for a certain number of discrete time-steps (that determines later the resolution in frequency space, see 6.2.4), while the excitation projects on the eigenmodes supported by the system that are now oscillating harmonically for a closed or damped-harmonically for an open system. It is obvious that the coupling strength of the excitation to each crystal mode can strongly vary. It is even possible that modes are not excited due to an improper spatial or spectral excitation. For the identification of the frequency eigenvalues corresponding to the given k -vector it is now sufficient (assumed all modes has been properly excited) to fourier transform the time series of one field component at one space point and identify the peaks of the frequency spectrum with the eigenvalues. In practice, it is dangerous to rely just on one component and one space point because by chance one can choose a point that lies in a node plane of a mode that is consequently missing in the spectrum. Also just one field component can be zero for a mode of a certain polarisation. The codes in use for this work therefore choose randomly a number of test points and components (typically 10 to 50) to minimise the risk of missing some modes for these reasons.

After determining the eigenvalues the eigenmodes can be extracted by repeating the calculation and applying discrete Fourier transformations for the known eigenvalues. This can be understood as applying very narrow band filters to extract the eigenmodes out of the mode superposition oscillating in the system.

Material Definition and Convergence

In a FDTD algorithm the computational domain is divided into discrete subcells and the spatial derivatives are approximated by finite differences. We now want to discuss how fine the numerical space has to be resolved to get reliable results, or in other words, how many grid points are needed and how far the material definition of the dielectric

scatterers influences accuracy.

The simplest test to check convergence is to calculate the same physical system with different resolutions and compare the results of certain output parameters. It must be stressed that different output parameters like eigenvalues or energies can have different sensitivity to the resolution. If the results are within a certain interval of accuracy we say the result has converged and we use the lowest resolution that obtains this result for optimum efficiency.

We now set up an example system to demonstrate this procedure. We choose the very simple case of dielectric cylinders surrounded by air and arranged in a square lattice in two dimensions. However, when we want to assign the value for $\epsilon(\vec{r})$ on the discrete grid we face a problem. The circular scatterer cannot be properly represented on the rectangular grid. There are several reasonable choices how to assign the $\epsilon(\vec{r})$ -value. E.g.

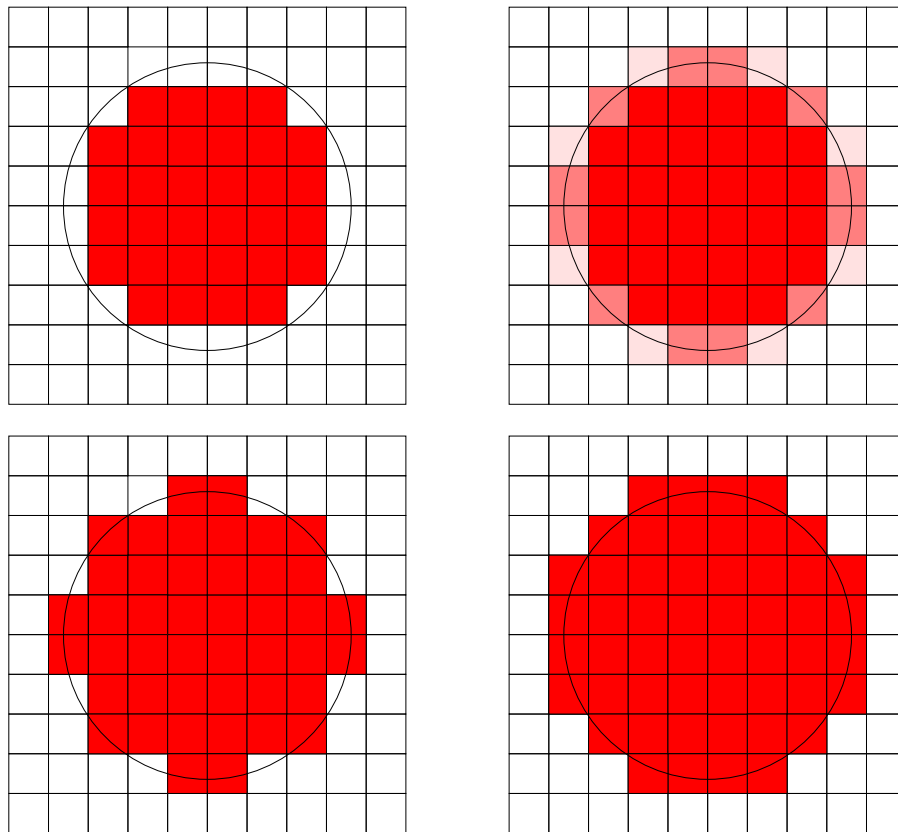


Figure 6.4: Illustration of different types of mapping a circular scatterer onto the discrete rectangular grid. The circle represents the shape of the ideal scatterer. Further explanation is given in the text.

we can give all discrete cells the value of the dielectric that lie completely within the circle as can be seen in fig. 6.4 (upper left). In the limit of an infinite resolution this would perfectly represent the circle. However, for lower resolutions it is obviously a

lower boundary for the size of the scatterer and the results will correspond to a slightly smaller scatterer. Analogous we can construct an upper boundary by assigning the value of the high dielectric material to all cells that touch the circle (fig. 6.4 (lower right)). A good compromise would be to analyse the relative volume fraction of the ideal cylinder in each cell and assign the corresponding index value only when more than half of the cell is occupied by the cylinder (fig. 6.4 (lower left)). For this case we now calculate two typical eigenfrequencies depending on the number of gridpoints N per lattice constant a which means that the whole unit cell is divided into N^2 discrete cells. The curves are shown in fig. 6.5 marked with open squares. We can see that especially for the lower eigenvalue the convergence behaviour is quite bad and even for 120 points per lattice constant there is still no convergence.

We therefore try to improve our material modelling once more by not only using the

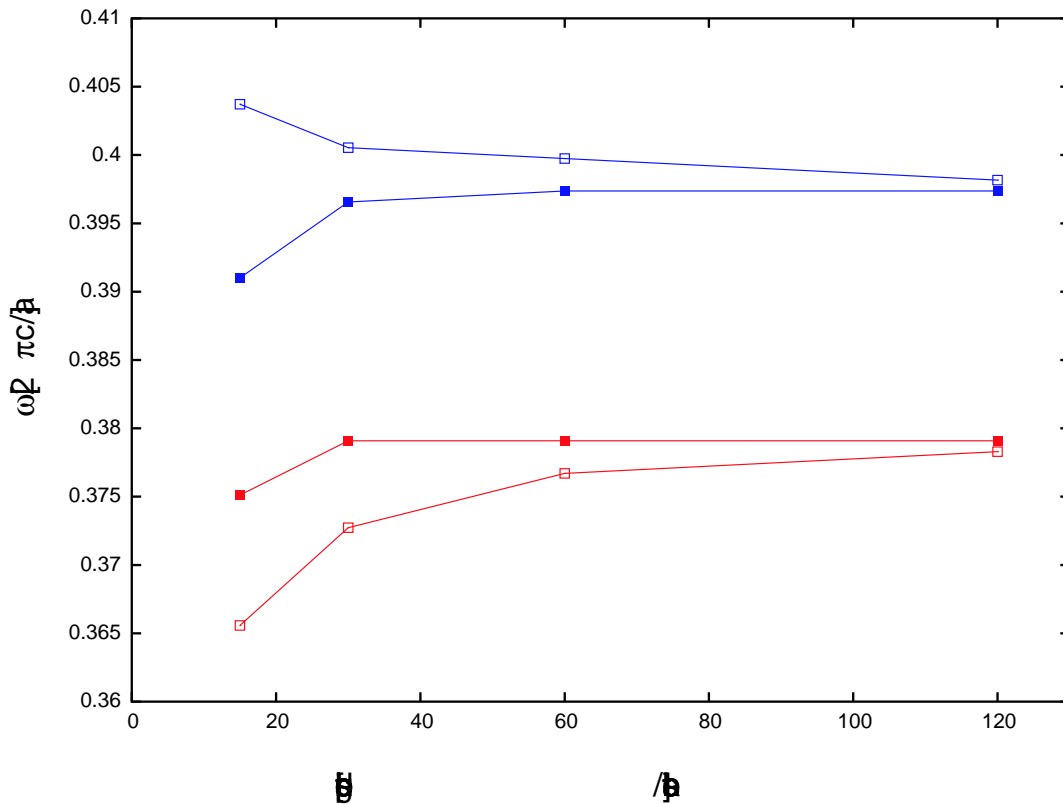


Figure 6.5: Convergence behaviour of two eigenvalues for different modelling of the scatterers. Open squares represent the staircase method; filled squares the fuzzy-cell method.

filling fraction of a cell at the edge of the cylinder for the decision if high or low index is assigned. Now we calculate an average refractive index weighted by the filling fraction and assign it to the edge cells. This is illustrated in fig. 6.4 (upper right) by the use of a grey scale. This method, often referred as fuzzy-cells, represents best the total filling



Figure 6.6: Dielectric distribution of the conventional unit cell. white: $n=3.4$, black: $n=1.0$

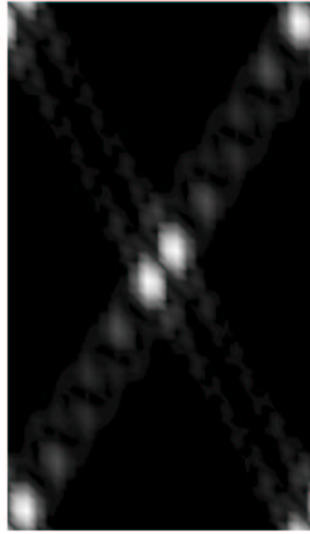


Figure 6.7: Initial condition (a): H-field intensity

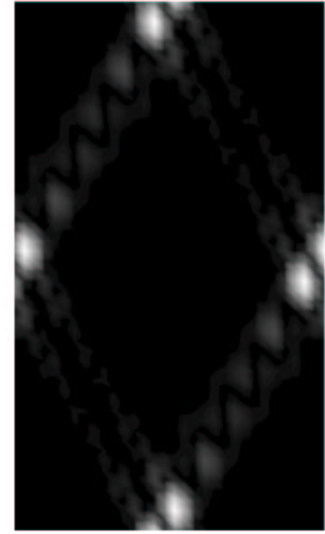


Figure 6.8: Initial condition (b): H-field intensity

fraction of high index material in the unit cell. The curves represented by filled squares in fig. 6.5 show a dramatically better convergence behaviour. Good convergence is reached for 30 grid points per lattice constant. The disadvantage of fuzzy-cells is that the discontinuous nature of the dielectric interfaces smoothes. This may have disadvantages for other applications. However, in the case of photonic crystals fuzzy-cells have proven to be the most effective way of material modelling. It should be added here that in plane wave methods there exists an even more sophisticated way of averaging. Depending on the polarisation of the electric field relative to the surface either the dielectric constant or its reciprocal are averaged, leading to an even better convergence.

Regardless of the used material model there exists the problem that the scatterer has a different symmetry in the numerical grid. E.g. a circular scatterer has ideally a higher symmetry than the lattice in a hexagonal arrangement. However, in the FDTD grid it has strictly speaking a square symmetry and therefore it is lower than that of the lattice. This can cause a small lifting of degeneracies and therefore splitting of bands in some cases.

Purely Periodic Systems

A purely periodic system is bounded in all space directions by periodic boundary conditions. We have discussed one- and two-dimensional examples in chapter 3 and a three-dimensional example in chapter 5. Now we discuss which type of excitation has

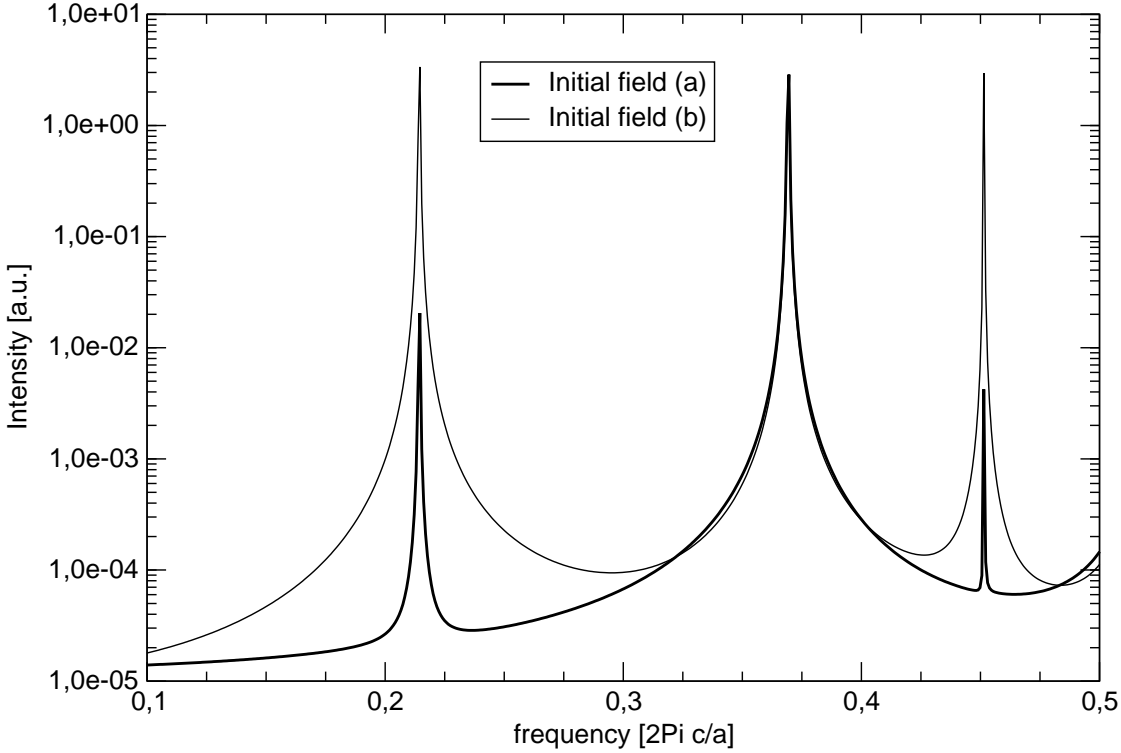


Figure 6.9: Spectra for initial fields with different spatial localisation at the M -point of an hexagonal lattice.

to be used to obtain comprehensive and reliable results.

First, we recall some known properties of the system and the desired results: Due to its periodic boundary conditions the computational domain cannot lose energy. Moreover, the eigenmodes form a complete set of linear independent eigenfunctions. This has the consequence that the eigenvalues are real and the expected peaks in the spectra are δ -shaped. The consequence is that the initial condition will project onto this set of eigenfunctions with a strength that is only determined by its spatial overlap. Afterwards each mode contains and conserves a certain amount of energy. To excite all modes reliably we have to take care of the spatial distribution of the initial condition, including polarisation. If we additionally assure that the excitation covers the whole range of frequencies of interest, the results should be comprehensive. Moreover, we can use an additional property of the solution to improve convergence and reduce noise: We know that the eigenmodes can be decomposed into plane waves with wavevector $(\vec{k} + \vec{G}_i)$. If

the excitation also consists only of these plane waves, this would improve the efficiency of the calculation (see 6.2.3).

These preliminary considerations lead to the ansatz of an initial field distribution consisting of the superposition of plane waves of the form

$$\vec{H}(\vec{r}, t = 0) = \sum_{\vec{G}_i} \left[\vec{v} \times (\vec{k} + \vec{G}_i) \right] e^{i\vec{r}(\vec{k} + \vec{G}_i) + i\Phi_i} \quad (6.75)$$

where we have two arbitrary parameters \vec{v} and Φ . The form of the amplitude of each plane wave $\vec{v} \times (\vec{k} + \vec{G}_i)$ forces transversality of the plane waves and satisfies the homogeneous Maxwell equation $\nabla \vec{H} = 0$ [61]. \vec{v} is arbitrary and provides an additional degree of freedom that can be used especially in two dimensional systems. As described in 3.1.5 the 2D case decomposes in TE- and TM-modes. If we choose e.g. $\vec{v} = (0, 0, v_z)$ the polarisation of the plane waves is always TM while for $\vec{v} = (v_x, v_y, 0)$ we have TE polarisation. We can therefore selectively excite modes of a certain polarisation by a proper choice of \vec{v} .

The other arbitrary parameter, the phase Φ_i of each plane wave can be used to adjust the spatial distribution of the initial condition. We will demonstrate this now for a two dimensional example.

We calculate the spectrum for a hexagonal lattice of air holes with radius $r = 0.375a$ in a dielectric background with refractive index $n = 3.4$ at the M -point of the first Brillouin zone. A sketch of the dielectric structure of the conventional unit cell used for computation is shown in fig. 6.6. As discussed in 3.3.1 the first and the third TE-band at M concentrate the energy mainly in the dielectric region while the second TE-band has significant intensity within the holes. We therefore adjust Φ_i in a way that the intensity of the initial field is either concentrated in the holes (fig. 6.7) or in the high dielectric region (fig. 6.8). The initial conditions consist of 121 plane waves corresponding to the reciprocal lattice vectors

$$\vec{G}_{i,j} = \sum_{i=-5}^5 \sum_{j=-5}^5 i\vec{G}_1 + j\vec{G}_2 \quad (6.76)$$

with G_1 and G_2 representing the primitive lattice vectors of the structure. It should be stressed that this superposition of plane waves must not be seen in the sense of a decomposition. It just provides "material" for the system that can be mapped on the eigenmodes. A further increase of the number of plane waves does not give any advantage.

Fig. 6.9 compares the spectra for the two different initial conditions. For the initial condition localised in the high dielectric region the peaks of all three bands have intensities in the same order of magnitude while for localisation in the air holes the peak of the second band is more than two orders of magnitude larger. In the chosen example nevertheless all peaks can be clearly identified. However, in situations where modes of

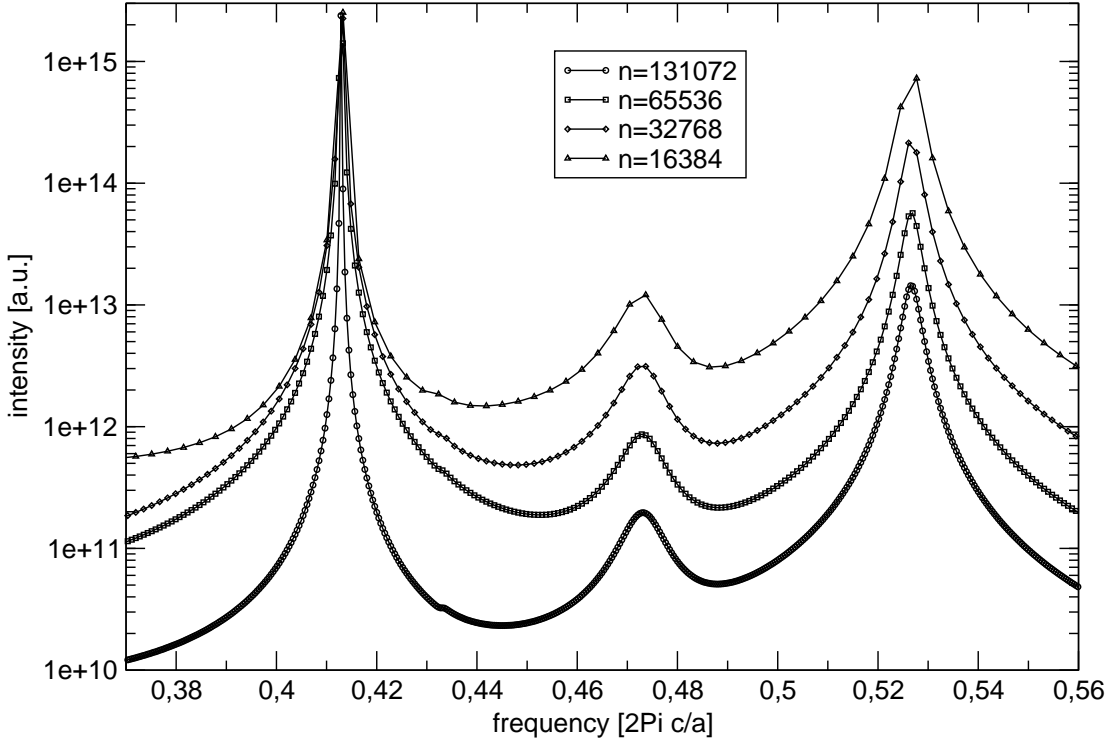


Figure 6.10: Spectra for different integration intervals at $0.75 |\Gamma - M|$ of a slab system with Si -core and finite SiO_2 -claddings ($d=1.2a$). Parameters see 4.3.3.

different localisation have nearly the same frequency they can only be resolved with a careful adaptation of the initial condition.

Partially Open Systems

If we want to calculate the bandstructure of a system that is at least open in one direction the physical situation changes substantially. As the analysis of two dimensional photonic crystal slabs is the central aspect of this work (see chapter 4) we will now carefully discuss excitations that allow a reliable identification of eigenmodes in a lossy system.

The photonic crystals under investigation generally contain both guided modes with a δ -shaped line in frequency domain and exponentially decaying "lossy" modes with a corresponding Lorentzian lineshape in the spectra. This leads to a major problem when

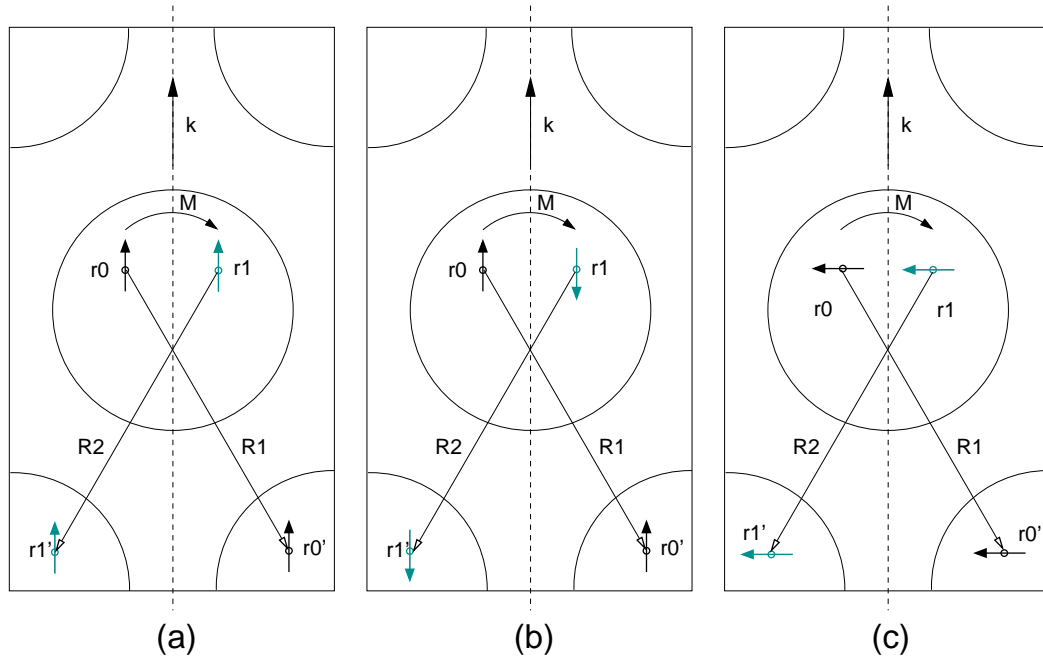


Figure 6.11: Arrangements of point dipole sources within the conventional unit cell of the hexagonal lattice for different symmetries and polarisation.

bandstructures with high frequency resolution are needed. E.g. we assume a system with one guided and one lossy mode and integrate over a time interval T with a corresponding frequency resolution $\Delta\omega$ and choose the initial condition in a way that both peaks have the same intensity. If we now increase T to decrease $\Delta\omega$ the ratio of the peak intensities is not 1 anymore because the peak intensity of the lossy mode becomes comparably smaller. The reason is that in the Fourier sum the additional contributions of the longer integration time are constant for the guided mode while these for the lossy mode decay exponentially. Fig. 6.10 shows this effect for a realistic structure as investigated in 4.3.3. The three peaks correspond to the second, third and fourth TE-modes at the M -point. The second band is below the air light cone and therefore guided while the third and the fourth are lossy. The effect described above can be clearly seen by the comparison of four different integration intervals.

The consequence is that we cannot reach an arbitrary frequency resolution because at a certain point the lossy modes would disappear in the noise of the spectra. This represents a major disadvantage of a time domain method in this case. We can not rely on a very general excitation but have to apply additional information about the expected

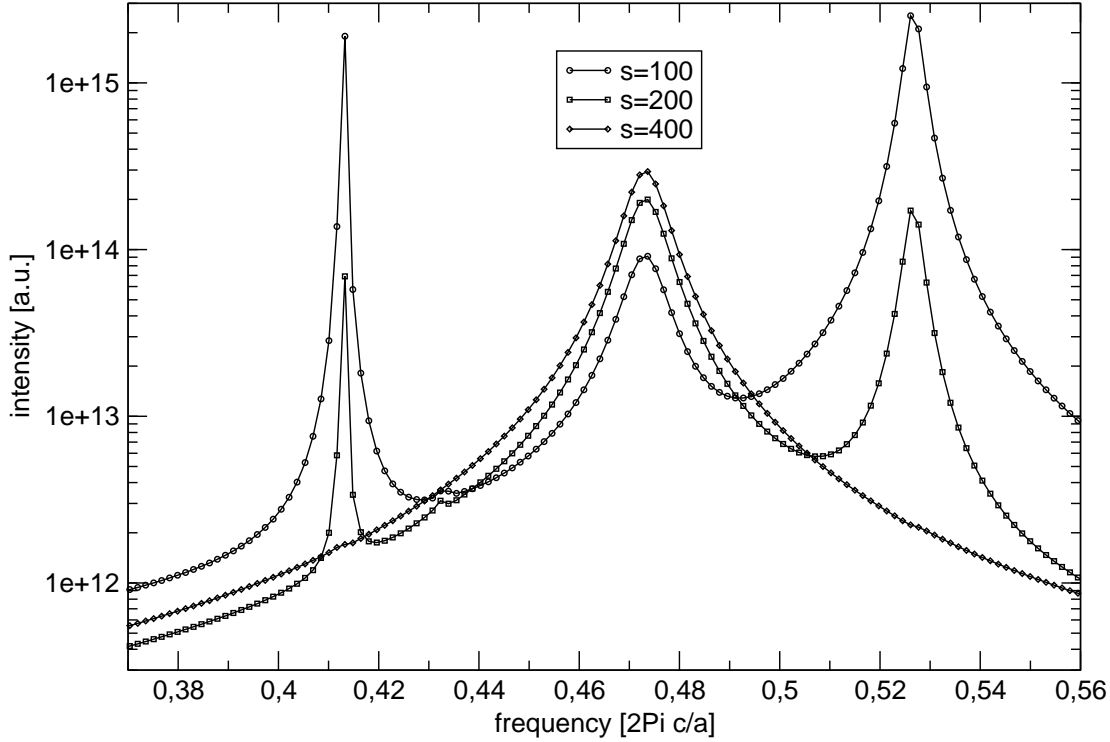


Figure 6.12: Spectra for different spectral widths of the exciting pulse.

solutions. To achieve this we have two possible strategies. First, we can selectively excite the desired mode by spatially localising the excitation or even use symmetry properties. Second, we can selectively excite a frequency range by a pulsed source. In practice, for problems that are difficult to address because we know only a little about the solution, generally a combination of both is applied. There is no general guideline for the optimum choice and a large part depends on experience. In the following we will discuss a type of pulsed excitation that has been widely used in chapter 4 of this work.

A simple way to realise a pulsed source is the use of a pointlike current source at position \vec{r}_0 as described in 6.2.3. In our calculation we use a sine function with center frequency ω_0 and a Gaussian envelope with width s .

$$\vec{j}(\vec{r}_0, t) = \vec{j}_0 \cdot \sin \left[\frac{2\pi c}{a} \omega_0 (t - t_0) \right] e^{-\frac{1}{2} \left(\frac{t-t_0}{s} \right)^2} \quad (6.77)$$

As it would lead to an unwanted additional peak at ω_0 we must start the fourier transform not until the external current has vanished and only its emitted fields remain in the system. We define therefore a time $T = 2t_0$ when we start with the fourier transform and relate t_0 and s in a way that $\vec{j}(\vec{r}_0, T)$ is below a certain threshold. In the following calculations this was done with $t_0 \approx 3s$, leading to $\vec{j}(\vec{r}_0, T) < 2\%$. When we apply this to the conventional unit cell of a hexagonal lattice we have to be careful with the spatial localisation of the current source. If we would use just one pointsource in the conventional unit cell that is physically repeated infinitely in the crystal plane the periodicity of the dielectric lattice would be different than that of the point sources. The lattice constant of the currents would be larger, causing smaller k -values and effectively an artificial backfolding of the bandstructure. To avoid this we have to place current sources at each position of the conventional unit cell that can be mapped by a lattice vector \vec{R} to \vec{r}_0 . Fig. 6.11(a) shows an example for \vec{r}_0 mapped to \vec{r}_0' by the lattice vector \vec{R}_1 . The two dipole sources have now the correct lattice periodicity. However, we must also take the phase between the two dipoles into account because otherwise their emission into plane waves with wavevector $\vec{k} + \vec{G}_i$ would destructively interfere. We must choose the phase relation according to Bloch's theorem for fields in different unit cells:

$$\vec{j}(\vec{r}_0, t) = e^{i\vec{k}\vec{R}_1} \cdot \vec{j}(\vec{r}_0', t) \quad (6.78)$$

This has also to be taken into account when modes of certain symmetries are excited selectively. In chapter 4 we restrict ourselves to modes with odd symmetry with respect to the \vec{k} -z-plane for Γ - M -direction (dashed line in fig. 6.11(a)-(c)). Therefore our current sources have to be arranged accordingly. We mirror the source at \vec{r}_0 by the operation \hat{M} to \vec{r}_1 and add the second source \vec{r}_1' by the application of \vec{R}_2 . To excite the desired mode symmetry we also have to be careful with the polarisation of the dipoles. We recall that parallel components of the electric field transform odd for odd modes while normal components transform even for odd modes (see 3.1.5). The dipole polarisations to achieve odd modes are therefore as shown in fig. 6.11 (b)-(c) while (a) shows an even excitation.

Now we have all ingredients for selectively exciting an odd mode. For the structure used as an example above in this chapter we gradually modify t_0 and s around the frequency of the third TE-band. The results are shown in fig. 6.12. We see that for $s = 100$ the neighboring modes are still dominating, for $s = 200$ all three modes have approximately the same intensity and for $s = 400$ only the desired mode is detectable.

At the end of this section we note that the selective excitation of a single mode is computationally very expensive when whole bands or bandstructures have to be analysed. Effectively, with a nearly monochromatic excitation the main advantage of time-domain methods vanishes. This approach should only be applied for critical positions within the bandstructure as for example occurring at avoided crossings. However, the careful use of all presented strategies of mode excitation provide an excellent toolkit for the analysis

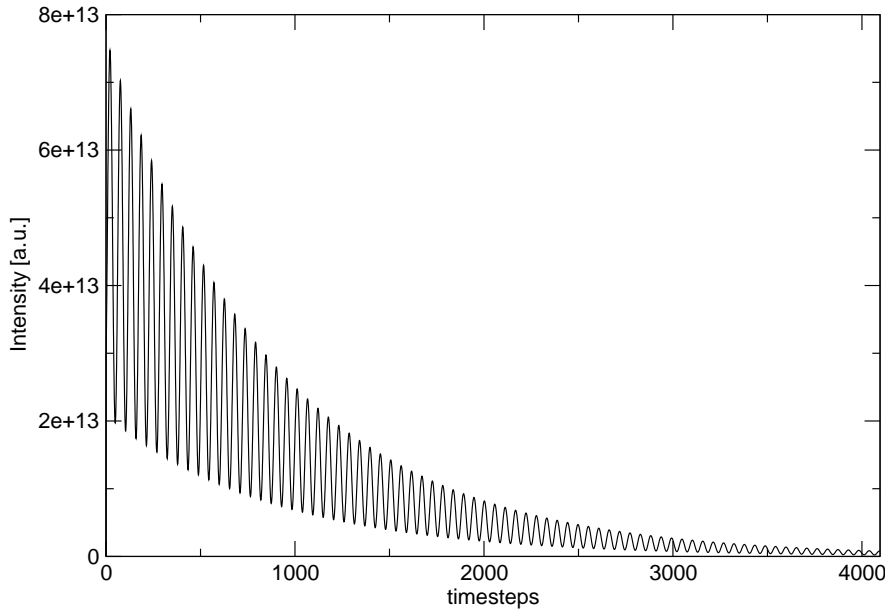


Figure 6.13: E-field intensity of a monochromatic excitation after the decay of the excitation current at a randomly chosen space-point.

of photonic crystal structures supporting guided as well as lossy modes.

Calculation of Losses

The real parts of the eigenvalues can be easily determined as the peak positions in the obtained spectra as discussed in the preceding chapter. In the case of lossy modes we are also interested in the imaginary part that represents the temporal decay of a mode. Principally this could be done in two ways: We can either determine the width of the peaks in the frequency spectra or directly extract the temporal information for a monochromatic excitation. On the first view the frequency domain approach looks more useful because the data can be obtained for all modes corresponding to a certain k -value in a single simulation. However, in practice we have the problem that we need a high resolution in frequency for precisely determining the linewidth. As described before this reduces the peak height relative to these of guided modes and therefore the error caused by neighboring peaks increases. In contrast a monochromatic excitation requires a larger number of time steps before the excitation current has decayed, but afterwards a relative small number of time steps is sufficient to determine the temporal decay. Even if we repeat this for several bands the total computation time is not significantly larger than

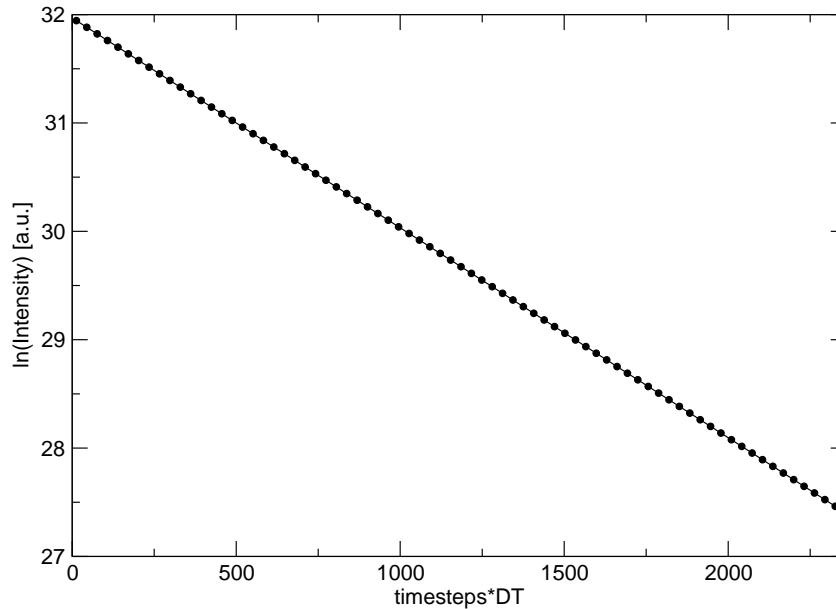


Figure 6.14: Logarithmic graph of the maxima of the intensity decay displayed in 6.13 (circles) with linear fit (line).

for a spectral analysis. We will demonstrate this now for a typical example choosing the same example system as used in 6.3.1. We have seen that the parameters $t_0 = 1200$ and $s = 400$ lead to a selective excitation of the lossy mode for $\omega_0 = 0.473$. We will now analyse the temporal behaviour of the electric field intensity at a randomly chosen point \vec{r}_0 . Fig. 6.13 shows a clear exponential decay of the intensity. The approach we will now use to extract the decay constant $Im(\omega)$ is simple: We extract the maxima of the oscillatory decaying intensity and fit an exponential function (or, equivalent but more practical: use the logarithm of the intensity value and apply a linear fit). As we have a large number of maxima even for a small number of time steps (compared to what is needed for a proper resolution in frequency space) this linear fit is very precise. We will not discuss the fit algorithm in detail because we use predefined functions of commercial packages, but generally speaking a simple least square fit is sufficient. Fig. 6.14 shows the extracted maxima as well as the fit function.

6.3.2 Transmission and Reflection of Partially Periodic Systems

While the bandstructures and eigenmodes are properties of an ideal infinitely extended system, transmission and reflection are characteristic for finite and therefore more real-

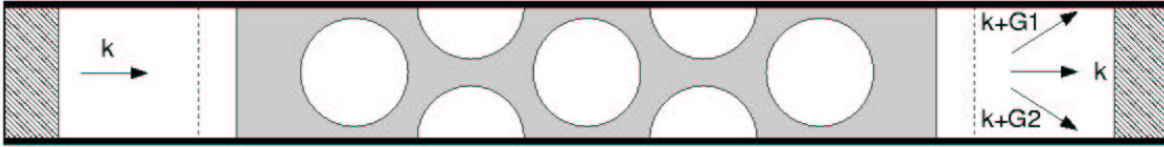


Figure 6.15: Schematic illustration of an in-plane cross-section of a system with free-space incoupling. White areas indicate air, grey areas silicon. Hatched areas symbolize PML- and bold lines periodic boundaries. Dashed lines are transmission and reflection planes, respectively.

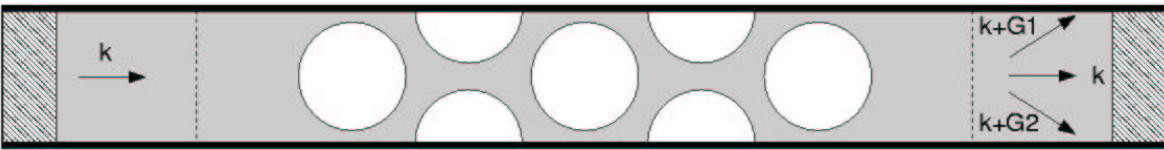


Figure 6.16: Schematic illustration of an in-plane cross-section of a system with planar-waveguide incoupling. White areas indicate air, grey areas silicon. Hatched areas symbolize PML- and bold lines periodic boundaries. Dashed lines are transmission and reflection planes, respectively.

istic structures. There is always an excitation that comes from the "outside" and enters the structure under investigation at an incoupling interface, interacts with the structure and leaves at an outcoupling interface. In a FDTD-simulation this means that we have to apply open boundaries at least in this direction of propagation where the structure is finite. In the directions perpendicular it is still possible to repeat the structure periodically into infinity. Fig. 6.15-6.18 show cross-sections for a three dimensional system where we have the finite direction of propagation, one periodically repeated crystal direction and an open out-of-plane direction. This is the typical setup for the calculation of transmission through a photonic crystal slab.

Very sloppy speaking the transmission is the fraction of the incoupled excitation that is going through the structure while the reflection is what is going backwards. However, if we look more careful at the problem we see that we have to define these numbers more precise to obtain unambiguous results.

To illustrate the problem we consider as a simple example system an air-bridge structure that is finite in Γ - M -direction and periodically repeated perpendicular. The first issue we should clarify is the type of termination in the finite direction. The cross-sections through the crystal plane in fig. 6.15 and fig. 6.16 show that we can e.g. either cut the structure so that it is entirely surrounded by air or we can continue the unperturbed waveguide. This choice has an important influence on the excitation signal as can be seen in the cross-section perpendicular to the crystal plane in fig. 6.17 and fig. 6.18. When we use a waveguide as an incoupling channel we can excite with modes that are

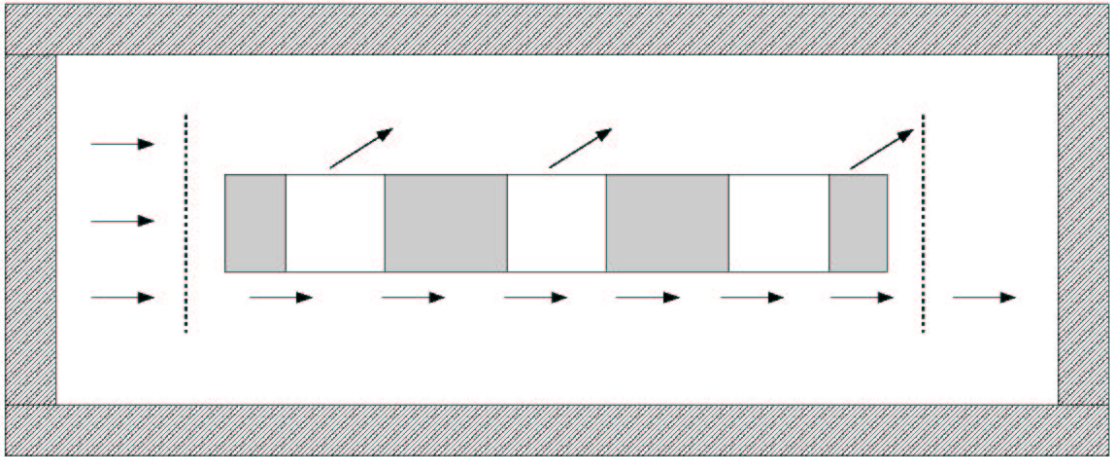


Figure 6.17: Cross-section perpendicular to the center of fig. 6.15. The arrows symbolize plane waves that interact with the structure (out-of-plane-scattering) or propagate unaffected below the structure.

confined to the slab while for a freespace incoupling plane waves or, more complicated, localised beam spots can be used. We define the transmission as the amount of energy W_T that crosses a given plane P

$$W_T = \int dt \int_P d\vec{r}^2 \vec{S}(\vec{r}, t) \quad (6.79)$$

at the end of the structure (marked as dashed lines in the pictures) normalised by the energy of the input. It is also obvious that all types of excitations give different transmission results. If we choose e.g. a monochromatic source with a frequency in the bandgap, the transmission of a waveguide mode excitation is much smaller than that of a plane wave excitation as illustrated in fig. 6.17 and 6.18. The reason is that in the case of free space incoupling there are plane waves that do not interact with the structure and directly reach the transmission plane (illustrated by the arrows below the structure in fig. 6.17). In the crystal plane the difficulties can be even more complicated because for a frequency above the bandgap the outcoupling has not only wavevector components in the direction of the incoupling but also contributions from Bragg-diffraction as illustrated in fig. 6.15. The last aspect to be mentioned here is the scattering out of the crystal plane that contributes as losses to the results. In fig. 6.17 and 6.18 it is illustrated that for an improper choice of the plane where transmission is calculated these losses can partially and wrongly contribute to transmission, especially for small angle scattering.

We saw even in this simple example that we have to carefully define the system and the excitation to obtain results that can be interpreted clearly and unambiguously which is especially critical when comparing with experimental measurements. We will now give

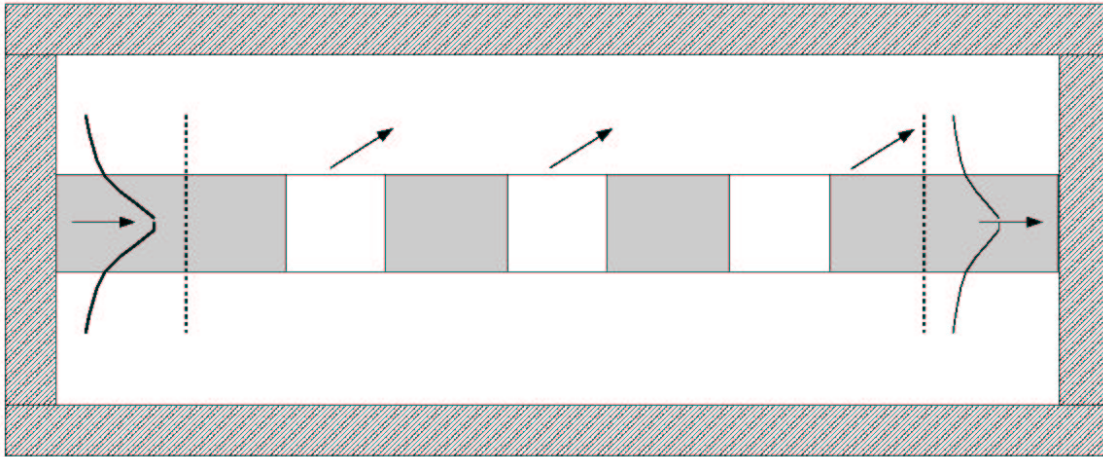


Figure 6.18: Cross-section perpendicular to the center of fig. 6.16. The excitation in this case is done by a localised waveguide mode.

a guideline how this can be achieved.

The definition of the surface termination and the incoupling channel is given due to practical or experimental constraints. The general approach of a well defined transmission and reflection calculation is as follows:

- Decompose the incoupling channel into a complete set of eigenfunctions. In most cases this will be either plane waves or eigenfunctions of a waveguide or a fibre.
- Analyse the mode structure of the incoupling channel and excite one well defined incoupling mode. This is a point where many mistakes are made in the FDTD-community. The simple excitation by an oscillating point source in a waveguide that is often used produces a very difficult to determine superposition of guided and radiating parts. The radiating parts can be sorted out by a sufficient length of the incoupling waveguide, but it remains still the problem that the resulting excitation is a superposition of guided modes of different orders and symmetries that strongly depends on system parameters like dipole source position that must not influence the physical results.
- Project the outcoupling signal onto the eigenfunctions of the outcoupling channel and calculate the percentage of the incoupling signal that is projected to each outcoupling channel.
- Repeat the previous step for a reflection plane with the set of counterpropagating incoupling modes as outcoupling channel.
- Repeat the two previous steps for each incoupling mode.

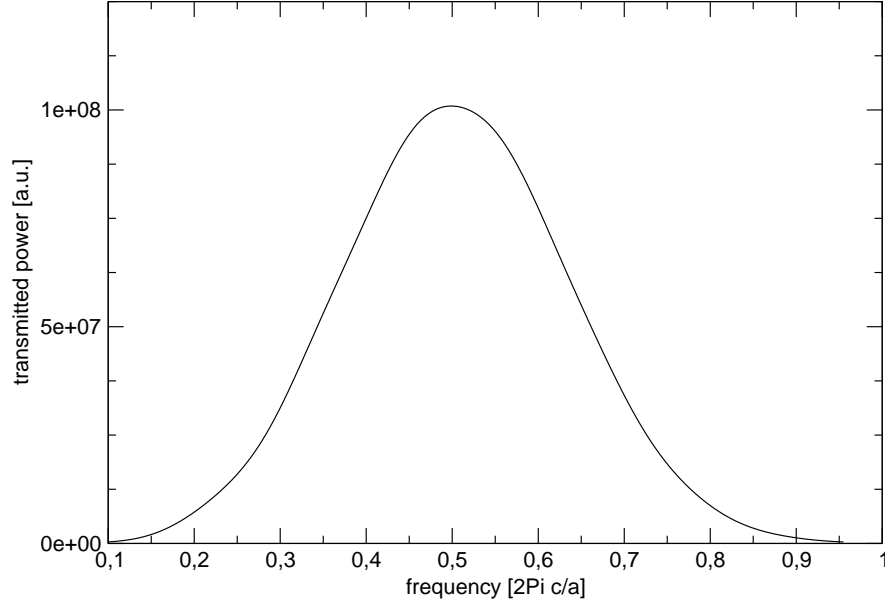


Figure 6.19: Spectral transmission profile of an incoupled waveguide pulse.

The complete result of a three dimensional transmission/reflection calculation of a lossy system would consist of two matrices, one for transmission and one for reflection, that relates each incoupling mode I to each outcoupling mode O of the system

$$\begin{pmatrix} O_1(\omega) \\ O_2(\omega) \\ \cdot \\ \cdot \\ O_n(\omega) \end{pmatrix} = \begin{pmatrix} T_{11}(\omega) & T_{12}(\omega) & \cdot & \cdot & T_{1n}(\omega) \\ T_{21}(\omega) & T_{22}(\omega) & \cdot & \cdot & T_{2n}(\omega) \\ \cdot & \cdot & \cdot & \cdot & \cdot \\ \cdot & \cdot & \cdot & \cdot & \cdot \\ T_{m1}(\omega) & T_{m2}(\omega) & \cdot & \cdot & T_{mn}(\omega) \end{pmatrix} \cdot \begin{pmatrix} I_1(\omega) \\ I_2(\omega) \\ \cdot \\ \cdot \\ I_m(\omega) \end{pmatrix} \quad (6.80)$$

and analogously for reflection. The losses L cannot be assigned to an output channel but can be given integral for one input channel as

$$L_m(\omega) = 1 - \sum_n T_{mn}(\omega) + R_{mn}(\omega) \quad (6.81)$$

For practical applications it is not necessary in most cases to know all transmission and reflection coefficients. E.g. it is sufficient to calculate the coefficients relating the fundamental modes of incoupling and outcoupling waveguide because higher modes suffer from large losses and are therefore not relevant. It is also common to integrate output

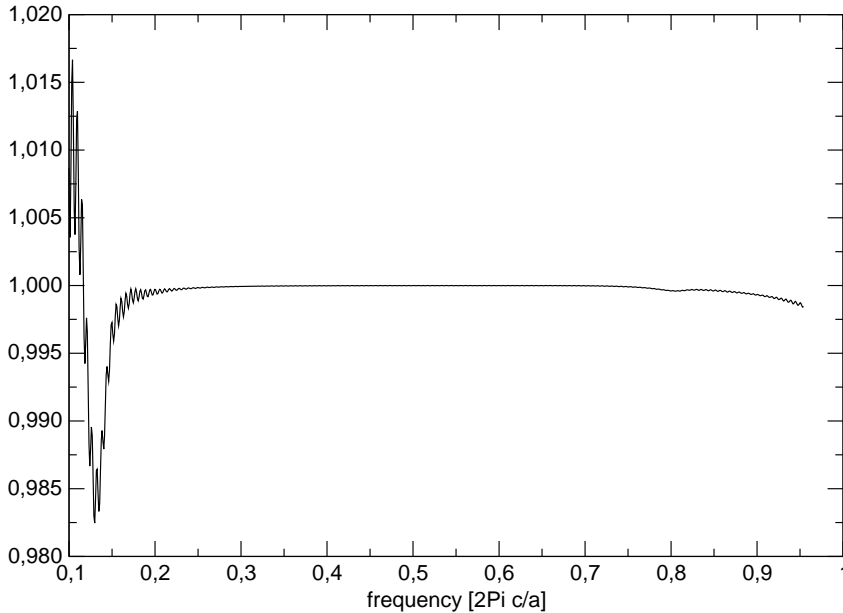


Figure 6.20: Ratio of the spectral waveguide transmission for two planes with distance $30a$.

channels that belong to the same waveguide mode but travel in different directions due to Bragg diffraction. However, it should be stressed that simplifications like these always require a good knowledge about the system under investigation because otherwise the interpretation of the results is misleading. A general problem in the comparison with experimental results is also that in experiments there are similar problems in providing controlled and well-defined conditions (e.g. single-mode excitation).

In this work (see e.g. chapter 4) we mainly used an in- and outcoupling with unpatterned dielectric waveguides because it is easier to produce well-defined conditions with localised guided modes than with extended plane waves. We inject a mode by first calculating its mode profile with standard solvers from planar optics [62] and then use the mode profile as an envelope function for a total-field/scattered-field approach. The argumentation so far relied more or less on a monochromatic excitation. However, to use the full potential of a time-domain method we should also apply pulsed sources. For a pulse we principally have to calculate the spatial profile for each frequency component and construct the TFSF-algorithm from this. This is very time consumptive in practice and therefore we use an approximation: We only calculate the profile for the center frequency of the pulse and inject a pulse with this spatial envelope into a unpatterned waveguide. The parts that do not exactly solve the eigenmode equation need some propagation length

to project to the right solutions while some parts radiate away. While this happens the pulse spreads in time due to the dispersion of different frequency components. Then, we record the pulse at a certain timestep at each space point that contains relevant parts and use this stored pulse as an initial field condition in transmission simulations. The error of this approximative method depends on the spectral pulse width, the dispersion of the waveguide and the spatial volume where it is recorded. Fig. 6.19 shows a typical excitation pulse. The error can be estimated by calculating the change in the spectral transmission of the pulse after some propagation length that ideally should be zero. Fig. 6.20 shows a small deviation in the range of 0.5% for a large frequency range. The deviation becomes larger for small frequencies (long wavelengths) which are not properly recorded by the finite cutout. For frequencies below 0.1 the results are not reliable.

6.4 Conclusion

In this chapter we have presented various aspects of the finite-difference time-domain (FDTD) method for solving the time dependant Maxwell-curl-equations. Besides the time integrating core-algorithm with field components localised on shifted subgrids within the Yee cell, the proper implementation of stability conditions, dielectric materials, boundary conditions and external sources has been discussed as well as various aspects of data extraction, that can be critical due to the nature of the Yee-cell or, as Fourier-transform related numbers, due to the time-domain character of the method. A solution for energy related numbers has been presented in form of a discrete version of Poynting's theorem. As the proper choice and adaptation of these building blocks of a FDTD-code is critical for accuracy, reliability, performance and stability of a simulation, we have given several concrete examples from photonic crystal analysis. Especially the proper choice of initial conditions or exciting pulse sources in bandstructure calculations for closed as well as for open systems has been discussed and substantiated by several investigations concerning pulse widths, localisation or symmetry considerations. Special interest has also been given to the calculation of losses in complex eigenvalue problems. Moreover, we carefully addressed transmission calculations of photonic crystal slabs and formulated a general guideline for obtaining reliable and unambiguous results.

7 Conclusions and Outlook

Based on FDTD-simulations, we have presented new unique results on the complex structure of electromagnetic fields in various classes of photonic crystals as well as discussed the computational method itself in the context of this application. Thereby, the main intention has been to achieve a realistic description of three dimensional systems with technological or fundamental relevance.

In chapter 3 we introduced the master equation that describes the eigenvalues and eigenmodes of an infinitely extended dielectric structure with discrete translational symmetry as a combination of Maxwell's equations and Bloch's theorem. Useful representations like Brillouin zone and bandstructure were also introduced and explained. By discussing spatial energy localisation in one- and two-dimensional structures we explained the existence of a bandgap, i.e. a frequency region where no eigenmodes exist, under appropriate conditions. The influence of the refractive indices and the geometry were discussed for several examples. Besides these physical principles that entirely characterise the ideal crystal, some auxiliary tools for an efficient and intuitive description like symmetry considerations or the supercell approach for defect structures were presented and supplemented with numerical examples. Our study of lower dimensional systems specifically is essential for the investigation of more complex systems discussed in the succeeding chapters because the superposition e.g. with finite size effects makes a proper identification of the mechanisms leading to a certain property difficult.

Chapter 4 addresses the interaction of a two-dimensional photonic crystal pattern with a vertical layer structure. This material system, that is often called photonic crystal slab, is the most prominent candidate for application in integrated optics, because of its relatively easy fabrication (compared to three dimensional crystals). It relies on total internal reflection for the confinement to the core layer and has regions in the bandstructure where the modes can be lossy due to the interaction with the environment mode bath. This interaction has been investigated in detail in this chapter for several configurations of the layer structure. We start with an air-bridge structure that only consists of a patterned high dielectric slab surrounded by air, then add semi-infinitely extended patterned low index cladding layers, cut these claddings to a finite thickness and finally mount this structure on a substrate. While the results for the air-bridge structure and the infinitely extended claddings closely resemble to standard predictions in literature, in the finite cladding case we have found an (up to now undescribed) new type of mode. These cladding-modes show significant intensity within the cladding layers and exist

for frequencies within the bandgap region of the core modes. Moreover, symmetry and field distribution allow a coupling to core modes leading to unexpected transmission for bandgap frequencies. As a consequence the bandgap is effectively destroyed. In the more realistic case on top of a substrate, the cladding modes are shown to be lossy. It will be a central aspect of future work to investigate the influence of cladding modes to defect structures like linedefect-waveguides.

We note that this part of our work directly touches one of the most important topics of today's photonic crystal research. Most of the interesting suggestions for optoelectronic applications rely on two-dimensional simulations and calculations. However, more and more, the vertical structure or, respectively, the in-plane waveguiding is realised to be the limiting factor. It has to be clarified in future if application proposals still hold after a full three-dimensional realistic analysis.

In chapter 5 we discuss the space-, polarisation- and frequency-dependance of the spontaneous emission rate in an inverted opal structure. In the limits of the weak coupling regime we demonstrate the equivalence of a classical approach to the full quantummechanical treatment, as has been shown in literature before. Then we adopt our FDTD-method to utilise this equivalence and analyse finite crystallites of an high index inverted opal with a complete photonic bandgap. The results show strong enhancement (up to a factor of ≈ 26) for emitter positions in dielectric regions and interfaces. The latter has also a strong polarisation dependance due to the continuity conditions of the electric eigenmodes. Moreover, we found that the photonic crystal effects can be obtained for relatively small finite crystallites and that the distance of the emitter to a surface is only relevant if it is less than 2 or 3 lattice constants. As inverted opals are very often used as a test system for luminescence and other light-matter-interaction experiments, these results are very important for the interpretation of these experiments. Normally, dye molecules are infiltrated into these opals and distribute inhomogenously. Very often an adsorbtion at dielectric interfaces takes place. Therefore, it is essential to take the spatial dependance of the spontaneous emission rate into account, because an estimation of an averaged emission modification based on the total density of states would yield inaccurate results.

In further studies it should be investigated if these effects can be used to tailor light emission in desired ways. However, it is not only the infiltration of active materials that gives reason for interesting applications. Also the inclusion of materials like liquid crystals that can be switched by external fields is an interesting perspective for future research. Moreover, new developments like direct laser writing give new motivation for the competition with slab structures in integrated optics, because they address the main disadvantage of three-dimensional structures in this respect, the difficulty of a controlled inclusion of defects.

All the results in this work have been obtained by FDTD-simulation. As FDTD is a very general method for analysing electrodynamic problems, several significant adaptations have to be done to achieve efficient, reliable and accurate results in photonic crystal analysis. The basics of the method itself as well as the proper detailed adjustments for different types of photonic crystal problems (e.g. bandstructure, transmission) have been discussed in chapter 6. Especially the appropriate excitation of guided and lossy modes in photonic crystal slabs has been studied and practical hints has been given.

However, although FDTD is now the standard tool for photonic crystal analysis (together with the plane-wave-expansion method) and the available computing power is fastly increasing, this method still suffers from its large demand of resources. Therefore, new developments in applied mathematics and numerics are strongly required, especially for optimisation of technologically relevant structures or intensive parameter scanning, that support FDTD analysis in future. Promising achievements in this field have been done with multigrid-methods or hybrid-basis-approximations. Moreover, new questions like fabrication tolerances make finite-element or finite-volume-approach reasonable, because they are better suited to resolve local deviations from the perfect structure. However, these new developments are only able to handle optically passive structures, while the general character of FDTD also allows in principle the inclusion of active materials. Efforts in this direction are highly active research topics. Therefore, in the analysis of new systems like photonic crystal lasers, fibre lasers or diodes that are based on photonic crystal structures, FDTD will play a leading role for technological applications, as well as in the theoretical investigation of the strong coupling regime of spontaneous emission.

Bibliography

- [1] E. Yablonovitch, "Inhibited spontaneous emission in solid-state physics and electronics", *Phys. Rev. Lett.* **58**, 2059 (1987).
- [2] S. John, "Strong localization of photons in certain disordered dielectric superlattices", *Phys. Rev. Lett.* **58**, 2486 (1987).
- [3] M. S. Thijssen, R. Sprik, J. E. G. J. Wijnhoven, M. Megens, T. Narayanan, A. Lagendijk, and W. L. Vos, "Inhibited light propagation and broad band reflection in photonic air-sphere crystals", *Phys. Rev. Lett.* **83**, 2730 (1999).
- [4] C. Hermann and O. Hess, "Modified spontaneous emission rate in an inverted opal structure with complete photonic band gap", *J. Opt. Soc. Am. B* **19**, 3013 (2002).
- [5] S. Y. Zhu, Y. Yang, H. Chen, H. Zheng, and M. S. Zubairy, "Spontaneous Radiation and Lamb Shift in Three-Dimensional Photonic Crystals", *Phys. Rev. Lett.* **84**, 2136 (2000).
- [6] S. John, T. Quang, "Spontaneous emission near the edge of a photonic band gap", *Phys. Rev. A* **50**, 1764 (1994).
- [7] O. Painter, J. Vuckovic, A. Scherer, "Defect modes of a two-dimensional photonic crystal in an optically thin dielectric slab", *J. Opt. Soc. Am. B* **16** (2), 275 (1999).
- [8] J. D. Joannopoulos, J. N. Winn, and R. D. Meade, "Photonic Crystals: Molding the Flow of Light", Princeton University Press (1995).
- [9] A. Mekis, J. C. Chen, I. Kurland, S. Fan, P. R. Villeneuve, and J. D. Joannopoulos, "High transmission through sharp bends in photonic crystal waveguides", *Phys. Rev. Lett.* **77**, 3787 (1996).
- [10] R. F. Cregan, B. J. Mangan, J. C. Knight, T. A. Birks, P. S. Russell, P. J. Roberts, and D. D. Allan, "Single-mode photonic band gap guidance of light in air", *SCIENCE* **285**:(5433) 1537 (1999).
- [11] D. Meissner, G. v. Freymann, private communications.

- [12] H. P. Schriemer, H. M. van Driel, A. F. Koenderink, and W. L. Vos, "Modified spontaneous emission spectra of laser dye in inverse opal photonic crystals", *Phys. Rev. A (Rapid Comm.)* **63**, 011801 (2001).
- [13] S. G. Johnson and J. D. Joannopoulos, "Block-iterative frequency-domain methods for Maxwell's equations in a planewave basis", *Optics Express* **8**, no. 3, 173 (2001).
- [14] S. Kittel, "Introduction to Solid State Physics", John Wiley and Sons (1995).
- [15] K. Busch, N. Vats, S. John, and B. C. Sanders, "Radiating dipoles in photonic crystals", *Phys. Rev. E* **62**, 4251 (2000).
- [16] M. M. Sigalas, R. Biswas, K.-M. Ho, and C. M. Soukoulis, "Theoretical investigation of off-plane propagation of electromagnetic waves in two-dimensional photonic crystals", *Phys. Rev. B* **58**, 6791 (1998).
- [17] T. D. Happ, A. Markard, M. Kamp, A. Forchel, and S. Anand, "Single-mode operation of coupled-cavity lasers based on two-dimensional photonic crystals", *Appl. Phys. Lett.*, **79**, 4091 (2001).
- [18] H. Kosaka, T. Kawashima, A. Tomita, M. Notomi, T. Tamamura, T. Sato, and S. Kawakami, "Self-collimating phenomena in photonic crystals", *Appl. Phys. Lett.*, **74**, 1212 (1999).
- [19] C. J. M. Smith, H. Benisty, D. Labilloy, U. Oesterle, R. Houdre, T. F. Krauss, R. M. de La Rue and C. Weisbuch, "Near-infrared microcavities confined by two-dimensional photonic bandgap crystals", *Electron. Lett.* **35** (3), 228 (1999).
- [20] C. Jamois, R. B. Wehrspohn, L. C. Andreani, C. Hermann, O. Hess, and U. Gösele, "Silicon-based two-dimensional photonic crystal waveguides", *Photonics and Nanostructures* **1**, 1 (2003).
- [21] S. G. Johnson, P. R. Villeneuve, S. Fan, and J. D. Joannopoulos, "Linear waveguides in photonic-crystal slabs", *Phys. Rev. B* **62**, 8212 (2000).
- [22] T. Baba, A. Motegi, T. Iwai, N. Fukaya, Y. Watanabe, and A. Sakai, "Light propagation characteristics of straight single-line-defect waveguides in photonic crystal slabs fabricated into a silicon-on-insulator substrate", *IEEE J. Quantum Electron.* **38**, 743 (2002).
- [23] M. Notomi, A. Shinya, K. Yamada, J.-I. Takahashi, C. Takahashi, and I. Yokohama, "Structural tuning of guided modes of line-defect waveguides of silicon-on-insulator photonic crystal slabs", *IEEE J. Quantum Electron.* **38**, 736 (2002).

- [24] T. F. Krauss, C. J. M. Smith, B. Vogele, S. K. Murad, C. D. W. Wilkinson, R. S. Grant, M. G. Burt, and R. M. De La Rue, "Two-dimensional waveguide based photonic microstructures in GaAs and InP", *Microelectron. Eng.* **35**, 29 (1997).
- [25] W. Bogaerts, P. Bienstman, and R. Baets, "Scattering at sidewall roughness in photonic crystal slabs", *Opt. Lett.* **28**, 689 (2003).
- [26] S. Fan, P. R. Villeneuve, and J. D. Joannopoulos, "Theoretical investigation of fabrication-related disorder on the properties of photonic crystals", *J. Appl. Phys.* **78**, 1415 (1995).
- [27] K. Sakoda, "Optical Properties of Photonic Crystals", Springer (2001).
- [28] S. G. Johnson, S. Fan, P. R. Villeneuve, J. D. Joannopoulos, and L. A. Kolodziejski, "Guided modes in photonic crystal slabs", *Phys. Rev. B* **60**, 5751 (1999).
- [29] Y. A. Vlasov, conference contribution, PECS V, Kyoto, 2004.
- [30] Y. Xu, R. K. Lee, A. Yariv, "Finite-difference time-domain analysis of spontaneous emission in a microdisk cavity", *Phys. Rev. A* **61**, 033808 (2000).
- [31] P. Meystre and M. Sargent III, "Elements of Quantum Optics", Springer (1990).
- [32] S. John, J. Wang, "Quantum Electrodynamics near a Photonic Band Gap: Photon Bound States and Dressed Atoms", *Phys. Rev. Lett.* **64**, 2418 (1990).
- [33] N. Vats, S. John, and K. Busch, "Theory of fluorescence in photonic crystals", *Phys. Rev. A* **65**, 043808 (2002).
- [34] R. Sprik, B. A. van Tiggelen, and A. Lagendijk, "Optical emission in periodic dielectrics", *Europhys. Lett.* **35**, 265 (1996).
- [35] G. Kweon and L. M. Lawandy, "Quantum Electrodynamics in Photonic Crystals", *Opt. Comm.* **118**, 388 (1995).
- [36] Z. Y. Li, L. L. Lin, and Z. Q. Zhang, "Spontaneous Emission from Photonic Crystals: Full Vectorial Calculations", *Phys. Rev. Lett.* **84**, 4341 (2000).
- [37] Z. Y. Li and Y. Xia, "Optical photonic band gaps and the Lamb shift", *Phys. Rev. B (Rapid Comm.)* **63**, 121305(R) (2001).
- [38] Z. Y. Li and Y. Xia, "Full vectorial model for quantum optics in three-dimensional photonic crystals", *Phys. Rev. A* **63**, 043817 (2001).
- [39] H. Chew, "Radiation and lifetimes of atoms inside dielectric particles", *Phys. Rev. A* **38**, 3410 (1988).

- [40] F. L. Kien, N. H. Quang, and K. Hakuta, "Spontaneous emission from an atom inside a dielectric sphere", *Opt. Commun.* **178**, 151 (2000).
- [41] R. K. Lee, Y. Xu, A. Yariv, "Modified spontaneous emission from a two-dimensional photonic bandgap crystal slab", *J. Opt. Soc. Am. B* **17**, 1438 (2000).
- [42] J. E. G. J. Wijnhoven and W.L. Vos, "Preparation of photonic crystals made of air spheres in titania", *Science* **281**, 802 (1998).
- [43] A. Blanco, E. Chomski, S. Grabtchak, M. Ibisate, S. John, S. W. Leonard, C. Lopez, F. Meseguer, H. Miguez, J. P. Mondia, G. A. Ozin, O. Toader, and H. M. van Driel, "Large-scale synthesis of a silicon photonic crystal with a three-dimensional bandgap near 1.5 micrometers", *Nature* **405**, 437 (2000).
- [44] H. Miguez, F. Meseguer, C. Lopez, M. Holgado, G. Andreasen, A. Mifsud, and V. Forn, "Germanium FCC Structure from a Colloidal Crystal Template", *Langmuir* **16**, 4405 (2000).
- [45] K. Busch, S. John, "Photonic band gap formation in certain self-organizing systems", *Phys. Rev. E* **58**, 3896 (1998).
- [46] J. Callaway, "Energy Band Theory," Academic Press (1964).
- [47] T. Suzuki and P. K. L. Yu, "Emission power of an electric dipole in the photonic band structure of the fcc lattice", *J. Opt. Soc. Am. B* **12**, 570 (1995).
- [48] K. S. Yee, "Numerical solution of initial boundary value problems involving Maxwell's equations in isotropic media", *IEEE Trans. Antennas Propagat.* **AP-14**, 302 (1966).
- [49] A. Taflove, "Advances in Computational Electrodynamics", Artech House (1998).
- [50] www.fdttd.org
- [51] Y. Dumeige, F. Raineri, and A. Levenson, "Second-harmonic generation in one-dimensional photonic edge waveguides", *Phys. Rev. E* **68**, 066617 (2003).
- [52] J. Y. Wang, Y. W. Kiang, and C. C. Yang, "Band structure calculations of photonic crystals with dispersive materials", *Proceedings of SPIE*, **4905**, 62 (2002).
- [53] M. Qiu and S. He, "Numerical method for computing defect modes in two-dimensional photonic crystals with dielectric or metallic inclusions", *Phys. Rev. B* **61**, 12871 (2000).
- [54] G. Mur, "Absorbing boundary conditions for the finite-difference approximation of the time-domain electromagnetics field equations", *IEEE trans. antennas propagat.* **EMC-23**, 377 (1981).

- [55] J. P. Berenger, "A perfectly matched layer for the absorption of electromagnetic waves", *J. Computational Physics* **114**, 185 (1994).
- [56] W. Nolting, "Grundkurs: Theoretische Physik 3 Elektrodynamik", Zimmermann-Neufang (1990).
- [57] J. de Moerloose and D. de Zutter, "Poynting's theorem for the finite-difference-time-domain method", *Microw. and Opt. Technology Lett.* **8**, 257 (1995).
- [58] J. G. Proakis and D. G. Manolakis, "Digital Signal Processing: Principles, Algorithms and Applications", Prentice Hall (1996).
- [59] S. G. Johnson, MIT Photonic-Bands. Available: <http://ab-initio.mit.edu/mpb>.
- [60] L. C. Andreani and M. Agio, "Photonic bands and gap maps in a photonic crystal slab", *IEEE J. Quantum Electron.* **38**, 891 (2002).
- [61] C. T. Chan, Q. L. Yu, K. M. Ho, "Order-N spectral method for electromagnetic waves", *Phys. Rev. B* **51**, 16635 (1995).
- [62] K. J. Ebeling, "Integrierte Optoelektronik", Springer (1989).